ASSESSING THE ACCURACY OF USING BIPLANAR RADIOGRAPHY COMBINED WITH COMPUTED TOMOGRAPHY TO ESTIMATE CARTILAGE DEFORMATION IN THE HIP

by

Katharine Joan Wilson

B.A.Sc., Queen's University, 2008

A THESIS SUBMITTED IN PARTIAL FULFILLMENT OF
THE REQUIREMENTS FOR THE DEGREE OF

MASTER OF APPLIED SCIENCE

in

THE FACULTY OF GRADUATE STUDIES

(Mechanical Engineering)

THE UNIVERSITY OF BRITISH COLUMBIA

(Vancouver)

September 2011

Abstract

Excessive or abnormal joint loading that leads to cartilage degeneration has been associated with hip osteoarthritis (OA). Before preventative measures for OA can be designed, such as physiotherapy techniques, braces, or surgical interventions, the connection between load-bearing and cartilage degeneration needs to be validated experimentally. As a first step towards such a validation, a method of measuring the load distribution across the hip joint is needed; ideally that can be used *in vivo* and can detect changes in the load distribution during an applied load. The objective of this study was to assess the accuracy of using biplanar radiography combined with CT imaging to estimate hip cartilage strain across the joint as an indication of the load distribution.

Estimating cartilage strain using biplanar radiography and CT imaging is a multi-device multi-step measurement protocol that has error associated with each step. While biplanar radiography systems are commonly assessed on their ability to measure radio-opaque bead locations, to the author's knowledge no studies have quantified errors in the additional steps of estimating cartilage strain. The present study used a phantom hip joint to quantify the errors in measuring bone displacement with biplanar radiography, segmenting 3D joint surfaces from a CT image, and measuring the relative proximity of joint surfaces in the biplanar radiography coordinate frame. The quantified errors were much lower than *ex vivo* hip cartilage deformation results in the literature, which demonstrated the potential for using this technique to estimate cartilage strain in the hip.

As a proof of concept, cartilage strain was estimated in the *ex vivo* hip joint during a compressive load. Two hemi-pelvis/proximal femur specimens, with radio-opaque beads inserted in each bone, were loaded in compression in a materials testing machine, with biplanar radiographs acquired throughout. A small amount of cartilage deformation (0.1mm) was detected across the hip joint; however, due to the low load applied the deformation results were not comparable to the literature. The largest cartilage strains were identified in the anterior and superior regions, which was consistent with the literature. Future studies using higher loads are needed to further assess the capabilities of our system.

Preface

Colin Russell is a M.A.Sc. candidate with the Orthopaedic Injury Biomechanics Group (OIBG) at UBC and wrote the de-noising algorithm used for the biplanar radiographic images (as described in Chapter 2).

This work was approved by the UBC Clinical Research Ethics Board (number H08-01931).

Table of Contents

List of Tables

List of Figures

List of Abbreviations

2D – Two dimensional

3D – Three dimensional

ASIS – Anterior superior iliac spine

CT – Computed tomography

FAI – Femoroacetabular impingement

FEM – Finite element modeling

MR – Magnetic resonance

MRI – Magnetic resonance imaging

OA – Osteoarthritis

PSIS – Posterior superior iliac spine

qMRI – Quantatative magnetic resonance imaging

Acknowledgments

I would like to acknowledge my supervisor, Dr. David Wilson, for his guidance and expertise throughout this thesis. I would also like to thank my committee members, Dr. Peter Cripton and Dr. Michael Gilbart, for their insight and feedback.

I am grateful to Angela Kedgley for her mentorship, encouragement, and endless optimism. She inspired and challenged me to be a better researcher, and I am so thankful for all her time and effort. The many late night/early morning phone calls to the UK were beyond appreciated.

This thesis benefited from the mechanical insight and creative solutions of Dr. Robin Coope of the BCCA Machine Shop, and from the CT expertise of Dean Malpas at the Canada Diagnostics Centre.

I would like to thank all of the students and staff in our lab for their help and suggestions. In particular I would like to thank Emily McWalter, Agnes d'Entremont, Shahram Amiri, Laura Given, Erin Lucas, Colin Russell, Jason Chak, Heather Murray, Maryam Shahrokni, Seth Gilchrist, Robyn Newell, Carolyn Van Toen, and Hannah Gustafson.

I am grateful to my friends and family for their never-ending support and encouragement. Thanks to Heather Murray, Erin Lucas and Paul Carter for their energy and fun-loving attitudes. To Sarah, for being a great listener and my role model through all aspects of life. And to my parents, for their unconditional love, support and a world of patience.

I would like to thank my funding support including Centre for Hip Health and Mobility, ICORD, the National Sciences and Engineering Research Council of Canada, the Canadian Arthritis Network and the University of British Columbia.

To my family for their endless support, guidance and love.

Chapter 1. Introduction and Literature Review

1.1 Introduction

Hip osteoarthritis (OA) is a painful and progressive disease that begins primarily as inflammation and pain around the hip, but progresses to mechanical damage in the joint characterized by cartilage fibrillation, sclerosis of the subchondral bone, osteophytes, and subchondral cysts [1-3]. The reasons behind the initiation and progression of hip OA are unclear, but the most widely accepted theory is that excessive or abnormal joint loading increases stress concentrations in the cartilage, leading to cartilage wear and degeneration [4-6]. The connection between load-bearing and cartilage degeneration needs to be validated experimentally before preventative measures for OA can be designed. As a first step towards such a validation, a method of measuring the load distribution across the hip joint is needed; ideally using a method that can be extended to *in vivo* studies and can detect changes in the load distribution during a physiological activity. The objective of this study was to assess the use of biplanar radiography combined with CT imaging to estimate hip cartilage deformation as an indication of the load distribution.

1.2 The hip joint

1.2.1 Articular surfaces

The hip joint is a synovial articulation between the acetabulum and the femoral head (Figure 1a) [7]. The femoral head is contained within the cup-like acetabulum to create a ball-and-socket joint. The articular surface of the acetabulum is a horseshoe-shaped strip of articular hyaline cartilage (the lunate surface) that lines the surface of the acetabulum. The central and inferior regions of the acetabulum, in which the acetabular fossa and acetabular notch are found, respectively, are not covered by cartilage. The rim of the acetabulum is enlarged by a fibrocartilaginous structure called the labrum (Figure 1b), which is continuous with the articular hyaline cartilage in the acetabulum. In the inferior portion of the acetabulum the labrum bridges the acetabular notch as the transverse acetabular ligament. The articular surface of the proximal femur is the femoral head, which is connected to the femoral shaft by the femoral neck. The femoral head is covered by articular hyaline cartilage excluding a small region, the fovea, which is not covered by cartilage to allow insertion of the ligamentum teres femoris, a ligament which connects directly from the femoral head to the acetabular notch.

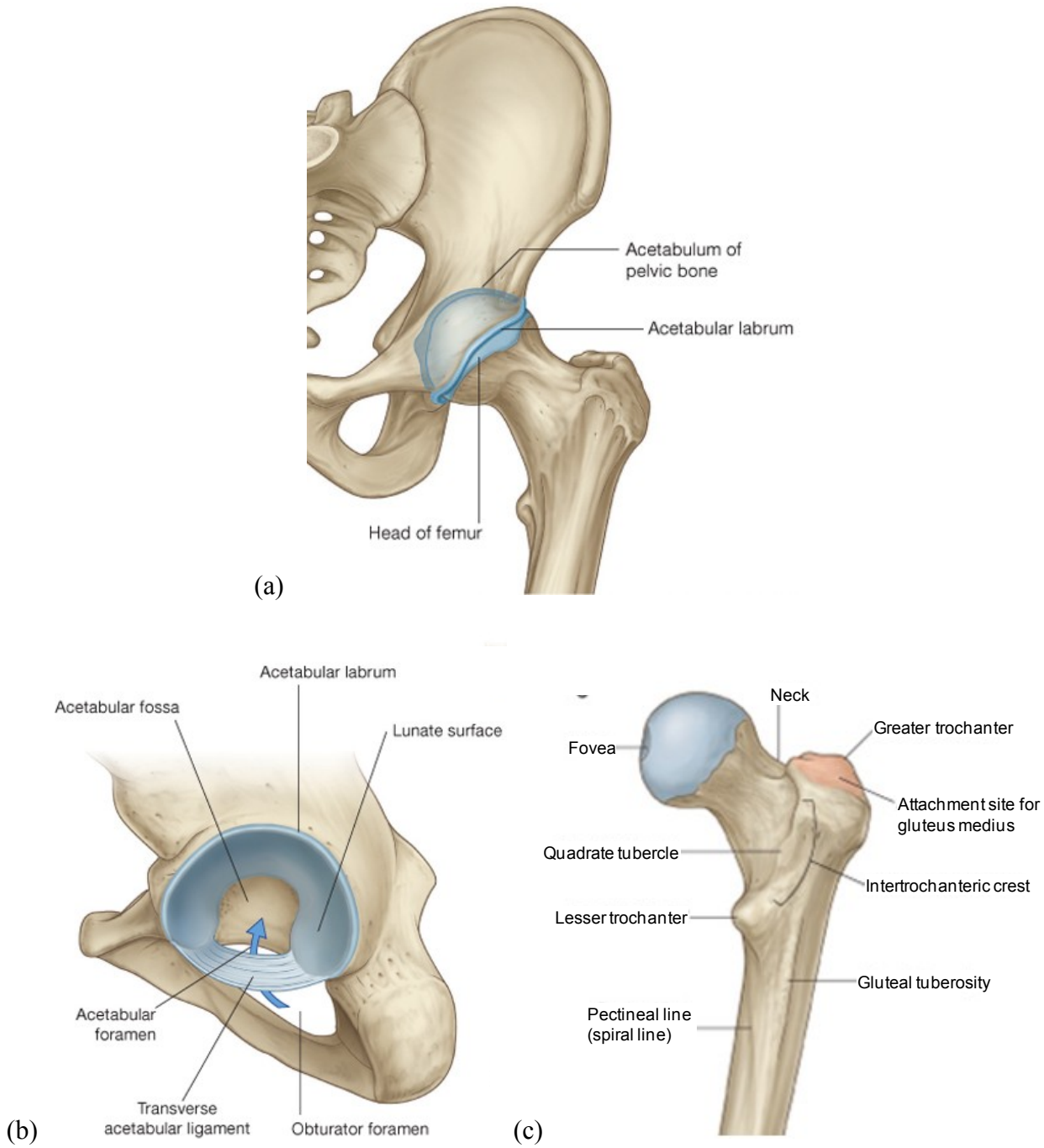

Figure 1. Hip joint anatomy, showing (a) the articular surfaces of the acetabulum and femoral head, and the main anatomical features of the (b) acetabulum and (c) proximal femur. [Reprinted from Gray's Anatomy for Students 2nd edition, Drake et al., 2009, with permission from Elsevier]

1.2.2 **Joint capsule**

The hip joint is enclosed by a synovial membrane and a thick fibrous membrane, referred to as the joint capsule (Figure 2a), which extends from the femoral neck to above the acetabular rim. Three ligaments are present to reinforce the joint capsule, as well as stabilize the joint overall: iliofemoral, pubofemoral, and ischiofemoral ligaments (Figure 2b).

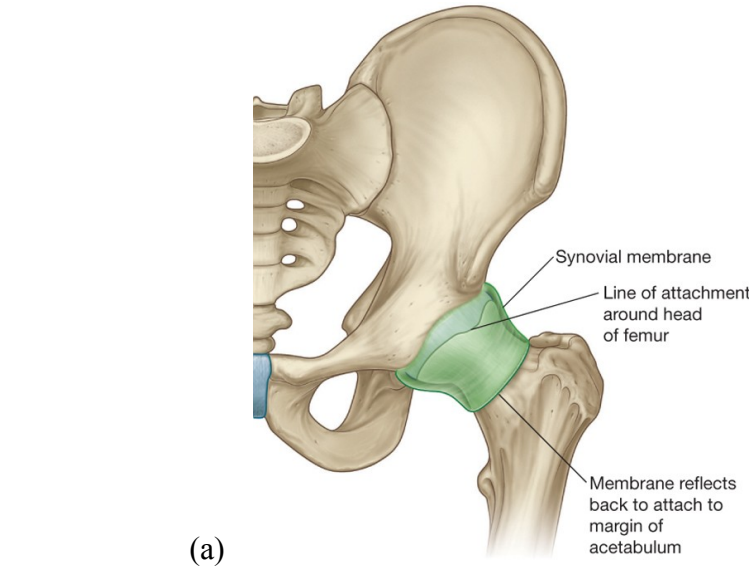

(a)

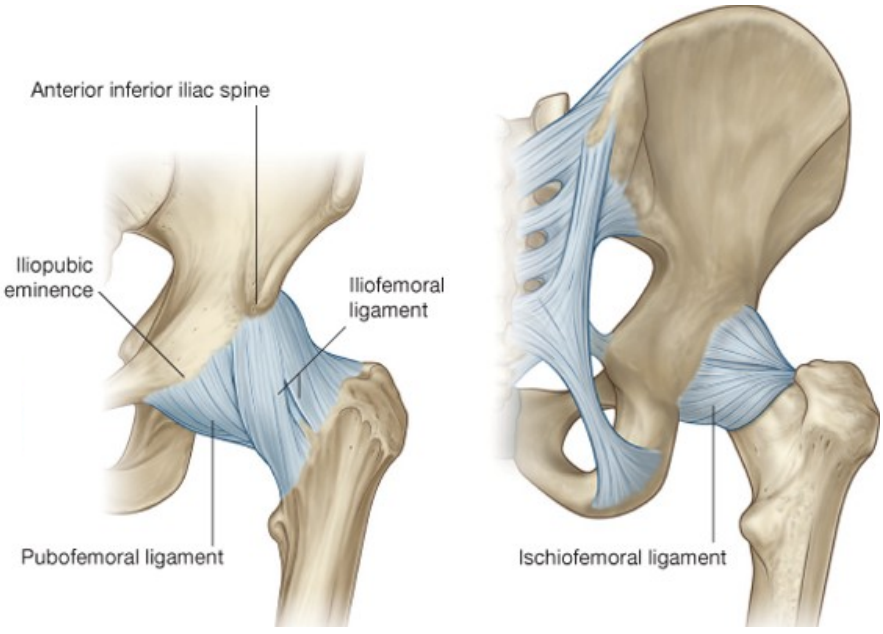

(b)

Figure 2. The joint capsule encloses the hip joint (a), and is reinforced by the iliofemoral, pubofemoral, and ischiofemoral ligaments (b). [Reprinted from Gray's Anatomy for Students 2nd edition, Drake et al., 2009, with permission from Elsevier]

1.2.3 **Hip cartilage and behavior under load**

Articular cartilage covers the load-bearing surfaces of the hip joint and allows the joint surfaces to glide with low friction during movement. The total cartilage thickness in the hip typically ranges from 1.0-3.0mm [8-10]. Femoral head cartilage is slightly thicker than acetabular cartilage, with one study reporting a mean thickness of 1.43±0.16mm (mean±standard deviation) for the femoral cartilage and 1.33±0.22mm for the acetabular cartilage, which were found using an ultrasound measurement technique [8]. The maximum cartilage thickness is found anterior and superior to the fovea on the femoral head, and in the anterosuperior region of the acetabulum [8, 9].

Articular cartilage is composed of 68-85% water by weight, and during loading it deforms predominantly through changes in tissue volume by fluid expression [11]. Little is known about the amount of cartilage deformation in the hip. One study loaded six *ex vivo* hip joints statically to simulate single-legged stance (230% bodyweight), and found a mean cartilage deformation of 0.960 mm relative to an unloaded position over a 225 minute loading period [12]. Another study used single-plane radiography to measure cartilage deformation in twenty-eight *ex vivo* hip joints during simulated walking (500% bodyweight) and found cartilage deformation up to 14% of the unloaded cartilage thickness [13]. While there is variance in the hip cartilage deformation results reported in the literature, it has been concluded that the load distribution is not uniform across the joint surface. This was found using mechanical and imaging techniques (pressure sensitive film, miniature pressure transducers, instrumented prostheses), which identified the anterosuperior region of the joint as the most heavily loaded [10, 12, 14].

During loading, the presence of pressurized fluid between the acetabular and femoral cartilage layers is thought to help maintain cartilage health by supporting loads transmitted through the hip. The presence of pressurized fluid between the acetabular and femoral cartilage layers has been identified by observing the natural topography of cartilage using ultrasound techniques. When the hip joint is loaded, the opposing cartilage surfaces naturally maintain surface undulations (approximately 0.075mm in depth), which are thought to create a high-resistance pathway of fluid that spares the cartilage matrix from excessive loads [15]. In another study fourteen samples of bovine cartilage were tested under static compression while measuring the

interstitial fluid pressure, and it was found that the pressurized fluid supported up to 90% of the load [16].

It is believed that the labrum plays a fundamental role in maintaining cartilage health during loading by maintaining the fluid pressure within the joint and increasing the articular surface area. It has been suggested that the labrum acts as a seal to maintain the pressure in the hip joint, allowing the pressurized interstitial fluid to support loads transmitted through the joint [17]. The labrum also provides an additional 8 cm^2 to the articulating surface area of the acetabulum, allowing the hip loads to be distributed further across the joint surface [18].

1.2.4 **Hip osteoarthritis**

Hip osteoarthritis (OA) is painful and progressive disease that has been diagnosed in 5% of the population aged 65 or older, with 20% of those patients suffering from bilateral hip OA [19]. The disease is characterized by sharp joint pain during activity, particularly during internal and external rotation of the hip. While the disease begins primarily as inflammation and pain around the hip, it progresses to mechanical damage in the joint characterized by cartilage fibrillation, sclerosis of the subchondral bone, osteophytes, and subchondral cysts [1-3]. The reasons behind the initiation and progression of the disease are unclear, but joint mechanics are believed to play a central role. The most widely accepted theory of hip OA is that excessive or abnormal joint loading increases stress concentrations in the cartilage, leading to cartilage wear and degeneration [4-6]. While this statement has not been validated experimentally, the anterosuperior region of the hip joint has been identified using imaging and mechanical methods as a higher load-bearing region [10, 14, 20-22], as well as a more commonly degenerated area of the cartilage during OA [23]. The connection between load-bearing and cartilage degeneration needs to be further understood before preventative measures for OA can be designed. By understanding the load distribution in the healthy hip joint, preventative measures, such as physiotherapy, orthotics, braces, or surgical techniques, could be used to correct abnormal joint biomechanics and prevent the progression of OA. To experimentally validate the connection between load-bearing and cartilage degeneration, the load distribution and regional cartilage degeneration need to be measured in normal and osteoarthritic hip joints for comparison. As a first step towards such a validation, a method of measuring the load distribution across the hip joint is needed. Ideally load distribution would be measured non-invasively, allowing *in vivo*

studies to be completed with physiological loading conditions and muscle activations, as well as measured continuously throughout an applied load, allowing changes in the load distribution to be detected during a physiological activity.

1.3 Intra-articular hip loading

1.3.1 Contemporary methods to quantify hip loads

Currently the methods of measuring load distribution in the hip joint are generally invasive and cannot be extended to *in vivo* research studies, or rely on static imaging techniques, which cannot provide information throughout a physiological activity. The following section outlines the contemporary methods of quantifying hip loading, and their associated limitations.

1.3.1.1 Pressure sensitive film

The most commonly used method of quantifying hip loads *ex vivo* is with pressure sensitive film, which has been used to measure the load distribution across the joint surface during simulated activities such as walking [14, 24] and one-legged stance [25, 26]. However, only the maximum load experienced at each point on the film can be quantified, and therefore this method is only useful to study the peak load distribution and cannot provide information throughout a physiological loading activity.

A major drawback of using pressure sensitive film is the invasive procedure of disarticulating the hip joint to wrap the film around the femoral head, and re-articulating the joint for subsequent loading. This process disrupts the joint capsule and can drastically change the loading environment in the joint.

Another limitation to this method is the effect of adding a relatively thick and stiff film into the joint on the contact mechanics and load values recorded. The thinnest film available is 0.2mm thick [14], which is relatively large compared to the cartilage thickness in the hip (typically ranging from 1.0-3.0mm) [9]. Pressure sensitive film also has an average elastic modulus of approximately 100MPa in compression [27], which is larger by a factor of 100-300 compared to the elastic modulus of normal articular cartilage [28]. Finally, it is difficult to wrap a flat film around a spherical joint, such as the hip, without creating wrinkles in the film, which can create error in the film's measurements [27]. Using finite element modeling it has been predicted that with the combination of the film's thickness, stiffness, and measurement error due to wrinkling,

the addition of pressure sensitive film can change the maximum load recorded in the hip by up to 28% [29].

1.3.1.2 Pressure transducers

As a dynamic measure of load distribution, miniature pressure transducers have been inserted in the superficial layer of either the femoral or acetabular cartilage in the hip *ex vivo* [30]. While this method allows a direct and time-variant measure of the load distribution, it requires a heavily invasive procedure including the destruction of the joint capsule, creation of cylindrical wells in the cartilage for transducer placement, and application of dental cement in each well to secure the transducer in place. The development of pressure sensitive film facilitated this process of directly measure load distribution because it had higher resolution and avoided altering the cartilage with cylindrical wells.

1.3.1.3 Instrumented prostheses

In an effort to study the hip in a physiological loading environment, instrumented prostheses have been inserted *in vivo* to directly measure the load distribution. A considerable advantage of this *in vivo* method is that a variety of loading environments and activities can be studied while physiological muscle forces are acting on the joint. One study looked at the average peak hip loads in four patients with instrumented prostheses during nine different activities, including different speeds of walking on level ground, walking up and down stairs, standing up, sitting down, standing on one leg, and knee bending. The measurements were normalized for the subject's bodyweight and the average peak hip contact forces across the four subjects are shown in Table 1.

Table 1. Average peak hip loads across four patients during daily living activities, measured with an instrumented prosthesis and normalized for the subject's bodyweight [21].

Activity	Average peak hip load (% BW)
Slow walking (3.5 km/h)	242
Normal walking (3.9 km/h)	238
Fast walking (5.3 km/h)	250
Up stairs	251
Down stairs	260
Standing up	190
Sitting down	156
Standing on 2-1-2 legs	231
Knee bend	143

The use of instrumented prostheses is limited due to the low number of patients that have such devices implanted, the patients that have the devices implanted also all necessarily have hip disease, the prosthetic components do not represent the natural incongruity of the femoral head and acetabular surfaces, and the cartilage-cartilage interface in the hip is replaced by a plastic-metal interface.

1.3.1.4 qMRI

More recently, quantitative magnetic resonance imaging (qMRI) has been used to non-invasively measure three-dimensional cartilage strain in the hip in response to loading, and has potential for *in vivo* studies. This method uses ultra high-resolution MRI images acquired of the cartilage before, during and after static joint loading. The cartilage is identified relative to the subchondral bone, cartilage thickness is measured across the whole surface, and cartilage strain is mapped over the femoral head surface at each stage of the loading application. One study used qMRI to measure hip cartilage deformation in six volunteers after periods of standing, walking or lying supine [10]. While the greatest change in cartilage thickness between unloaded and loaded cartilage was found in the anterosuperior region, as expected for this higher load-bearing region, the authors suggested that the 1.5T MRI scanner used did not have sufficient imaging resolution to accurately measure cartilage deformation. Another study used qMRI to determine the effect of a torn, repaired and resected labrum on cartilage strain in seven *ex vivo* hips during simulated loading for single-legged stance [12]. It was found that resection of the labrum caused a significant increase in cartilage strain during load, but a torn or repaired labrum did not.

While qMRI allows three-dimensional cartilage strain to be mapped in the hip as an indication of the load distribution, it is limited by the imaging resolution of the MR scanner. High imaging resolution is essential for avoiding a partial volume effect, in which a voxel lies over cartilage and bone or joint fluid simultaneously and has a lower intensity than if it lies entirely over cartilage. A tradeoff of acquiring higher imaging resolution is longer image acquisition times. To avoid motion artifacts during the longer acquisition times, cartilage must be loaded statically, which involves waiting for the cartilage to reach a steady-state thickness under load. Due to these limitations, qMRI is restricted to a static analysis of hip loading and cannot provide information throughout a dynamically applied load.

1.3.1.5 Finite element modeling

The load distribution in the hip has been analyzed using finite element models (FEM) to quantify the effects of changing different parameters such as bone geometry, bone deformation, and cartilage stiffness; however, the load distribution predicted by the models varied greatly depending on the parameters used [31, 32]. One study analyzed the effect of using different test parameters in computational models of the loaded hip joint; including geometry of the bone-cartilage interface (subject-specific, spherical or a conchoidal), and cartilage thickness (constant or irregular). It was found that the peak loads and contact areas in the models varied dramatically depending on the test parameters, and created doubt in the reliability of the current finite element models of the hip [31]. Further, validation of these models in the laboratory has been limited, and has relied on comparison with *ex vivo* methods, which have their own inherent limitations as described above.

1.3.2 **Using biplanar radiography and CT to quantify hip loads**

There is no known method of non-invasively and dynamically quantifying the three-dimensional load distribution in the hip joint. However, cartilage strain can be measured in response to an applied load, and the loading distribution across the joint can be inferred from strain. Biplanar radiography combined with computed tomography (CT) imaging has recently been used to quantify changes in cartilage thickness during loading [33, 34], and has the potential to estimate cartilage strain in the *ex vivo* and *in vivo* hip joint. This section outlines the methodology used to estimate hip cartilage strain with biplanar radiography and CT imaging, and sources of error in the associated steps.

Biplanar radiography has been used extensively to track *in vivo* and *ex vivo* bone displacement during joint loading by measuring the locations of radio-opaque beads rigidly inserted in the bones [34-41]. Contemporary biplanar radiography systems use two continuous x-ray sources and high-speed video cameras to dynamically acquire radiographic images of the joint while a load is applied. The system is calibrated in three-dimensions to define the position and orientation of the x-ray sources around the joint, which allows the three-dimensional coordinates of the beads to be measured. Since each bone and its respective beads act as a rigid body, the measured bead displacements can be used to describe the location of each bone during the applied load. CT imaging is used to create high-resolution 3D surface models of the bones and

register them to the measured bone locations in the biplanar radiography coordinate system, allowing the relative location of the joint surfaces to be determined throughout the applied load [33, 42, 43]. More recently this technique has been used to estimate cartilage thickness during loading by measuring the minimum distances between the bone surface models [33, 34].

To date, only one study has used biplanar radiography and CT imaging to measure cartilage thickness in the hip joint. Two *ex vivo* hip specimens were flexed and extended passively for 1.0s durations to simulate level walking and a chair ascent, and the location of minimum cartilage thickness in the anterosuperior region of the acetabulum was measured throughout the motion [22]. One limitation of the study was that 36.7% of the biplanar radiographs collected were excluded from the analysis, either due to difficulty in identifying the beads in the radiographs because of poor image contrast or migration of the beads was found within the bone. Studies of the hip joint have been limited partially due to the poor image contrast in the acquired radiographs, which is a result of the greater amount of soft tissue surrounding the hip relative to other articular joints. This method has been used more commonly to measure joint surface articulations in the knee [33-35, 42, 44-49], ankle [50, 51] and shoulder [52], demonstrating the considerable potential for similar measurements in the hip. For example, one study measured the minimum distances between the tibiofemoral surfaces during one-legged hopping, as an estimate of the cartilage thickness, and found a higher deformation of the cartilage in the medial compartment than the lateral compartment (Figure 3) [42].

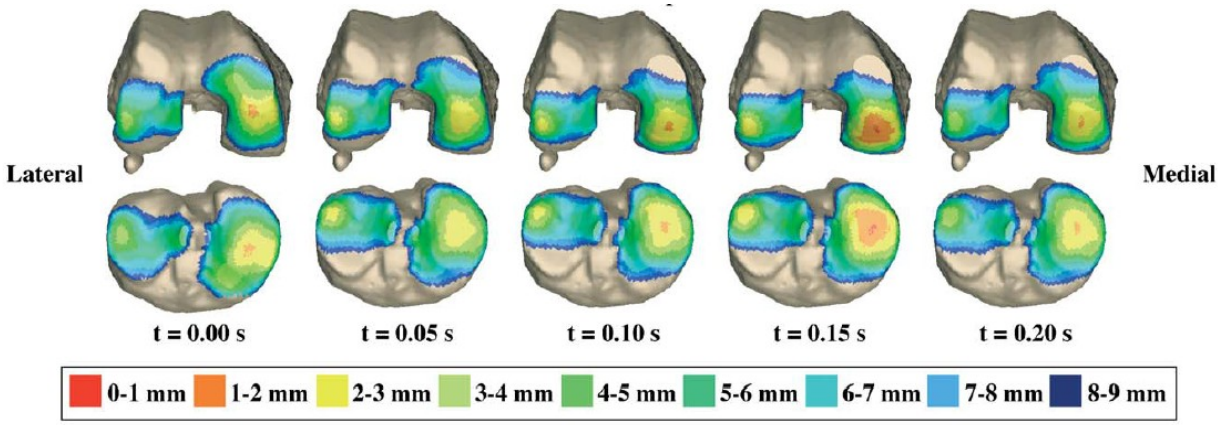

Figure 3. Color-coded distance map sequence showing the minimum distances between the femur and tibia surfaces after a one-legged hop landing. Time is time post-foot touchdown. [Reprinted from Journal of Biomechanics, Vol 36, Anderst W. et al., A method to estimate in vivo dynamic articular surface interaction, p.1296, 2003, with permission from Elsevier].

A limitation of this method is that the insertion of radio-opaque markers in the bone is an invasive technique; however, *in vivo* studies have found that the subjects heal entirely and the markers remain secure within the bone [33, 34, 46, 47, 50]. Marker-less systems are also currently being explored. These systems use CT surface models of the joint to create digitally reconstructed radiographs of the joint at each frame. The position and orientation of the surface models are adjusted until the digitally reconstructed radiographs match the original biplanar radiographs, and then the cartilage thickness measurements are completed as previously described. This marker-less technique has shown potential for non-invasive *in vivo* studies, but has the inherent tradeoff of relying heavily on complex image registration algorithms. The accuracy of marker-less systems is still being validated in the literature [22, 36, 45].

A limitation that is often reported regarding biplanar radiography studies is the exposure of subjects to radiation during testing; however, radiation levels reported in all studies in the literature were below the recommended dose limits for patients and workers stated by Health Canada [53].

Advantages of the biplanar radiography and CT imaging technique for analyzing the load distribution in the hip are that cartilage strain can be measured in response to a dynamically applied load, the joint capsule remains intact, and there is potential for *ex vivo* and *in vivo* studies. The 3D measurement of cartilage thickness also has a considerable advantage over 2D imaging techniques (planar radiography, 2D MR imaging), which rely on an accurate selection of the image slice orientation for cartilage thickness measurements and do not describe cartilage deformation regionally.

1.3.2.1 Sources of error using biplanar radiography

Although biplanar radiography has several advantages over other techniques of measuring cartilage strain, particularly the dynamic image capture and potential for *ex vivo* and *in vivo* measurements, there are sources of error that must be taken into account to accurately measure the location of the bones during loading. The biplanar radiography system needs to be calibrated in three dimensions. To ensure that the locations of the beads in the radiographs can be accurately measured in the laboratory coordinate system, this involves determining the position and orientation of the x-ray sources around the joint. Identifying the bead centroids in the radiographs is also a source of error, in that each bead is represented by a projected image on the

radiograph, which is subject to poor image contrast and image noise. Both the calibration of the system and its ability to track bead centroids need to be assessed for accuracy before *ex vivo* and *in vivo* experiments can be completed. While calibration errors are not often reported, the ability to measure bead locations is commonly assessed using a phantom study, with bead tracking errors reported in the literature in the range of 0.018-0.075mm [54-57]. As our biplanar radiography system is new to the laboratory and is a custom assembly of equipment, an accuracy assessment of its ability to measure the locations of radio-opaque beads needed to be completed.

1.3.2.2 Sources of error using CT imaging

The process of using CT imaging to segment the bead locations and joint surfaces is subject to error due to image resolution and metal artifacts from the beads. Error in segmenting the surfaces can create 3D surface models that do not reflect the true shape of the joint surfaces and subsequently cause incorrect estimates of the cartilage thickness. To minimize this error, high image resolution is essential for correctly identifying the boundaries of each bone surface. Accurately measuring the centroids of the beads in the CT image is also important since they are used to align the CT and biplanar radiography coordinate frames. Metal artifacts due to the beads in the CT image can create error in identifying the bead centroids, which subsequently influences the alignment of the CT and biplanar radiography coordinate frames. High image resolution also helps to minimize the error due to metal artifacts. To the author's knowledge, the errors in segmenting joint surfaces and using bead centroids to align the CT and biplanar radiography coordinate frames have not been reported.

1.4 Summary and direction

Excessive or abnormal joint loading leading to cartilage degeneration has been associated with hip osteoarthritis (OA). The connection between load-bearing and cartilage degeneration needs to be validated experimentally before preventative measures for OA can be designed. As a first step towards such a validation, a method of measuring the load distribution across the hip joint is needed; ideally using a method that can detect changes in the load distribution throughout a physiological activity and that can be extended to *in vivo* studies.

There is currently no method of measuring the load distribution in the hip non-invasively and with a continuous measure throughout the applied load. Pressure sensitive film and miniature

pressure transducers have been used to measure load distribution *ex vivo* [14, 21, 24-26, 30], but both methods involve destruction of the joint capsule, and the film only provides a static assessment of the peak load distribution. Instrumented prostheses can measure the load transmitted through the hip *in vivo* [21], but are not representative of physiological hip joint surfaces and are necessarily inserted in patients with diseased joints. qMRI has been used to measure cartilage strain in the hip as an indication of the loading distribution, and has potential for *ex vivo* and *in vivo* applications [10, 12]; however, this method uses static image acquisition and does not provide information on the changes in the load distribution throughout an applied load.

Biplanar radiography combined with CT imaging is the only known method that can estimate hip cartilage deformation continuously throughout an applied load[33, 34], and has potential for *ex vivo* and *in vivo* applications. This method can provide information on the distribution of strain across the joint, from which the load distribution can be inferred. Estimating cartilage deformation using biplanar radiography and CT imaging is a multi-device multi-step measurement protocol that has error associated with each step. To the author's knowledge no studies have quantified the errors that accumulate in the steps involved for estimating cartilage thickness.

The objective of this study was to assess the accuracy of using biplanar radiography combined with CT imaging to estimate hip cartilage deformation as an indication of the load distribution.

The objectives of the present study are as follows:

1. Assess the accuracy of using biplanar radiography and CT imaging for measuring the relative locations of joint surfaces. Specific errors to be assessed include that in measuring bone displacement using inserted radio-opaque beads, segmenting 3D joint surfaces from a CT image, and measuring the proximity of the joint surfaces in the biplanar radiography coordinate frame.
2. Estimate 3D cartilage thickness and deformation in response to a compressive load in the *ex vivo* hip joint using biplanar radiography and CT imaging.

Chapter 2. Biplanar Radiography Imaging System

2.1 Introduction

Biplanar radiography was developed for tracking three-dimensional (3D) motion of the skeletal system by *Selvik* in 1974 [40]. The method uses two x-ray sources to collect radiographs of a testing object during motion, and uses the location of the sources to determine the coordinates of the object in 3D. Advantages of this method for studying joint surface proximity include that it highly accurate and capable of acquiring images throughout a dynamically applied load.

Biplanar radiography systems vary between laboratories, as the equipment can be acquired as a fully-equipped commercial system, or as individual components that are combined to create a custom system. The advantage of a custom system is the equipment can be selected to attain certain testing requirements, such as high-speed image collection or low image noise. It should be noted that there are both static and dynamic biplanar radiography systems described in the literature, each with their own advantages. The static systems can collect one pair of biplanar radiographs during a testing session, and have shown high image quality and image contrast for viewing bone surfaces. The present study uses a system with dynamic capabilities, so that it is capable of collecting a high number of biplanar radiographs per second, but with the trade-off of less image contrast. For this reason radio-opaque beads are often attached to the objects of interest so that their motion can be tracked more accurately in the radiographs. The biplanar radiography system in our laboratory was acquired prior to the development of this project, and therefore my role included setting up the equipment and completing an accuracy assessment of its capabilities. This chapter outlines the biplanar radiography equipment and the imaging procedure used during the subsequent chapters of this study. For clarity, the steps involved in using our biplanar radiography system to track an object of interest are laid out in a flow chart below (Figure 4). By calibrating the biplanar radiography system in three dimensions (left pathway), and acquiring biplanar radiographs of a beaded object during motion (right pathway), the beads attached to the object can be accurately tracked in space. Finally to ensure the beads are rigidly attached to the object of interest during testing, a rigid body motion error can be calculated.

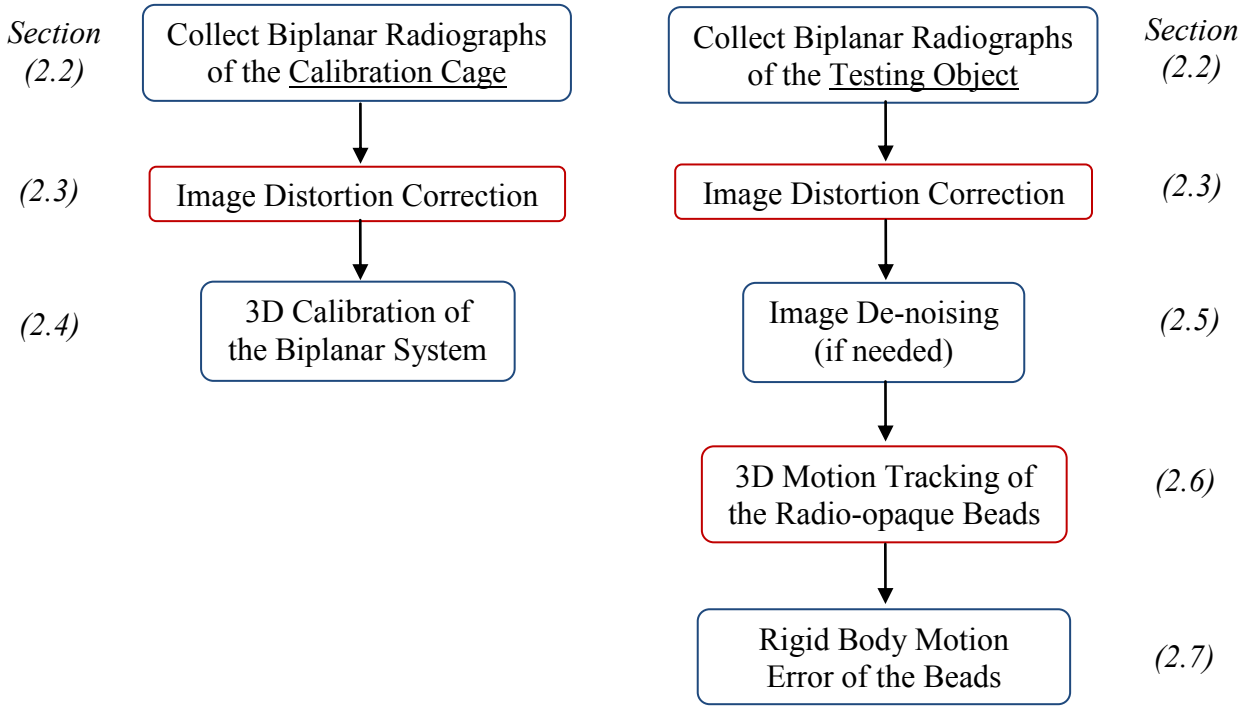

Figure 4. Flow chart of the steps involved in using our biplanar radiography system to track an object of interest. Includes the calibration of the biplanar radiography system in three-dimensions (left pathway) and acquiring biplanar radiographs of a beaded testing object during motion (right pathway).

2.2 Biplanar radiography equipment

The biplanar radiography system that was developed in our laboratory allowed custom placement of two x-ray sources and image intensifiers. While Figure 5 shows the equipment in an orthogonal setup, an advantage of the system was that the x-ray source and image intensifier pairs could be positioned at any relative angle while maintaining the accuracy level. The object of interest was placed in the intersecting capture volume of the two x-ray sources, and images were collected with high-speed video cameras.

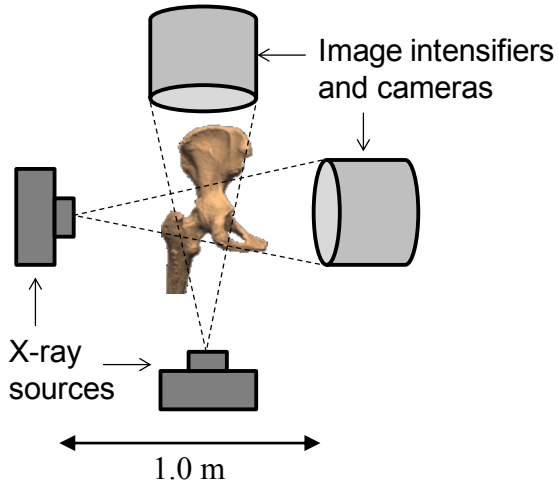

Figure 5. Our biplanar radiography system included two x-ray sources and two image intensifiers instrumented with high-speed cameras. The object of interest was placed within the capture volume of the two x-ray sources.

Each x-ray tube (Comet MXR-160, TSG X-ray, Atlanta, GA) created a continuous beam of x-rays from a point source up to 160kVp and 2.0mA, and was supplied by a 640-Watt generator (Gulmay FC-160, TSG X-ray, Atlanta, GA) (Figure 6a). The corresponding image intensifier (PS93QX-P20, Precise Optics, Bay Shore, NY) was used to convert the radiographs into visible images and had an adjustable field of view (diameters of four, six, or nine inches) (Figure 6b). For all of the subsequent studies in Chapters 3 and 4, a nine inch-diameter field of view was used to allow the largest capture volume in which to position the testing object.

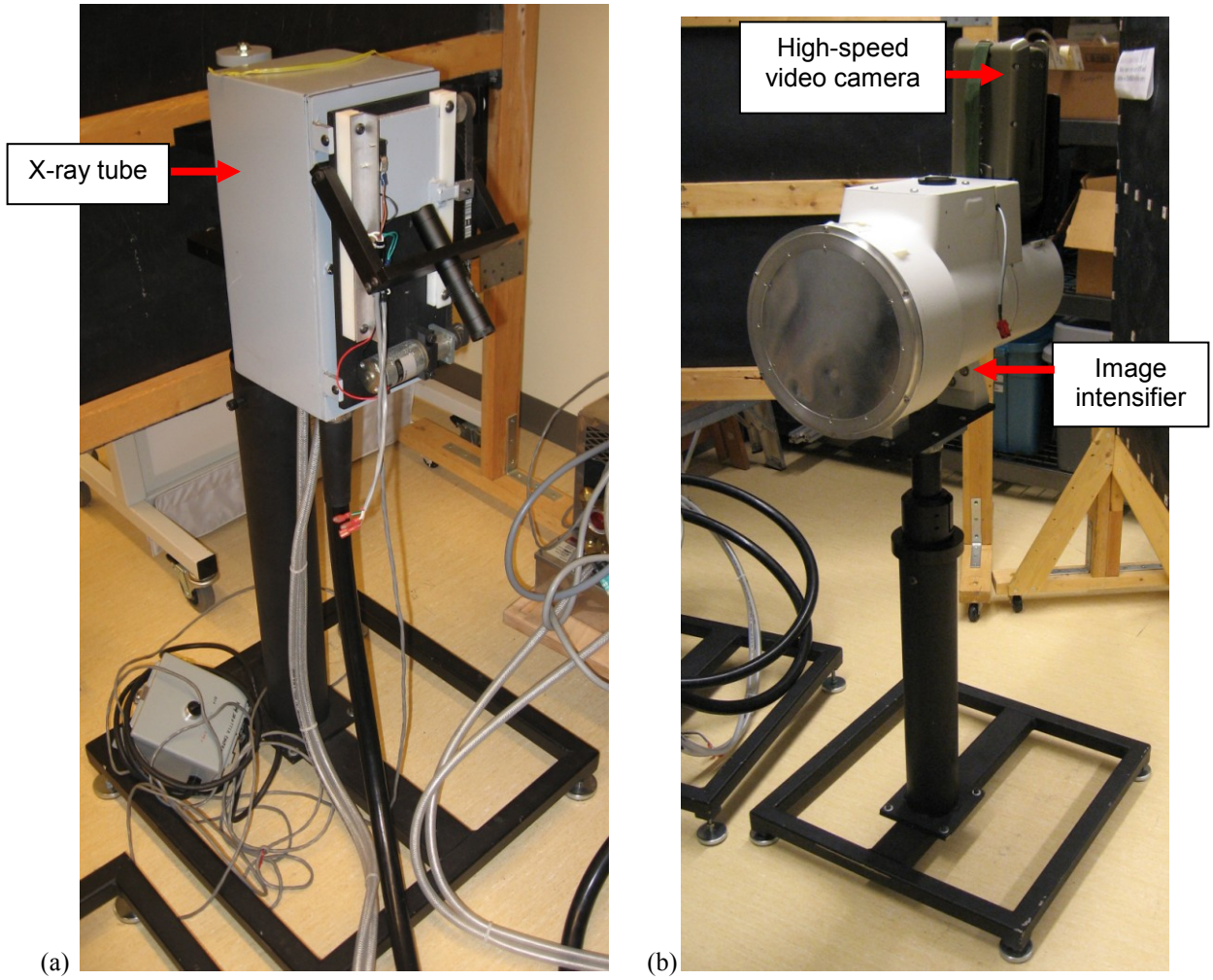

Figure 6. Biplanar radiography equipment included two x-ray tubes (a) and two image intensifiers equipped with high-speed video cameras (b).

For optimal image quality the x-ray tube and image intensifier pairs were separated by a distance of 1.0 metre (Figure 5), producing an optimal amount of radiation per unit area on the image intensifier, as specified by the manufacturer.

Due to the conical shape of each x-ray beam, the x-ray source and image intensifier pairs could be positioned at different relative angles to create varying sizes and shapes of the capture volume. The capture volume increased when the x-ray equipment was positioned so that the testing object was as close to each image intensifier as possible. It was found using solid modeling software (AutoCAD, Autodesk Inc., San Rafael, CA) that when the testing object was located an equal distance from each x-ray source and image intensifier the capture volume was

0.0010m^3 (Figure 7a), whereas when it was located as close to the image intensifiers as possible the capture volume increased to 0.0055m^3 (Figure 7b).

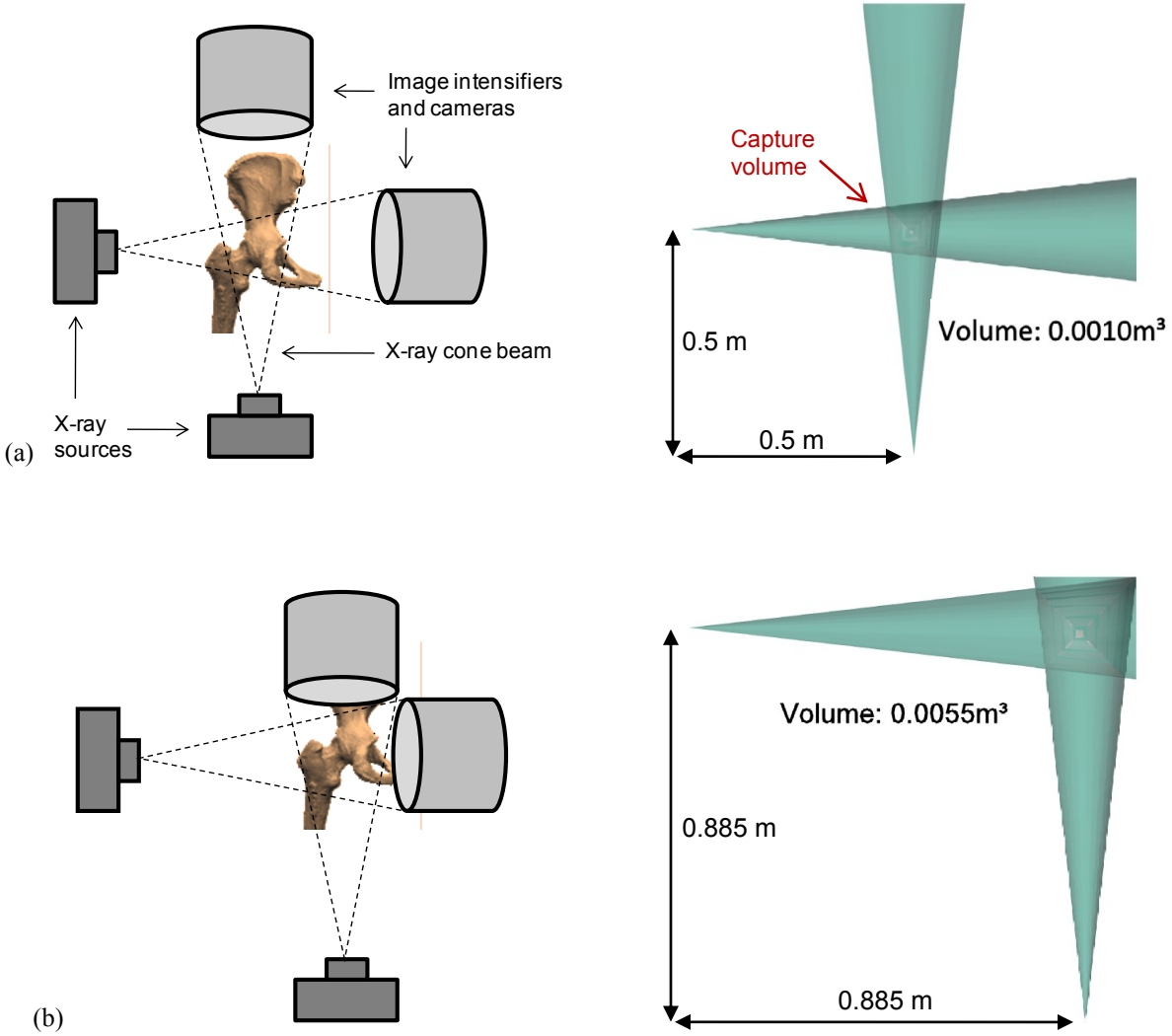

Figure 7. The capture volume increased from (a) when the testing object was located at an equal distance from each image intensifier and x-ray source, to (b) when the testing object was located as close to the image intensifiers as possible.

The size and shape of the capture volume could also be adjusted by changing the relative angle between the x-ray source and image intensifier pairs. At a small relative angle of 30º the capture volume was long and thin, limiting the size of the object that could be imaged (Figure 8a), while a large relative angle of 120º increased the size of the capture volume (Figure 8b). It should be noted that a small relative angle can lead to radiation scatter from one x-ray source onto the neighboring image intensifier, creating high-contrast areas on the edge of the acquired image. This scattering effect is further discussed in Chapter 4.

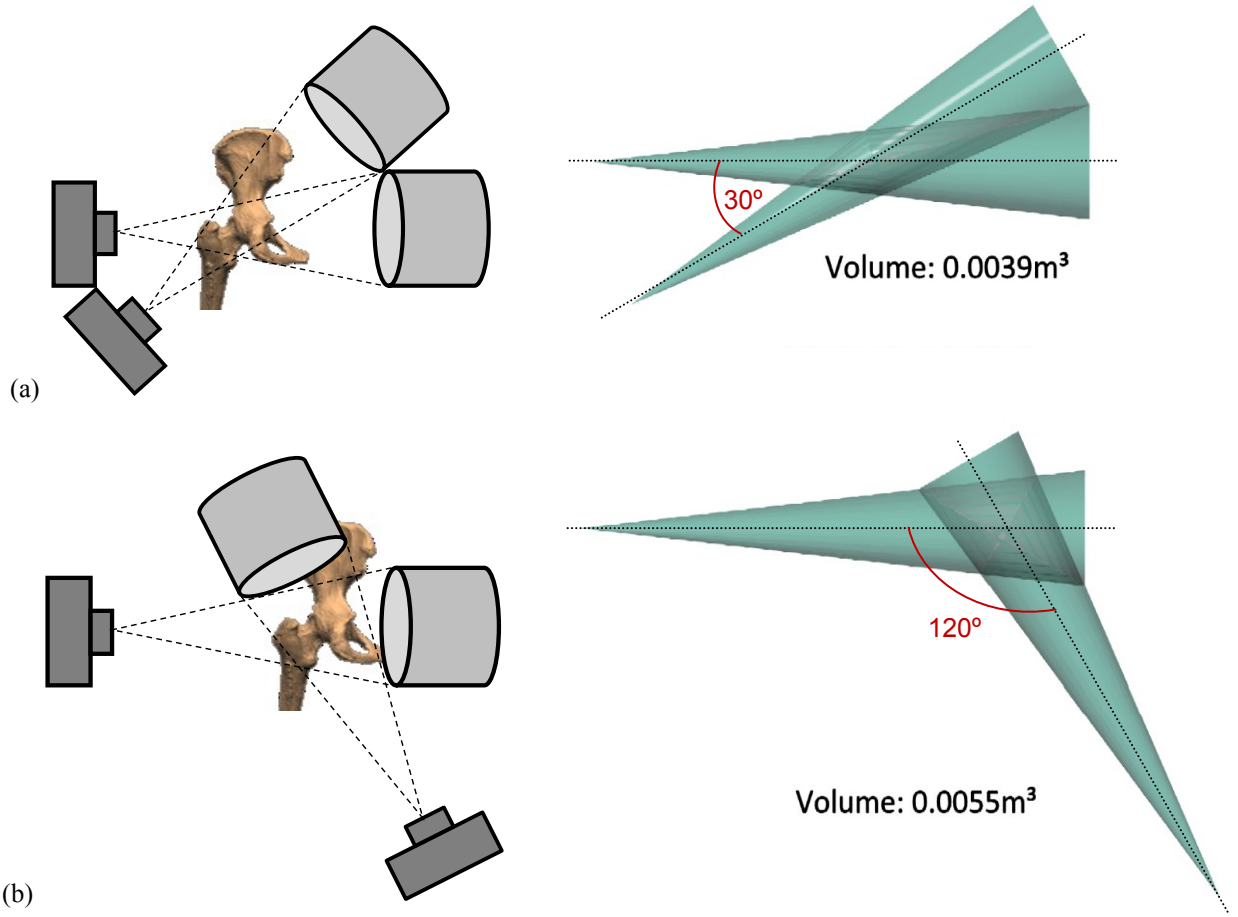

Figure 8. The capture volume changed depending on the relative angle between the x-ray source and image intensifier pairs. (a) A small relative angle of 30° created a long thin capture volume. (b) A large relative angle of 120° created a larger and more compact capture volume.

Custom placement of the x-ray equipment is a considerable advantage of this system, as it allows the shape and size of the capture volume to be adjusted depending on other equipment being used for testing or the shape of the object being imaged.

An alignment object was used to ensure that each x-ray source and image intensifier pair was aligned correctly, with the center of the conical x-ray beam angled orthogonally to the image intensifier plane. The alignment object consisted of a clear plastic cylinder with a radio-opaque bead positioned on each end at the center of the cylinder's face. The cylinder was attached to the center of each image intensifier, which was denoted by a mark on its surface, and slight adjustments were made to the position of the x-ray source and image intensifier until the two radio-opaque beads lined up in the radiographs. If the x-ray source and image intensifier were misaligned, one edge of the image intensifier would receive a higher dose of radiation and create

a varying amount of contrast in the radiographic image. A misalignment could also lead to the x-ray beam missing part of the image intensifier altogether, and therefore not taking advantage of the full capture volume. While a misalignment would be accounted for in the 3D calibration of the system (see Chapter 2.4), this alignment process ensured the radiation was evenly distributed across the face of the image intensifier and improved image quality.

Phantom V12 high-speed video cameras (Vision Research, Wayne, NJ) (Figure 9) were mounted to the back of each image intensifier. The internal camera parameters included 800x800 pixel resolution, 50mm lens focal length, and 20μm pixel size. While the cameras were capable of collecting images up to 60,000 frames per second (fps), the studies in the subsequent chapters of this thesis included static and slow motion tests, and therefore images were collected at 24 fps to allow for a manageable amount of data analysis. Images were recorded by the accompanying software, Phantom Cine Viewer 675 (Vision Research, Wayne, NJ).

Figure 9. Phantom v12 high-speed video cameras (Vision Research, Wayne, NJ) were used to record the radiographic images created within the image intensifiers.

2.3 Image distortion correction

Biplanar radiography systems are subject to image distortion due to projection of the images from a curved surface in the image intensifiers onto a flat surface in the respective cameras. To correct for image distortion, a custom-made grid was used to highlight the variability in the image field of view each time the radiography system was set up for a test session. The grid was a perforated metal sheet (3.0mm hole diameter, 4.6mm center-to-center spacing, 3.0mm thickness, PSC-11618036, Metal Supermarkets, Mississauga, Ontario), which was attached to the face of each image intensifier before testing. A radiograph was acquired of the grid in each camera view and distortion in the grid images was corrected using the open source XROMM (X-ray Reconstruction of Moving Morphology) software developed at Brown University [58].

XROMM was run in MATLAB (The MathWorks, Natick, MA, USA) and used a distortion correction algorithm to compare the spacing between the holes in the biplanar radiographs with the idealized spacing of the holes on the grid. The idealized spacing was found in each radiograph by calculating the average distance between the center hole and each of its six neighboring holes, as distortion was the least at the center of the image. The software calculated a local weighted mean transformation matrix using the *cp2tform* function from the Image Processing Toolbox in MATLAB, with the distorted spacing and idealized spacing of each hole as the inputs for this function. The transformation matrix was then applied to all subsequent image frames acquired in a given test session. Figure 10 shows a radiographic image of the grid before and after distortion correction.

(a) 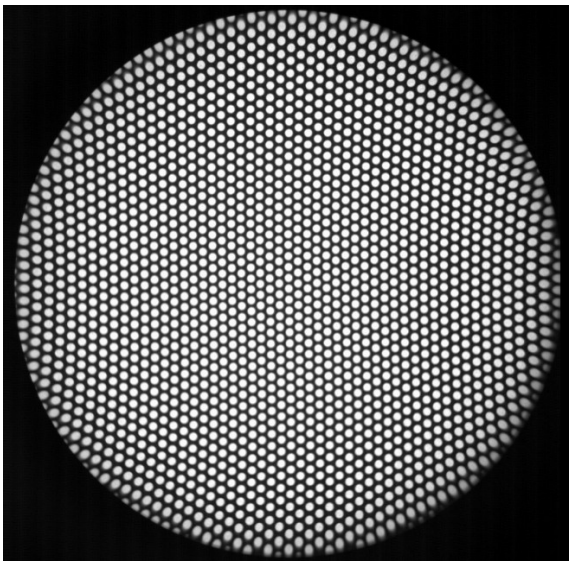 (b) 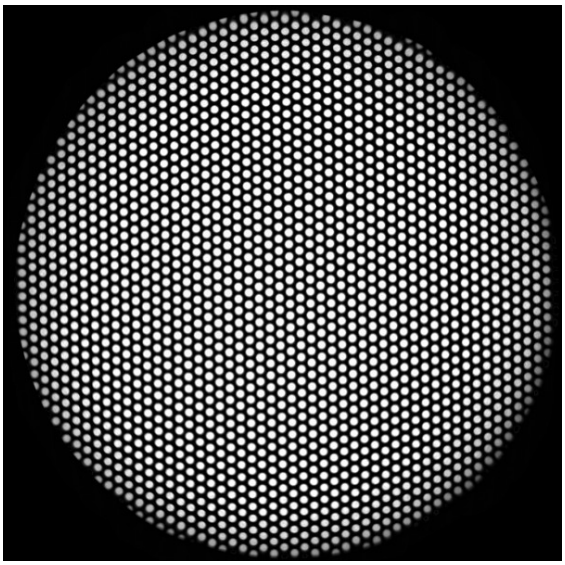

Figure 10. Radiographic images of the grid before (a) and after distortion correction with the XROMM software (b).

A similar approach of distortion correction has been applied in other biplanar radiography studies, using mesh grids, perforated sheets, or regularly spaced bead patterns to develop distortion correction algorithms [22, 34, 58, 59]. The method described above was validated for the current radiography system in previous work by Lucas *et al.* [60] at the University of British Columbia. Lucas *et al.* measured the amount of residual distortion in the grid image after the XROMM distortion correction algorithm had been applied. Lines were created between the centroids of two selected circles, and the distance between the midpoint of the line and the centroid of the center hole was calculated. This was completed five times in each of the vertical, horizontal, and diagonal directions, and an average residual distortion of 0.02 mm was found. Since this

remaining distortion was approximately equal to the precision of tracking radio-opaque beads, it was considered negligible.

2.4 De-noising algorithm

A custom de-noising algorithm was used on the radiographs that were obtained as part of the *ex vivo* study described in Chapter 4, because the soft tissue around the hip specimens produced substantial noise in the images. Figure 11 shows a radiograph of the beads inserted in the femur of one of the hip specimens before and after the de-noising algorithm was applied. The de-noising algorithm was not required for image analysis; however, the semi-automated bead tracking method in TEMA 3D could not consistently identify the beads in the original radiographs. Without de-noising the bead tracking could have been completed manually by selecting the bead centroids in every frame; however to manually select six beads, in over 1300 image frames, in each of the two camera views, would have been extremely time-consuming. While the details of image de-noising are not typically discussed in biplanar radiography studies, Hardy *et al.* mentioned using a custom noise subtraction algorithm on radiographic images of brain tissue during an impact [61].

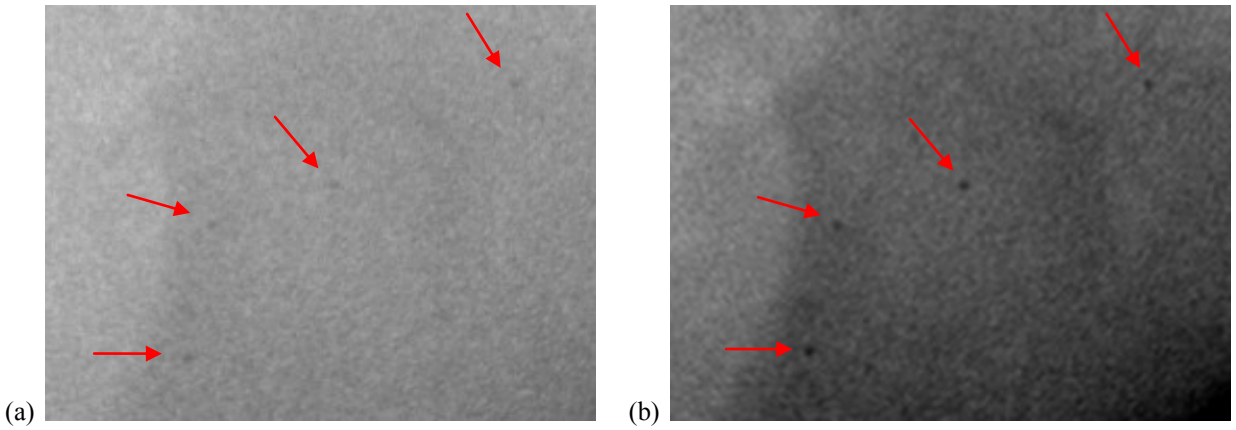

Figure 11. Radiographic images of the radio-opaque beads inserted in the proximal femur of a hip specimen before (a) and after (b) applying the de-noising algorithm.

The de-noising algorithm used in this study was developed by Colin Russell, a M.A.Sc. candidate with the Orthopaedic Injury Biomechanics Group (OIBG) at the University of British Columbia. It was also recently used by Lucas *et al.* [60] in a single-plane radiography study in our laboratory. The custom de-noising algorithm uses a three-dimensional thresholding technique. The algorithm uses *curvelets*, which are shaped like three-dimensional discs of

varying sizes and orientations, and are fit to the high-contrast features in each image. Curvelets that align well with a feature, such as the circular cross-section of a radio-opaque bead, are given a high rating; while curvelets that do not align well with a feature, such as those overlaid on noise, are given a low rating. The lower-rated curvelets are then filtered out based on a specified threshold, which reduces the noise and preserves the features. For a more detailed explanation of three dimensional curvelets, refer to Candes *et al* [62].

2.5 Three-dimensional calibration

The biplanar radiography system was calibrated for each testing session within TEMA 3D (Image Systems, Linköping, Sweden) using biplanar radiographs of a custom-made calibration object. The calibration object was CNC-milled (UBC Machine Shop, Vancouver, BC) to position sixteen stainless steel beads (4.0mm-diameter, McMaster-Carr, Princeton, NJ) within a cylindrical plastic frame (Figure 12). The cylindrical shape of the calibration frame allowed the x-ray source and image intensifier pairs to be positioned at any relative angle around the testing object, provided that all the calibration beads were within the capture volume.

(a)  (b) 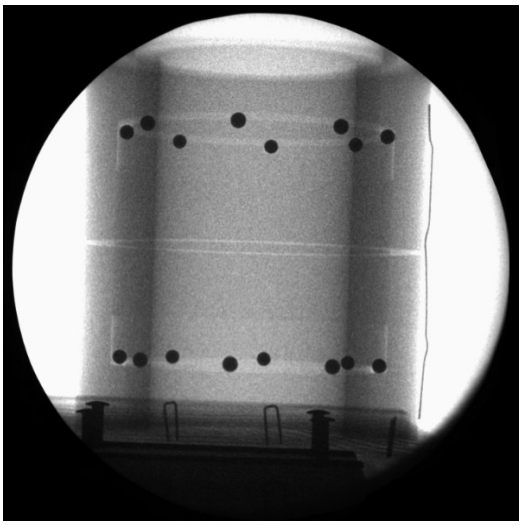

Figure 12. The custom calibration object used for 3D calibration of the biplanar radiography system. (a) Photograph of the calibration object in front of an image intensifier. (b) Radiograph of the calibration object showing the 16 radio-opaque beads.

The beads on the calibration object were selected in each camera view in TEMA 3D, and a centre of gravity algorithm was used to determine their centroids based on a user-defined

intensity threshold. Each bead centroid was described by its x,y-coordinates in the two-dimensional radiograph, which were referred to as its *observed coordinates*.

To calibrate the biplanar radiography system the known locations of the calibration beads and the observed coordinates in the radiographs were used in TEMA to calculate the location and orientation of each camera. The exact algorithms used in TEMA are proprietary software not distributed to the public, and therefore only the broad details are described here. Figure 13 shows the camera geometry; with the *image plane* representing the two-dimensional radiograph, the *optical axis* indicating the orientation of the camera in three dimensions, and the *focal point* of the camera which is located at a known distance along the optical axis (*focal length* = 50 mm for the current cameras). For each camera, lines of sight were drawn from the known coordinates of each calibration bead (from the manufacturing specifications), through the focal point of the camera, and onto the image plane, creating *projected coordinates* of each bead on the image plane. This was repeated for all sixteen beads on the calibration object.

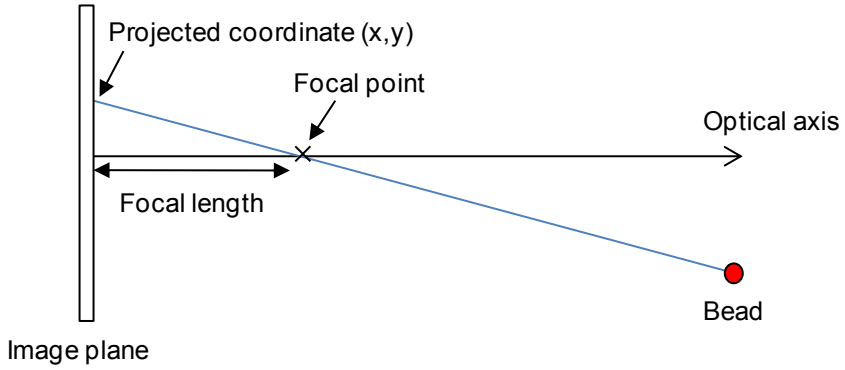

Figure 13. Geometry of each high-speed camera, used to calibrate the biplanar radiography system.

The distance between the *projected coordinates* of a calibration bead and its corresponding *observed coordinates* in the radiograph was measured for each bead and in each camera view. In TEMA these distances were referred to as *image residuals*, and quantified the error in matching the calibration beads to how they appeared in the radiographs. The calibration of the biplanar radiography system was then completed by adjusting the location and orientation of each camera to minimize the sum of the squares of the image residuals. More specifically this process defined the orientation of the optical axis and location of the focal point for each camera (Figure 13), which are necessary for the bead motion tracking step (Chapter 2.6). To quantify the overall

error of the calibration process the root mean square (RMS) of the image residuals was calculated, and included all of the beads in both camera views. The equation for the RMS calculation was as follows (Equation 1), with x representing the image residuals, n representing the number of image residuals (32 for the current calibration cage), and x_{rms} representing the RMS of the image residuals or 3D calibration error. For the current biplanar radiography system, the image residuals were found to be in the range of 0.180 – 0.250 mm, with a 3D calibration error of approximately 0.220 mm.

$$x_{rms} = \sqrt{\frac{{x_1}^2 + {x_2}^2 + \cdots + {x_n}^2}{n}}$$

Equation 1. Root mean square of the image residuals (x_{rms}), or calibration error, was calculated with x representing the image residuals and n representing the number of image residuals (two times the number of calibration beads).

2.6 Motion tracking software

Bead motion tracking was completed using a triangulation method within TEMA 3D. In the first image frame containing the testing object, the beads were selected in each camera view (Figure 14) and a centre of gravity algorithm was used to determine their centroids based on a user-defined intensity threshold. The centroids were described by their x,y-coordinates in the two-dimensional radiographs and referred to as the *observed coordinates* of each bead.

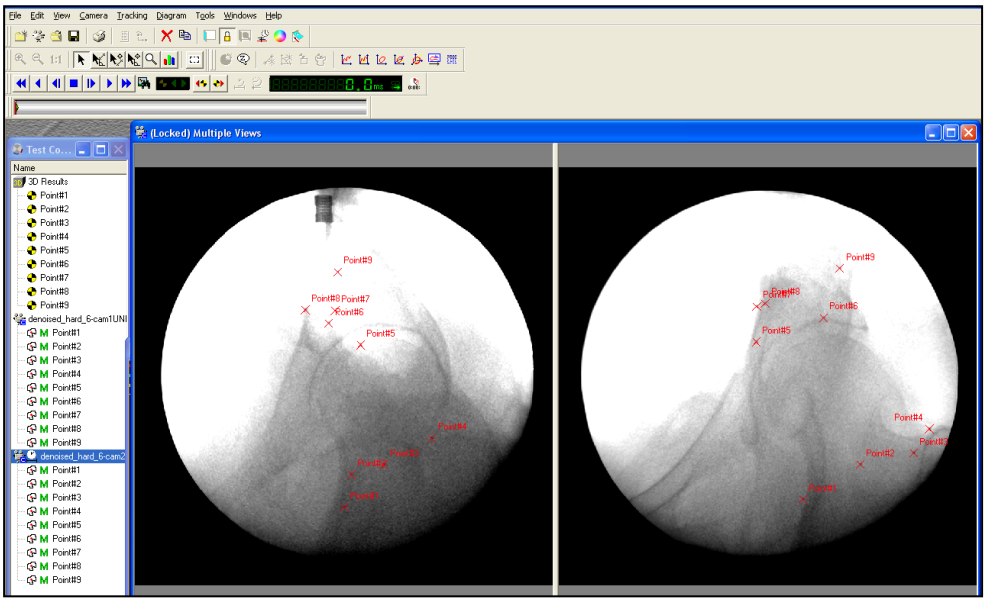

Figure 14. Radio-opaque beads were selected in both camera views in TEMA 3D.

The location and orientation of each camera were determined in the three-dimensional calibration step above (Chapter 2.5), which defined the optical axis and focal point of each camera. To determine the location of a bead in space, lines of sight were traced from the observed coordinates of the bead in each radiograph and through the focal point of the corresponding camera (Figure 15). The intersection point of the two lines of sight was defined as the location of the bead in space. If the lines did not intersect exactly due to error in the calibration, the point at which the lines were closest to intersecting was used as the bead location. This triangulation method was used to compute the location of each bead on a frame-by-frame basis. A semi-automatic tracking algorithm used the trend in a bead's motion to predict its location in the next frame; however, if the bead centroid could not be identified then it was selected manually with a user-defined intensity threshold.

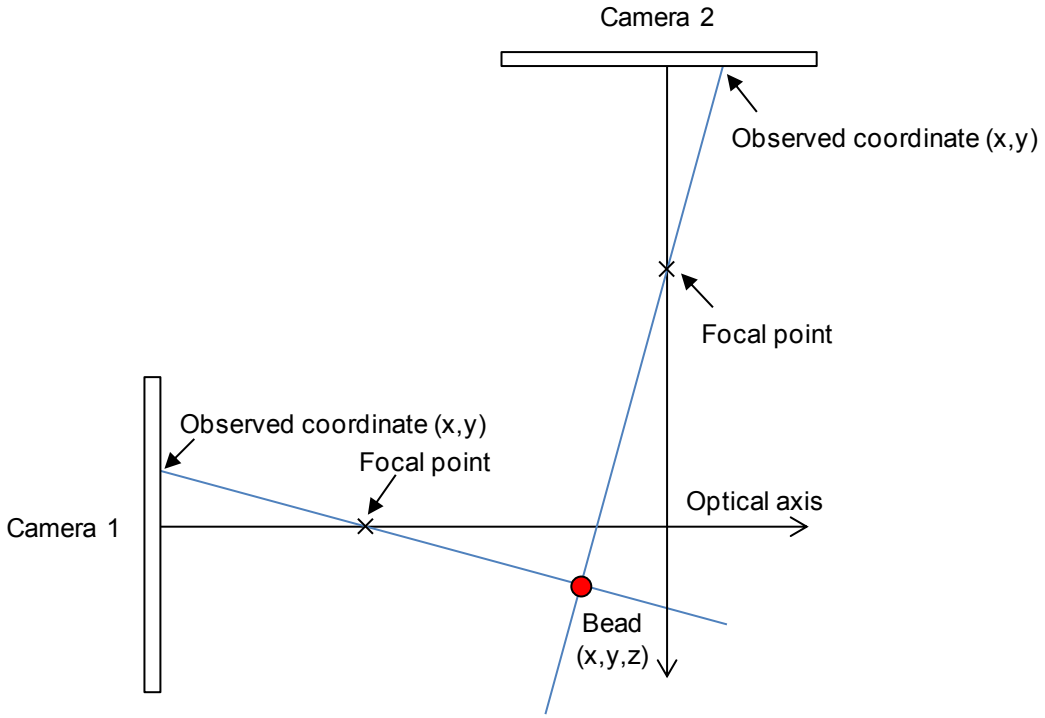

Figure 15. The triangulation method used in TEMA 3D to track the location of the radio-opaque beads. Lines of sight were traced from the observed coordinates of the bead in each radiograph and through the focal point of the camera. The intersection point of these lines of sight defined the location of the bead in space (red circle).

2.7 Rigid body motion error

To confirm that the radio-opaque beads were rigidly attached to the testing object, a rigid body motion error is commonly used in biplanar radiography studies. The relative distances between the beads in the rigid body are calculated for each frame of data, and the mean error in the relative distances is found. The currently acceptable upper limit of rigid body motion error of radio-opaque beads in biplanar radiography studies is 0.350 mm [63]. This upper limit was stated as an agreement of six European research centers in order to standardize biplanar radiography practices [63], as they found that a motion error of less than 0.350 mm ensured a rigid attachment of a bead in the bone.

Chapter 3. Quantifying the Errors Associated with Estimating Cartilage Thickness with Biplanar Radiography and Computed Tomography

3.1 Introduction

Biplanar radiography combined with computed tomography (CT) imaging has been identified as a minimally invasive method of estimating cartilage thickness. By accurately measuring the relative locations of the joint surfaces, cartilage thickness can be estimated across the joint by measuring the minimum distances between the surfaces. Using this imaging technique involves a multi-device multi-step measurement protocol, with each step accumulating a certain amount of error. There is a need for an accuracy assessment of our system's capabilities before *ex vivo* or *in vivo* cartilage thickness measurements can be made. The steps involved for measuring the locations of joint surfaces with biplanar radiography and CT imaging can be summarized as follows:

1. Acquire a high-resolution CT scan of the joint from which the locations of radio-opaque beads inserted in each bone and a 3D surface model of each bone can be segmented.
2. Acquire biplanar radiographs of the joint during an applied load, and quantify bone displacement by measuring the three-dimensional locations of the radio-opaque beads across all image frames.
3. Register the CT bead centroids to their locations determined in Step 2, and apply the same registration to the 3D surface model of each bone. Repeat this for each frame during the applied load, allowing the locations of the joint surfaces to be determined at each frame.

The error in measuring the locations of the radio-opaque beads using biplanar radiography (Step 2) has been used as a standard for comparing the capabilities of biplanar radiography systems in the literature [33-35, 42, 44, 54-56]. Phantom accuracy studies using static image acquisition are most commonly used, in which a rigid body, to which radio-opaque beads are attached, is translated using a precision linear stage [54-57]. Biplanar radiographs are acquired after each displacement, and the displacement of the beads is compared with the applied translations of the linear stage. Using this method a range of bead-tracking errors have been reported in the literature, from 0.018-0.075mm [54-57]. Despite the dynamic capabilities of biplanar radiography systems, static accuracy studies, in which the testing object is stationary during

radiograph acquisition, are most commonly used in the literature and are a sensible first step in the assessment of a biplanar radiography system. With continuous x-ray sources and high-speed cameras for acquiring radiographs, a static assessment can theoretically indicate a system's ability to measure the location of radio-opaque beads during motion. Since our biplanar radiography system was new to the laboratory, a preliminary accuracy assessment was needed to determine its ability to measure the three-dimensional locations of radio-opaque beads and to verify that our system was comparable with those in the literature.

While the error in measuring the locations of beads is often used to compare biplanar radiography systems, the errors that accumulate in the additional steps of estimating cartilage thickness (Steps 1 & 3) have not been reported. An accurate segmentation of the bone surfaces from a CT image (Step 1) is important because this determines the shape of the opposing bone surfaces. Likewise, accurate registration of the bead centroids from the CT image to their locations measured using biplanar radiography (Step 3) ensures that the joint surfaces are correctly oriented in space and ultimately determines how accurately the cartilage thickness can be estimated. To validate this multi-device multi-step method of estimating cartilage thickness, the errors associated with each of steps 1-3 need to be evaluated.

The purpose of this study was to determine the errors associated with estimating cartilage thickness using biplanar radiography and CT imaging, which included two main objectives. The first objective was to do a preliminary accuracy assessment of our biplanar radiography system, which was new to our laboratory, for measuring the locations of radio-opaque beads during static translations. The second objective was to design a phantom hip joint to quantify the errors associated with measuring the locations of joint surfaces during simulated cartilage compression, specifically the error in i) segmenting joint surfaces from a high-resolution CT image, ii) measuring bone displacement using inserted radio-opaque beads, and iii) measuring the locations of the CT segmented joint surfaces in the biplanar radiography coordinate system.

3.2 Materials and methods

3.2.1 Accuracy assessment of the biplanar radiography system

To assess the accuracy of our biplanar radiography system for measuring the location of radio-opaque beads during static translations, beaded phantoms were translated using a precision linear stage while their displacements were measured with biplanar radiography. Two phantoms were made out of polypropylene, with one rigidly mounted on a precision linear stage (Model M4022M, Parker Daedal, Irwin, PA), and the second phantom rigidly mounted to the base of the linear stage as a fixed reference object (Figure 16). These will be referred to as the 'moving' and 'static' phantoms, respectively. Spherical radio-opaque stainless steel beads (1.0mm diameter, McMaster-Carr, Princeton, NJ) were firmly attached with glue (Loctite Super Glue Control Gel, Henkel Corporation, Düsseldorf, Germany) to the outer surfaces of each phantom: six beads to the moving phantom and twelve beads to the static phantom. Stainless steel was chosen as an inexpensive radio-opaque material for a preliminary assessment of our biplanar radiography system, and has been used in other phantom accuracy studies in the literature [54].

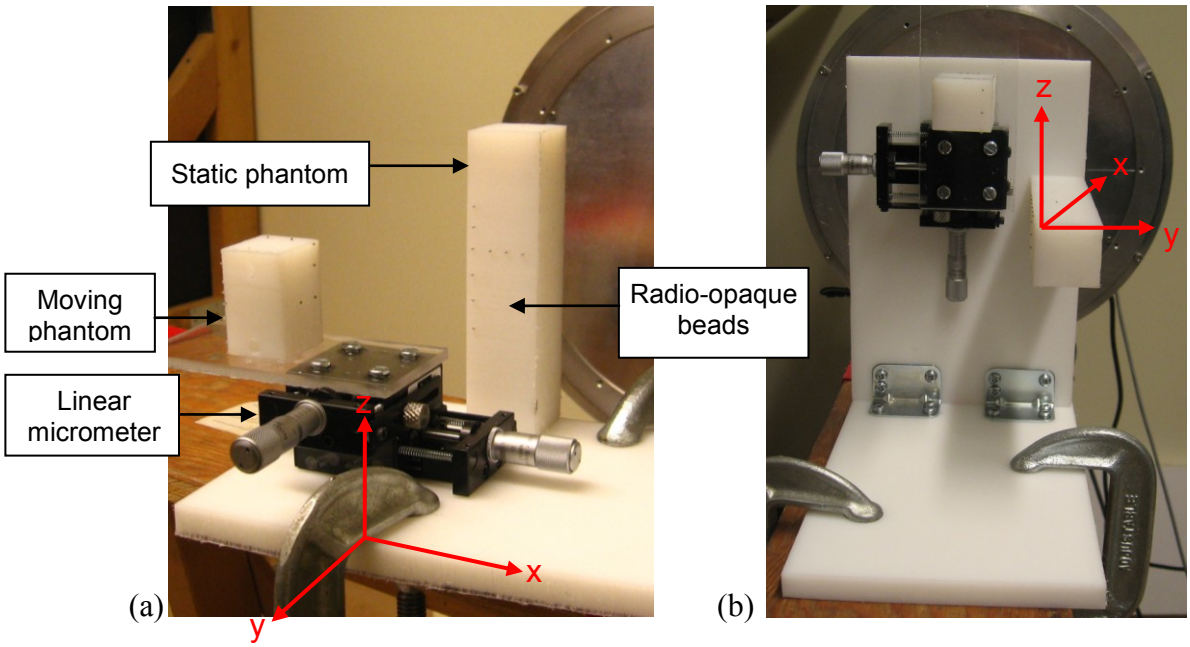

Figure 16. Bead tracking accuracy of the biplanar x-ray system was measured using the static and moving phantoms. Accuracy was measured in the x- and y-directions using the setup in (a) and in the z-direction in the setup in (b).

The biplanar radiography system was set up orthogonally with the center of the capture volume located as close to the image intensifiers as possible to maximize the size of the capture volume.

As described in Chapter 2, three-dimensional calibration of the biplanar radiography system was completed by acquiring biplanar radiographs of a custom calibration object before the testing session. The images were corrected for distortion, and software was used to calibrate the two cameras. See sections 2.2, 2.3, and 2.5 for more details.

To assess the accuracy of our biplanar radiography system for measuring the location of radio-opaque beads, the phantoms were positioned in the center of the capture volume and the moving phantom was displaced relative to the static phantom using the dials on the precision linear stage. The accuracy of the precision stage was ±0.002 mm in both directions, as stated by the manufacturer. The moving phantom was displaced in 0.127mm increments in each of the x, y, and z-axes, to a total displacement of 12.7 mm (or 100 increments) in each direction. The biplanar radiography system was used to acquire 50 image frame pairs of the phantoms at each position at 100kV and 1.0mA. The average positions of the beads over the 50 image frame pairs were used to determine the amount of static image noise in the acquired biplanar radiographs. The voltage and current were applied to both image intensifiers and were chosen for optimal image quality of the radio-opaque beads. To quantify repeatability the phantoms were placed in a single position and 10 sets of 50 image frame pairs were acquired, with the radiography equipment shut off between the acquisitions of each set of images.

As described in section 2.3, all biplanar radiograph frames were corrected for image distortion before analysis. The 3D positions of the beads were then quantified using motion tracking software (TEMA 3D, Image Systems, Linköping, Sweden). Each bead was selected in both camera views, and a centre of gravity algorithm was used to determine the bead centroid. The 3D coordinates of the beads were then semi-automatically determined on a frame-by-frame basis.

The measured displacements of the beads were compared to the known translations of the precision linear stage. Data analysis was completed in MATLAB (The MathWorks, Natick, MA, USA). To eliminate any error created by movement of the testing frame while turning the linear stage dials, the position of the moving phantom was analyzed relative to the static phantom. The centroid of the group of beads on each phantom was calculated, which allowed each phantom to be represented as a single point. The relative displacement of the moving phantom centroid was then determined. The error in bead tracking was defined as the mean difference in the displacement of the moving phantom centroid relative to the manually applied translation of the

linear stage. Repeatability was defined as the standard deviation of the ten repeated measurements of the moving phantom centroid when it remained in a single position.

3.2.2 **Errors in measuring the locations of joint surfaces**

3.2.2.1 Phantom hip

To determine the errors associated with estimating hip cartilage thickness with biplanar radiography and CT imaging, a simple hip joint phantom was created (Figure 17). The acetabulum was represented by a cube of Delrin® thermoplastic (50.8mm x 50.8mm x 38.1mm, McMaster-Carr, Princeton, NJ) with a hemisphere milled into the bottom surface (38.1mm-diameter ±0.025mm, UBC Machine Shop, Vancouver, BC) (see Appendix A: Phantom acetabulum for the design drawing). The femoral head was represented by a sphere of Delrin® (38.1mm-diameter ±0.025mm, McMaster-Carr, Princeton, NJ). This was fixed to a plastic cylinder, representing the proximal femoral shaft, and small polyethylene cubes were glued to the cylinder to represent the greater and lesser trochanters. Spherical radio-opaque tantalum beads (0.8mm-diameter, Tilly Medical, Lund, Sweden) were rigidly attached with glue (Loctite Super Glue, Henkel Corporation, Düsseldorf, Germany) to the phantom hip around the acetabulum, as well as to the femoral neck, greater trochanter and lesser trochanter. Tantalum beads have been used almost exclusively for biplanar radiography studies of articular joints [22, 34, 42, 64], because the material has a high atomic number that allows it to be easily identified in radiographs, and its biocompatibility allows it to be safely implanted in the human body. Biplanar radiography studies of the hip most commonly use 0.8mm-diameter beads, because while larger beads result in a larger image in the radiograph, their contour is more susceptible to distortion in the image which could result in a less accurate calculation of the bead centroid [64]. Bead locations (see Figure 17) were based on work by Lawrie *et al.* [65], which defined a bead placement protocol in the hip that minimized bead overlap in the biplanar radiographs.

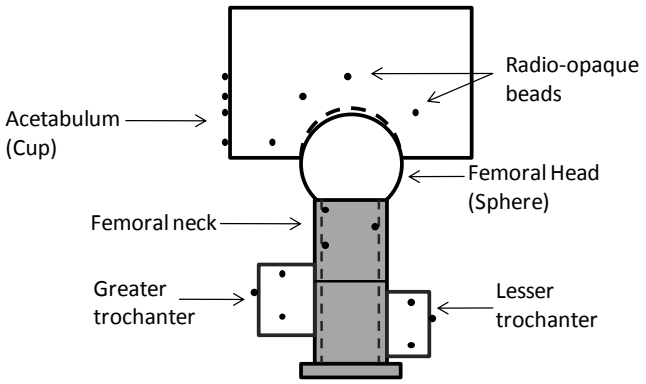

Figure 17. A simplified hip joint phantom modeled after the proximal femur and acetabulum, with radio-opaque beads attached at representative anatomical locations.

3.2.2.2 Segmenting joint surfaces

A high resolution computed tomography (CT) image was acquired of the phantom hip (Toshiba Aquilion helical CT, Canadian Diagnostics Center, Vancouver, BC) with the following imaging specifications: 0.5mm isotropic voxels, 0.5mm slice thickness, 500s exposure time, 300A x-ray tube current, 512 x 512 field of view. Analyze (Mayo Clinic, Rochester, MN) was used to locate the surfaces of the cup and sphere relative to their respective beads. The locations of the beads were determined by thresholding the CT images to isolate the voxels that made up each bead. For each set of voxels, corresponding to a single bead, their centroid was found based on a weighted grayscale. The surfaces of the cup and sphere phantoms were manually segmented in a slice-by-slice fashion, using a semi-automated region growing technique was used to identify the boundaries of the cup and sphere surfaces based on a user-defined pixel intensity threshold. Three-dimensional surface models of the cup and sphere were extracted using an adaptive deformation algorithm (Figure 18), with the sphere surface containing 13833 points and the cup surface containing 12244 points.

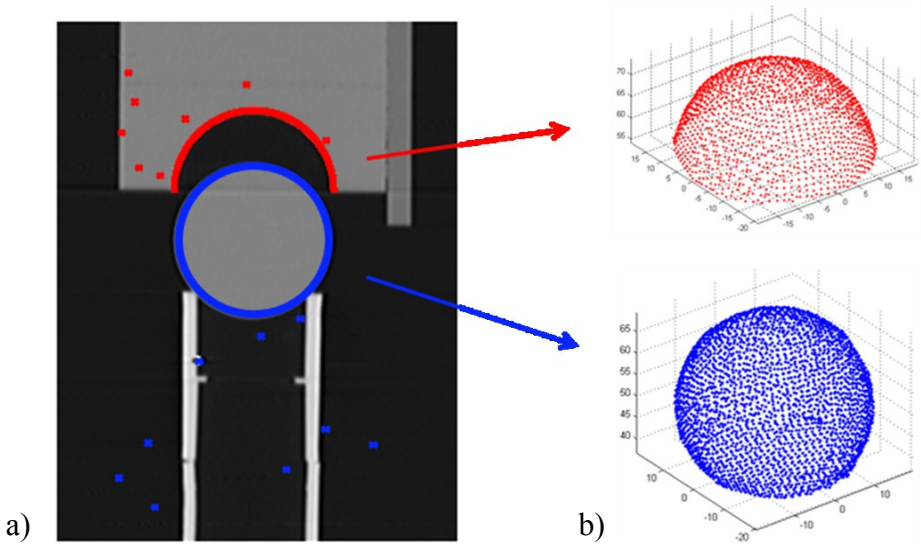

Figure 18. (a) Computed tomography scan of the phantom, with the beads attached to the cup (red points) and the sphere (blue points), as well as the segmented surfaces of the respective phantoms. (b) 3D surface models of the cup (red) and sphere (blue), extracted using an adaptive deformation algorithm.

To determine the error in the segmented phantom surfaces, the cup and sphere were digitized using a coordinate measuring machine (Contura, Carl Zeiss AG, Oberkochen, Germany) with a ±0.002mm accuracy, which provided a reference standard measurement of the shape of the surfaces. The digitized surfaces were measured in concentric circles, with each circle separated by an elevation of 1.27mm (Figure 19). The top half of the sphere was digitized and contained 12389 points, while the cup contained 10578 points.

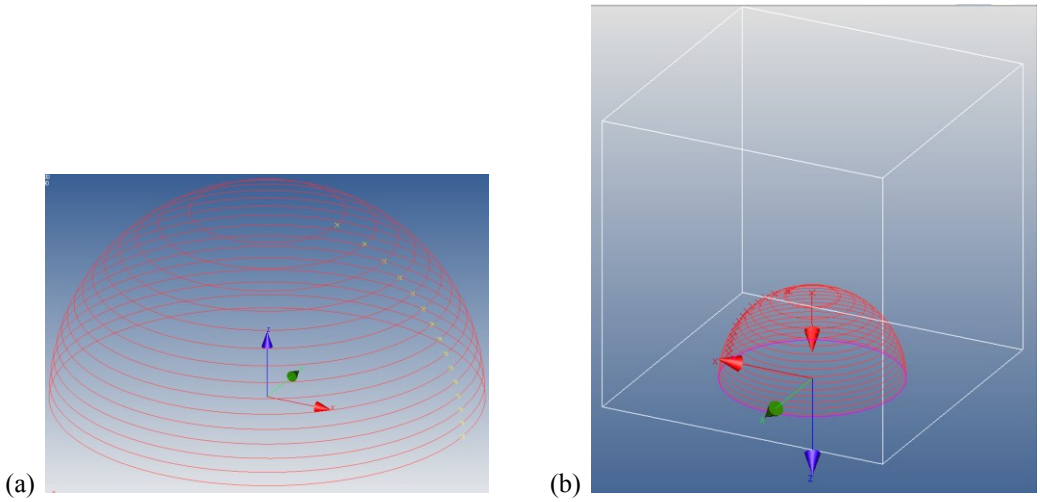

Figure 19. Digitized surfaces of the sphere (a) and cup (b) using a coordinate measurement machine.

The segmented sphere and cup surfaces were aligned with their corresponding digitized surface using a least-squares based registration algorithm [66] (a further description of the algorithm can be found in section 3.2.2.4). The minimum distance from each point on the digitized surface to the segmented surface was calculated to quantify the error at each point. The mean error was defined as the error in segmentation, and was calculated for each of the sphere and cup.

3.2.2.3 Measuring bone displacement

The sphere (proximal femur) and cup (acetabulum) were each mounted to precision linear stages (Model M4022M, Parker Daedal, Irwin, PA), which allowed translations in two directions (Figure 20).

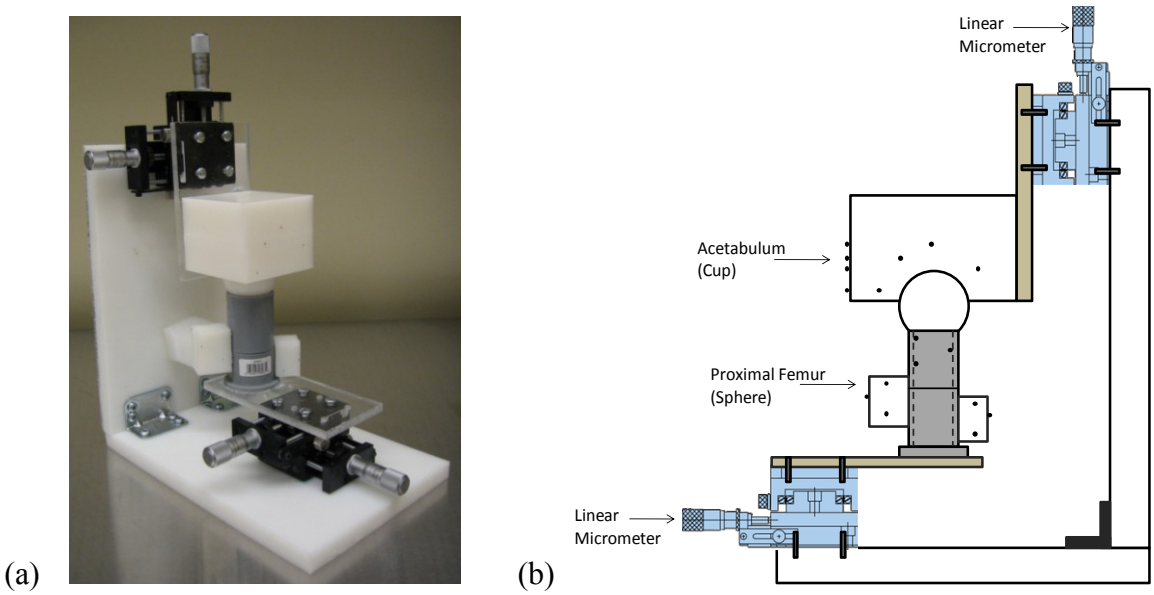

Figure 20. A photograph (a) and schematic (b) of the phantom hip joint used to measure surface proximity accuracy.

The dials on the two linear stages were used to position the phantom hip surfaces so that the sphere was contained within the cup, with a space between the surfaces to simulate hip cartilage. This alignment was created by first positioning the sphere almost entirely contained within the cup, and adjusting its position until an equal amount of space separated it from the cup circumference on all sides. The cup was then translated inferiorly until contact between the surfaces could be detected as resistance in the dial. To simulate the presence of hip cartilage, the cup was translated superiorly 2.0mm to create a baseline separation between the surfaces, which is the approximate thickness of hip cartilage under maximum deformation [10, 12].

The biplanar radiography system was set up orthogonally around the phantom hip; with the capture volume located as close to the image intensifiers as possible. As described in Chapter 2, the system was calibrated by acquiring biplanar radiographs of a custom calibration object and computing the position and orientation of each camera in TEMA 3D (Image Systems, Wayne, NJ). A mean calibration error was found across the different test sessions.

The phantom hip was positioned so that the sphere and cup surfaces, as well as their respective beads, were located within the capture volume. The cup was translated superiorly to simulate increments of hip cartilage deformation, with biplanar radiographs acquired at each increment. The cup was translated superiorly in 0.050mm increments to a total displacement of 1.0mm from its baseline position. Repeatability was assessed by returning the cup to the baseline position and repeating the following displacements: 0mm, 0.25mm, 0.50mm, 0.75mm, and 1.00 mm. The biplanar radiography system was used to acquire 50 image frame pairs of the phantoms after each incremental displacement at 100kV and 1.0mA. The voltage and current were applied to both image intensifiers and were chosen for optimal image quality of the radio-opaque beads. The average positions of the beads over the 50 image frame pairs were used to account for static image noise in the acquired biplanar radiographs.

As described in Chapter 2, the locations of the phantom proximal femur and acetabulum were measured at each imaged position by tracking the beads attached to each phantom in TEMA 3D (Image Systems, Wayne, NJ). The output of the software was the three-dimensional coordinates of the beads in the biplanar radiography coordinate system for each frame during the applied loading. The measured displacements of the beads on each of the phantom proximal femur and acetabulum were compared to the known translations of the precision linear stage. Data analysis was completed in MATLAB (The MathWorks, Natick, MA, USA). To eliminate any error created by movement of the testing frame while turning the linear stage dial, the position of the acetabulum was analyzed relative to the proximal femur. The centroid of the group of beads on each phantom was calculated, which allowed the displacement of each phantom bone to be described by the motion of a single point. The relative displacement of the acetabulum was then determined at each imaged position. The error in measuring bone displacement was defined as the mean difference in the displacement of the acetabulum relative to the manually applied translation of the linear stage.

3.2.2.4 Measuring the locations of joint surfaces

To measure the locations of the joint surfaces at each imaged position, the CT-segmented surfaces of the phantom femoral head and acetabulum were registered to the locations of their corresponding radio-opaque beads at each frame. The three-dimensional locations of the radio-opaque beads were measured in the biplanar radiography coordinate frame using TEMA 3D software (see Chapter 2). The locations of the beads measured in the CT coordinate system were registered with their corresponding locations in the biplanar radiography coordinate system using a least-squares based registration algorithm [66] in MATLAB. The input into the algorithm was the location of the beads in the biplanar radiography coordinate frame, called the *data_set*, and the corresponding locations of the beads in the CT coordinate frame, called the *model_set*. The centroid of each group of beads in the data_set and model_set was calculated, and the translation vector that aligned the model_set centroid with the data_set centroid was defined. The group of model_set beads were then rotated around its centroid until the least-squared distances between the data_set and model_set beads were minimized. A transformation matrix between the original location of the model_set in the CT coordinate frame and its new location in the biplanar radiography frame was defined. This was completed separately for the beads attached to the sphere and the beads attached to the cup, to determine the location of each rigid body. The transformation matrix used to register the bead locations was then applied to the extracted surfaces of the cup and sphere, which allowed the locations of the surfaces to be defined relative to their beads (Figure 21). The registration process was applied to the beads and joint surfaces at every frame, which allowed the locations of the sphere and cup to be measured at each imaged position.

The output of the registration algorithm was the distance between each pair of registered beads, otherwise defined as the distance between each bead in the data_set and its corresponding registered bead in the model_set. In Figure 21 this is demonstrated in the enlarged section, where the distance between the bead tracked in the biplanar radiography coordinate system (circle) and the corresponding registered bead from the CT coordinate system (diamond) is shown. The mean distance between each pair of registered beads was calculated across all imaged positions.

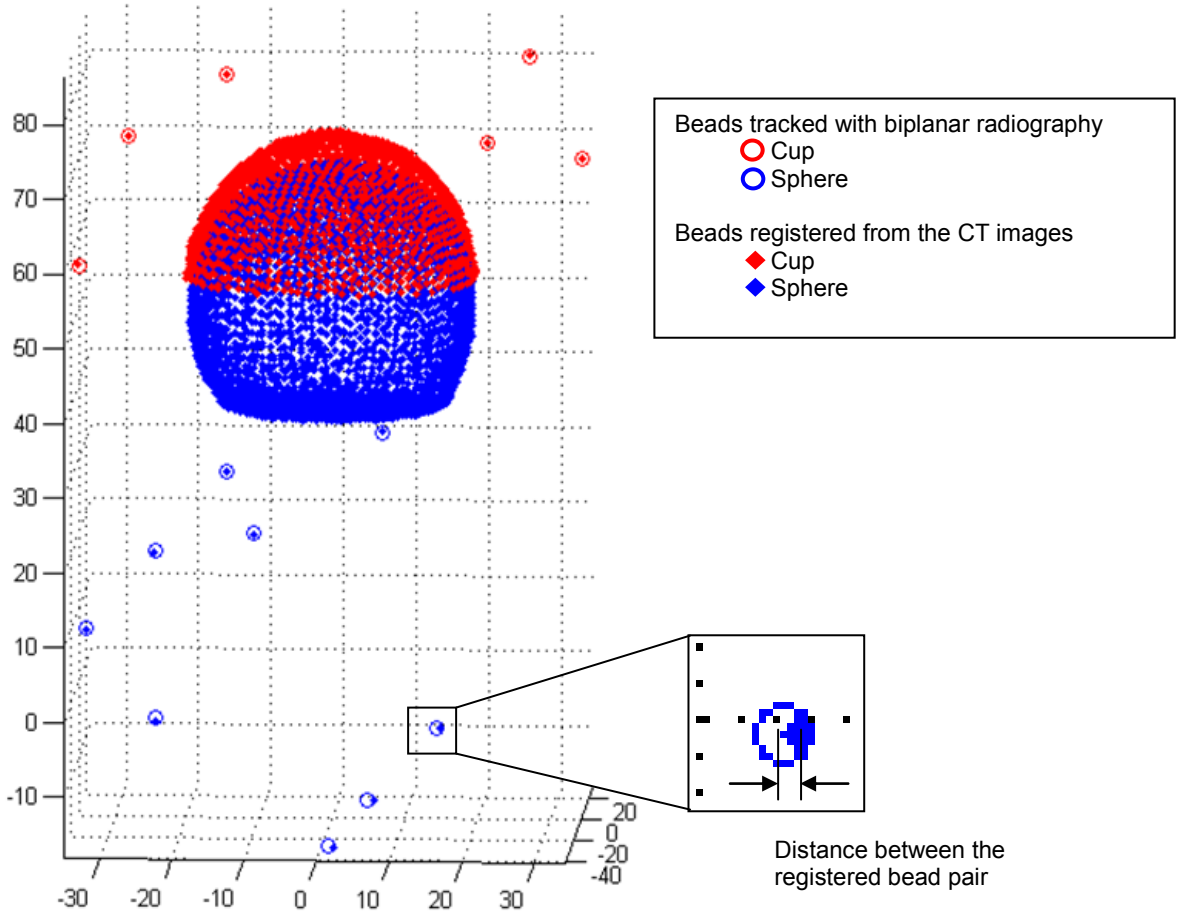

Figure 21. The biplanar radiography coordinate frame, showing the beads identified in the biplanar radiographs (circles) and the beads registered from the CT coordinate system (diamonds). The extracted surfaces of the sphere (blue) and cup (red) were also transformed into the biplanar radiography coordinate frame. The enlarged section demonstrates the distance between the biplanar radiography bead and its corresponding registered CT bead.

To determine the error in measuring the locations of the joint surfaces, a computer model was used to simulate the phantom experiment. The simulation was performed using custom-written software in MATLAB. From the baseline positions of the phantom sphere and cup surfaces, as described in the phantom study above (section 3.2.2.1), the cup was translated superiorly relative to the sphere in ideal 0.050mm increments. The direction of the cup displacement was simulated by fitting a trend line to the phantom cup translation data using a linear least squares method. This was completed in case the linear micrometer used to translate the phantom cup was not positioned perfectly vertical. The model cup was then translated in 0.050mm increments along this trend line to a total displacement of 1.0mm (Figure 22). The model provided ideal joint surface locations with which to compare the phantom study.

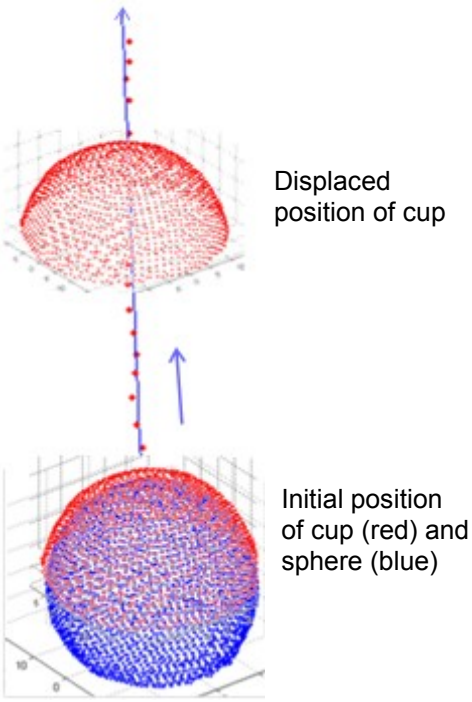

Figure 22. The phantom experiment was simulated by translating the phantom cup surface in ideal increments of 0.050mm. The direction of translation was determined by fitting a trend line (blue line) to the phantom displacement data (red points). The displacements are greatly exaggerated in this figure for visualization purposes.

Using the locations of the joint surfaces at each imaged position, cartilage thickness was estimated across the joint by measuring the minimum distances between the joint surfaces at every point. This was completed for both the phantom hip as well as the computer model. The minimum distance between the joint surfaces was calculated from each point on the cup surface to the closest point on the sphere. For each imaged position, the mean cartilage thickness was calculated over the entire joint, as well as for smaller regions of interest. The femoral head of the hip was divided into five anatomical regions: anterior, posterior, superior, medial, and lateral (Figure 23), as done in the literature [67]. The anatomical regions were identified on the sphere and cup based on the approximate location of the greater and lesser trochanters on the femoral head phantom.

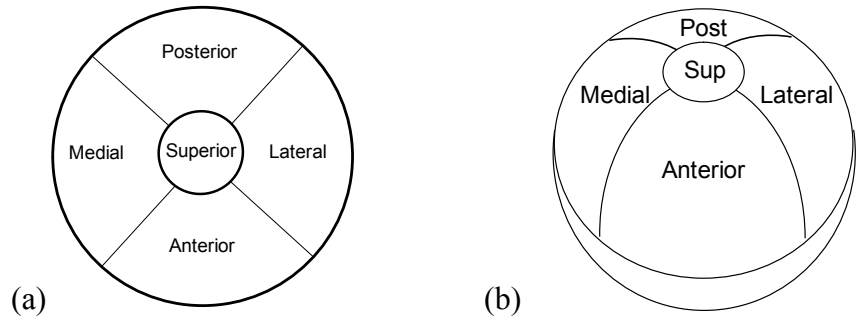

Figure 23. Anatomical regions of interest were defined on the phantom joint surfaces (superior, medial, posterior, lateral, and anterior). (a) Superior view of the regions, (b) 3D representation of the regions on the sphere surface.

The error in measuring the locations of joint surfaces was defined as the difference in the mean cartilage thickness measured in the phantom experiment relative to that predicted by the computer model. A mean error was found for each region of interest, as well as across the entire surface. This overall error of measuring the locations of the joint surfaces inherently assessed the error in measuring the locations of radio-opaque beads and registering the segmented joint surfaces to the bead locations. Repeatability of the cartilage thickness measurements was analyzed using the five imaged positions in which the measurements were repeated (0mm, 0.25mm, 0.50mm, 0.75mm, and 1.00 mm). The difference in the mean cartilage thickness measured in the phantom experiment relative to that predicted by the computer model was calculated for each imaged position, and repeatability was defined as the mean of these differences.

3.3 Results

3.3.1 Calibration of the biplanar radiography system

The calibration of the biplanar radiography system was completed as described in Chapter 2, and a mean calibration error of 0.123±0.031mm (mean ± standard deviation) was found over all testing sessions. This value represented the error in matching the known coordinates of the beads on the calibration object with their measured locations in the biplanar radiographs.

3.3.2 Accuracy assessment of the biplanar radiography system

The radio-opaque beads attached to the static and moving phantoms were clearly visible in the biplanar radiographs (Figure 24), and therefore de-noising was not required for image analysis.

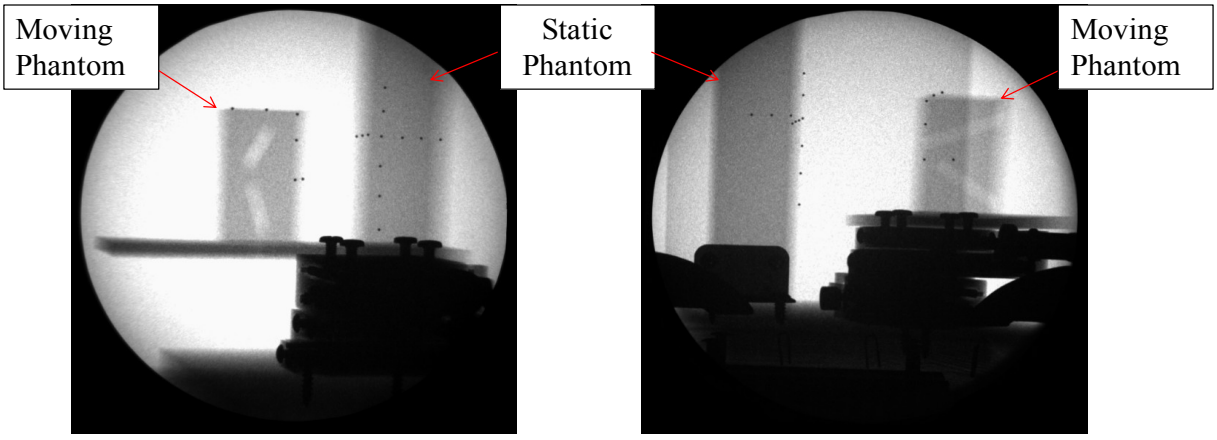

Figure 24. Biplanar camera views of the phantom setup, showing the static and moving phantoms with radio-opaque beads attached.

Within each set of 50 frame pairs, which were acquired with the phantoms in a static position, the measured locations of the bead centroids had a mean uncertainty of 0.034±0.023mm. This uncertainty was likely due to image noise, which appeared as varying image contrast within each radiograph from frame-to-frame, and caused the pixel intensity-weighted centroid of each bead to shift slightly between frames. To account for this variability the mean location of each bead over the 50 frames was used.

The errors in measuring the locations of radio-opaque beads are summarized below for each of the orthogonal axes, as well as the precision of the measurements (Table 2).

Table 2. The bead tracking error in each axis (± standard deviation), the mean error across all axes, and the precision of bead tracking measurements are summarized below. The error in bead tracking was measured across 100 increments of 0.127mm along each orthogonal axis, and precision was measured across ten biplanar radiographs with the beads remaining in a single position.

X-axis	0.010 ± 0.007mm
Y-axis	0.009 ± 0.007mm
Z-axis	0.018 ± 0.009mm
Mean Bead-Tracking Error	**0.012 ± 0.008mm**
Precision	**0.006mm**

3.3.3 **Errors in estimating cartilage thickness**

3.3.3.1 Error in segmenting joint surfaces

The mean error in the segmented sphere surface was 0.166±0.073mm (mean±standard deviation), with a maximum error of 0.500mm, as measured relative to the CMM digitized surface (Figure 25a). The mean error in the segmented cup surface was 0.138±0.063mm, with a maximum error of 0.509mm (Figure 25b).

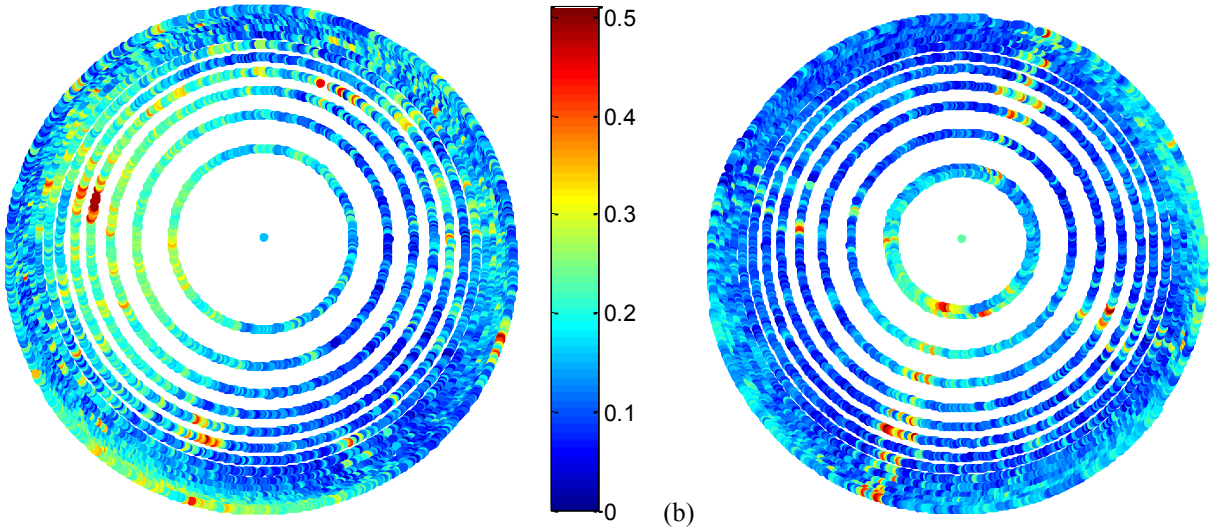

Figure 25. Difference between the segmented surfaces and digitized surfaces for the sphere (a) and cup (b), in mm. Displayed from a superior view of the digitized surfaces, with each point on the surface colour-coded to show low errors in blue and high errors in red.

3.3.3.2 *Error in measuring bone displacement*

The beads were clearly visible in the biplanar radiographs (Figure 26), and therefore image de-noising was not required for image analysis.

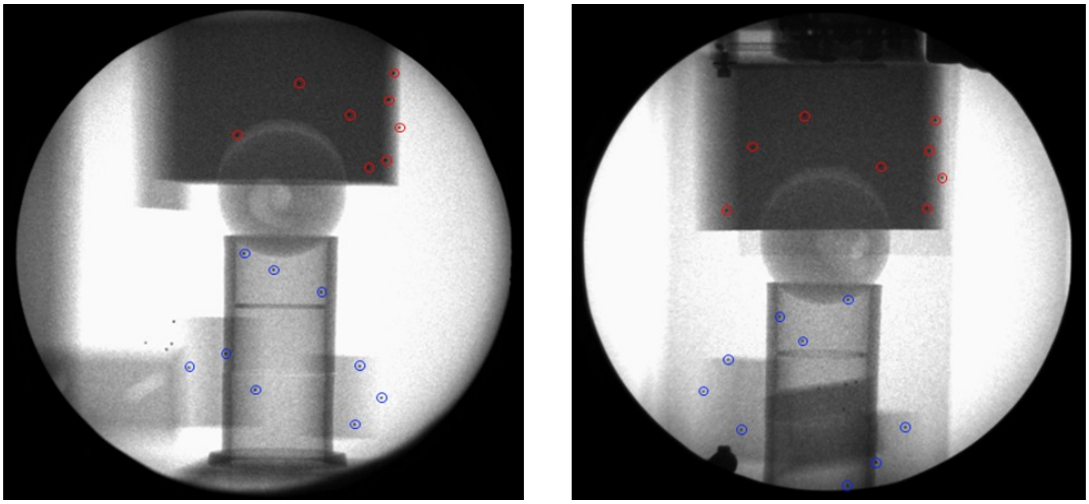

Figure 26. Biplanar radiographs of the phantom hip. The three-dimensional motion of the beads rigidly attached to the cup (circled in red) and the sphere (circled in blue) was tracked using motion tracking software (TEMA 3D).

The measured displacements of the beads attached to the cup closely followed the translations of the precision linear stage (Figure 27), with a mean error in the bead displacements found to be 0.002±0.004mm. This error was measured across the twenty incremental displacements of 0.050mm of the cup relative to the sphere.

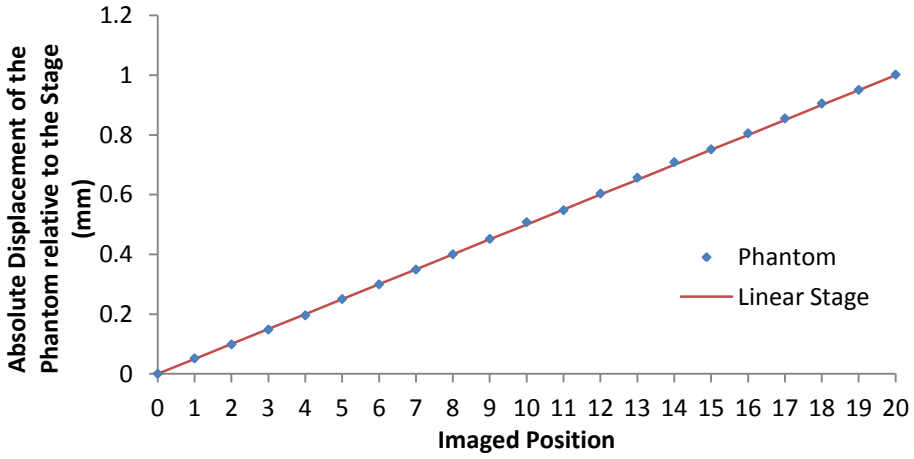

Figure 27. Displacement of the cup relative to the precision linear stage at each imaged position. Phantom displacement was based on the centroid of the beads attached to the cup relative to the centroid of the beads attached to the sphere.

3.3.3.3 Error in measuring the locations of joint surfaces

The mean distance between each pair of registered beads was 0.157±0.003mm (mean±standard deviation) for the cup surface and 0.185±0.004mm for the sphere surface. The mean distance was calculated across all frames by registering the locations of the beads on each surface from the CT image to the locations of the corresponding beads in the biplanar radiographs.

The error in measuring the location of joint surfaces, defined as the mean difference between the measured and model cartilage thickness results, was 0.010±0.005mm (mean±standard deviation) when measured over the entire surface. Repeatability of the cartilage thickness measurements was within 0.006mm, as found for the repeated measurements at five positions of simulated cartilage deformation (0.00mm, 0.25mm, 0.50mm, 0.75mm, and 1.00mm). The error in the mean cartilage thickness in each region of interest is summarized in Table 3. The error in measuring the locations of joint surfaces included the error that accumulated from measuring the locations of the radio-opaque beads and registering the segmented joint surfaces to the bead locations.

Table 3. Difference between the mean cartilage thickness measured using biplanar radiography and CT imaging and the cartilage thickness predicted by the computer model for each region of interest.

Region of Interest	**Difference Between the Measured and Model Mean Cartilage Thickness (mm)**
Superior	0.005 ± 0.003
Medial	0.007 ± 0.006
Posterior	0.006 ± 0.005
Lateral	0.009 ± 0.007
Anterior	0.003 ± 0.003

3.4 Discussion

The ability of our biplanar radiography system to measure the locations of radio-opaque beads, with an average bead tracking error of 0.012±0.008mm and precision of 0.006mm, was comparable to other static accuracy studies in the literature, which reported bead measurement errors of 0.018-0.075mm and precision values of 0.006-0.016mm [54-56]. This level of accuracy for measuring three-dimensional motion is a considerable advantage of biplanar radiography over other imaging systems, such as optoelectronic motion capture, which has a positional accuracy of 0.100mm (Optotrak Certus Motion Capture System, Northern Digital, Waterloo, Canada).

The variability in the bead measurement error between the three orthogonal axes, in which the error in the z-axis was slightly higher, can be explained by the location of the beads on the calibration object. The beads were positioned on the cylindrical calibration object in two concentric rings of eight beads, with each ring centred around the z-axis (Figure 28). As a result there was a wider range of bead coordinates in the xy-plane for calibrating the biplanar radiography system in the x- and y-directions, while the limited range of coordinates in the z-direction may have caused a less accurate calibration of the system for the z-axis.

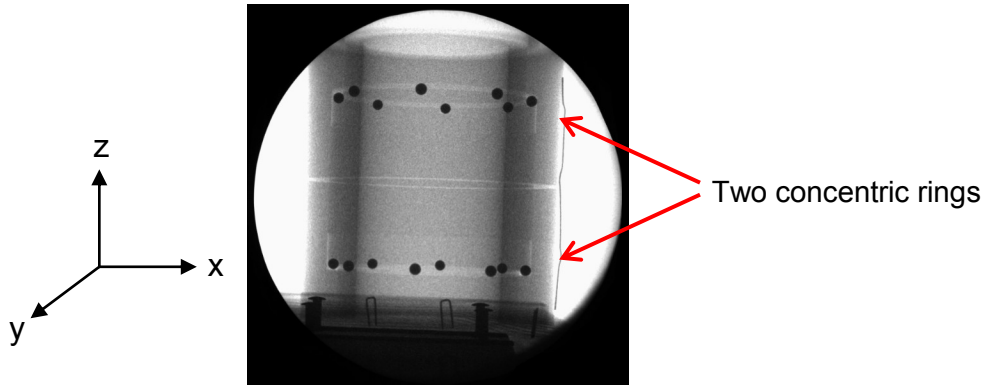

Figure 28. The calibration beads were positioned on the cylindrical calibration object in two concentric rings around the z-axis, which likely caused a slightly higher bead measurement error in the z-axis.

The error in segmenting the phantom joint surfaces (0.166 ± 0.073mm and 0.138 ± 0.063mm, for the sphere and cup respectively) was due to the limits of the CT image resolution. A pixel intensity threshold was selected to identify the surface boundaries, which could create error in the segmented surfaces. The segmentation error was minimized by segmenting the surfaces in each of the orthogonal planes (coronal, sagittal, transverse) and using all of the included data to

extract the 3D surface model. This would especially minimize the error at the outer edges of the spherical surfaces. If only one segmentation plane had been used then the slice thickness of 0.5mm could allow the surface edges to fall in between the image slices and not be included in the surface extraction. As expected, the segmentation errors found for the smooth phantom surfaces were less than the segmentation errors found for *ex vivo* hip joints in the literature [68, 69], which involve more difficult segmentations of irregular bone surfaces. For example, Rathnayaka *et al*. [68] reported the accuracy of using an intensity threshold segmentation technique was 0.180±0.020mm, which was found by comparing the segmented surface models of five ovine femur bones from CT images to their corresponding digitized surfaces, which were measured using a coordinate measuring machine. It is possible that the segmentation error reported for phantom surfaces could increase in an *ex vivo* study of the hip joint, due to the irregular bone surfaces and inclusion of soft tissue around the joint. However, cortical bone has a high density that is easily identifiable in CT images and segmentation of bone surfaces has been completed with comparable accuracy to our phantom in the *ex vivo* hip joint [68, 69].

After registration of the CT bead locations to the bead locations in the biplanar radiography coordinate frame, the mean distance between the registered bead pairs (0.157±0.003mm and 0.185±0.004mm, for the cup and sphere respectively) was comparable to registration errors found in the literature [22, 34, 42]. Using similar methods of registering the bead centroids measured with CT and biplanar radiography, Martin *et al.* [22] reported bead registration errors of 0.130-0.700mm for radio-opaque beads inserted into the proximal femur and acetabulum of two cadaver hip specimens, Tashman *et al.* [34] reported a mean bead registration error of 0.320mm for beads inserted into the femur of five canine subjects, and Anderst *et al.* [42] estimated the bead registration error to be one-half of the slice thickness of the CT image (0.313-0.625mm). The error in the present study is likely lower than in the literature because the beads were surrounded by polyethylene and not by dense soft tissue and bone. While error in registering the beads could create a misalignment of the joint surfaces relative to their true positions, the distances between the registered bead pairs represents a worst case scenario. It is possible that the errors in the beads could average out so that the joint surface was in fact aligned correctly. An example of this is seen in Figure 29 below, in which the bead centroids measured from a CT image (x's) are registered to the bead centroids measured using biplanar radiography (circles). If the registration errors are higher for some beads than others then a misalignment of

the joint surfaces could occur (Figure 29a). However, if the CT beads are scaled larger or smaller than the biplanar radiography bead locations, then the errors average out and the joint surfaces are in fact aligned correctly (Figure 29b). In this case the distances between the registered bead pairs are no longer an accurate measure of the registration step. This theory was confirmed by finding a low overall error in measuring the locations of the joint surfaces (0.010±0.005mm), which inherently included the error in measuring bone displacement with radio-opaque beads and the error in registering joint surfaces to the bone location.

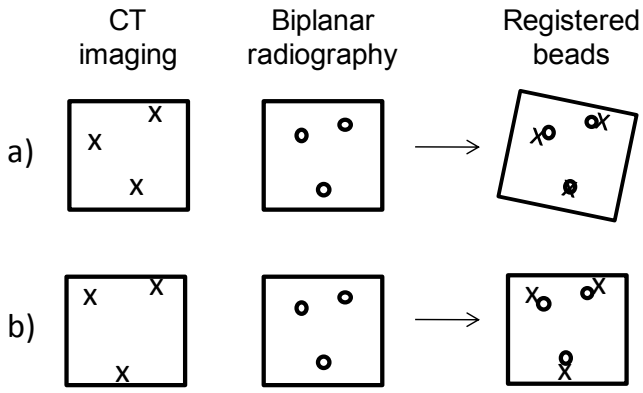

Figure 29. Examples of bead registration results, in which the beads measured from a CT image (x's) are registered to the beads measured with biplanar radiography (circles). (a) A higher registration error in some of the beads can lead to a misalignment of the joint surface. (b) If the CT beads are scaled larger than the biplanar radiography beads then the joint surfaces are aligned correctly and the registration error is inaccurate.

The results of the phantom accuracy study confirmed that error accumulates in each step of measuring the location of joint surfaces with biplanar radiography and CT imaging. A mean error was quantified for segmenting joint surfaces from a CT image (0.166±0.073mm), measuring bone displacement (0.002±0.004mm), and measuring the locations of joint surfaces (0.010±0.005mm). Together the error in segmenting joint surfaces from a CT image (0.166±0.073mm) and measuring the locations of joint surfaces in the biplanar radiography coordinate system (0.010±0.005mm) describe the accuracy of estimating cartilage thickness using biplanar radiography and CT imaging. The accumulation of errors is an important consideration for studies that are using this imaging technique to analyze the relative motion of bone surfaces and estimate cartilage deformation, since they often involve sub-millimeter movements. The error in measuring bone displacement using inserted radio-opaque beads is often reported in studies that use biplanar radiography and CT imaging to analyze joint surface motion [22, 33, 34, 42, 44]; however, this high accuracy level could be misleading in studies that

assess joint surface articulations. The error quantified for segmenting joint surfaces demonstrated the importance of high resolution CT images for maintaining the accuracy of this method.

The results of this study demonstrated that there is potential to estimate physiological hip cartilage deformation using biplanar radiography and CT imaging. This conclusion was made with an assumption that motion of the joint surfaces towards each other reflects a deformation of the cartilage. Greaves *et al.* applied a 230% bodyweight load to four hip joints *ex vivo*, and found an average hip cartilage deformation of 0.960±0.270mm (mean ± standard deviation) using qMRI [12]. In the present study the errors in estimating cartilage deformation were found to be 152±0.068mm for segmentation of the joint surfaces and 0.010±0.005mm for measuring the locations of joint surfaces, which combined are much lower than the *ex vivo* measured deformation of 0.960mm. There is also potential to further improve the segmentation error using a higher CT image resolution (such as using 0.3mm x 0.3mm x 0.3mm isotropic voxels).

A limitation of this study was the static image acquisition used during the experiments (ie. the phantoms were stationary during image collection). While this did not fully represent the dynamic image capture that our system is capable of, it was a sensible first step in the assessment of the biplanar radiography system and allowed our results to be compared to other groups in the literature. In addition, a dynamic accuracy experiment would have involved costly and complex equipment, such as a motorized precision linear stage with a digital read-out of its position that could be synced with the biplanar radiography image collection.

A second limitation was that soft tissues were not included in the phantom hip experiment. The *in vivo* hip joint is covered by layers of muscle and fatty tissue that could interfere with image quality and the detection of the locations of the radio-opaque beads. As found in previous work that used our system for single-plane radiography of the spinal cord [60], difficulty in viewing the beads through soft tissue can be relieved by increasing the voltage and current settings and using the de-noising algorithm described in Chapter 2, though both these methods may have an effect on the accuracy of the system. Image quality and the ability to detect radio-opaque beads inserted in the *ex vivo* hip were studied in the experiments described in Chapter 4.

3.5 Conclusions

Estimating cartilage thickness using biplanar radiography and CT imaging is a multi-device multi-step measurement protocol that has error associated with each step. From a preliminary assessment of our biplanar radiography system, its ability to measure the locations of radio-opaque beads was comparable to the most highly accurate biplanar radiography systems in the literature. To the author's knowledge no studies have reported the errors associated with the subsequent steps of estimating cartilage thickness. The present study quantified the mean error for segmenting joint surfaces (0.166±0.073mm), for measuring bone displacement (0.002±0.004mm), and for measuring the locations of joint surfaces (0.010±0.005m), which inherently assessed the error in registering the segmented joint surfaces to the bone locations. With the high accuracy of this imaging method, there may be potential to measure the locations of hip joint surfaces *ex vivo*, as well as estimate cartilage thickness and deformation across the joint.

Chapter 4. Estimating Cartilage Thickness and Cartilage Strain in the Hip Joint *Ex Vivo* with Biplanar Radiography and Computed Tomography

4.1 Introduction

As a first step towards understanding the connection between load-bearing and cartilage degeneration during osteoarthritis, biplanar radiography combined with computed tomography (CT) imaging has been identified as a method of measuring cartilage strain to indicate the load distribution, and has potential for *ex vivo* and *in vivo* studies. With an imaging system that proved capable of measuring the location of joint surfaces and estimating cartilage thickness in a phantom hip joint with high accuracy (see Chapter 3), there was potential to use this system to detect physiological cartilage deformation in the hip *ex vivo*. As summarized previously in Chapter 3, the steps involved for measuring cartilage thickness using biplanar radiography and CT imaging include the following:

1. Acquire a high-resolution CT scan of the joint from which the locations of the beads inserted in each bone and a 3D surface model of each bone can be segmented.
2. Measure the three-dimensional positions of the radio-opaque beads across all biplanar radiograph frames acquired during an applied load.
3. Register the CT bead centroids to their locations determined in Step 2, and apply the same registration to the 3D surface model of each bone. Repeat this for each frame during the applied load, allowing the location of the joint surfaces to be measured at each frame.
4. Estimate the cartilage thickness across the joint by measuring the minimum distance between the surfaces at every point. Complete these measurements for every frame to estimate changes in cartilage thickness during an applied load.

The distance between the joint surfaces provides an estimate of the cartilage thickness at each point on the surface, and it can be assumed that any compression of the joint surfaces towards one another causes cartilage deformation. At this time there is only one other known study that has measured the relative motion of hip joint surfaces using biplanar radiography, by Martin *et al*. [22], in which the point of closest contact in the anterosuperior region of the acetabulum was measured dynamically during passive flexion of the *ex vivo* hip. There are no known studies that

have measured cartilage deformation in the hip joint during a dynamic compressive load, which could provide considerable insight into physiological cartilage deformation.

While the errors involved in each of the steps outlined above were determined with a phantom study (see Chapter 3), there are challenges associated with an *ex vivo* experiment that need to be addressed to maintain the accuracy of the system. One challenge is securing the radio-opaque beads within each bone near the joint surface, so that the beads and bone act as a rigid body. A secure insertion within the bone is essential for the bead registration in Step 3, in which the CT bead centroids are registered to their location within the biplanar radiography frame, as any bead migration within the bone could increase the bead registration error and incorrectly position the joint surface. Bead insertion is commonly performed by drilling a small hole through the cortical bone near the joint surface, and using a needle to push a bead into the cancellous bone, which has been found to successfully hold the beads in place during joint motion [22, 34, 42, 65]. As described in Chapter 2, a rigid body motion error is commonly used to assess the relative motion of a bead within the bone. The relative distances between all the beads in a particular bone are calculated for each frame of data, and the standard deviation in the distances is defined as the error. The currently acceptable upper limit of the rigid body motion error in biplanar radiography studies is 0.350 mm, which was stated as an agreement of multiple research centers in order to standardize biplanar radiography practices [63]. To maintain the accuracy of our system to measure the distance between joint surfaces, a protocol for securely inserting radio-opaque beads in the bone needs to be established.

Another challenge of an *ex vivo* application is the reduced image contrast in the radiographs due to the presence of soft tissue around the joint. The thick layers of muscle and fat tissue cause interference by absorbing the penetrating x-rays, reducing the amount of radiation used to create the projected image. Adequate image contrast is essential to accurately measuring the proximity of joint surfaces, as it can influence both the ability to track radio-opaque beads inside the bone (Step 2) and to register the joint surfaces with the biplanar radiography data (Step 3). One method to obtain acceptable image contrast, without sacrificing accuracy, is to use a higher dose of radiation. Martin *et al.* [22] found that by applying three times the radiation dose, the beads in the hip joint of an obese patient could be tracked with equivalent accuracy to those in a non-obese patient, while still maintaining the dose under the regulated safety limits. As image

contrast varies between biplanar radiography setups, the effect of soft tissue on our system's ability to track radio-opaque beads needs to be evaluated *ex vivo*.

The purpose of this study was to verify that our imaging system was capable of measuring the location of *ex vivo* hip joint surfaces under a compressive load, which included three objectives:

1. Measure the displacement of the proximal femur and pelvis in the hip joint *ex vivo* during a dynamic compressive load with biplanar radiography, by measuring the locations of radio-opaque beads inserted in the bones.
2. Estimate the cartilage thickness and cartilage strain in the hip joint *ex vivo* during a dynamic compressive load using biplanar radiography and CT imaging.

4.2 Materials and methods

4.2.1 Specimen preparation

Two left cadaver hip specimens were used for this study, including the hemi-pelvis and proximal femur sectioned mid-shaft. Approval by the UBC Clinical Research Ethics Board was obtained for this project (number H08-01931). The donors were two females aged 59 and 80 at the time of death, with weights of 56kg and 78kg respectively. Neither specimen had any history of hip surgery. Specimens were procured immediately following the donor's death and stored at -19°C until testing was to be completed. Each specimen was thawed at room temperature one day prior to testing. Soft tissues were removed from the hemi-pelvis superior to the anterior superior iliac spine (ASIS), as well as from the femoral shaft inferior to the greater trochanter (Figure 30). All soft tissues around the hip joint and joint capsule were left intact. Specimens were kept moist at all times with a phosphate-buffered saline solution.

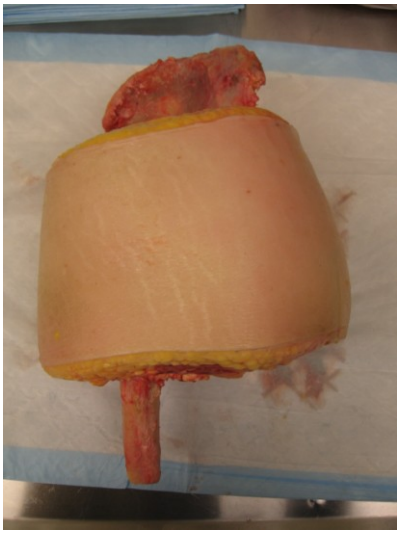

Figure 30. Posterior view of a left hip cadaver specimen with soft tissues removed superior to the ASIS on the pelvis and inferior to the greater trochanter on the femur.

4.2.2 **Bead injection**

Spherical radio-opaque tantalum beads (0.8mm-diameter, Tilly Medical, Lund, Sweden) were inserted into the bone segments, five beads in the pelvis and five beads in the proximal femur, with the beads distributed in the bone surrounding the acetabulum and in the region between the greater and lesser trochanters of the proximal femur. Bead locations were based on work by Lawrie *et al.* [65], which defined a bead placement protocol in the hip to that minimized bead overlap in biplanar radiographs. Biplanar radiography studies of the hip most commonly use 0.8mm-diameter beads, because while larger beads result in a larger image in the radiograph, their contour is more susceptible to distortion in the image which could result in a less accurate calculation of the bead centroid [64]. A pilot hole was drilled through the soft tissue and into the cortical bone with a custom drill bit (McMaster-Carr, Princeton, NJ) (Figure 31a). This created a 1.6mm hole in the bone that ended with a 0.8mm pocket for the bead. A brachytherapy needle (1.0mm-diameter, CP Medical, Portland, OR) was inserted into the drilled hole (Figure 31b), and used to push a tantalum bead into the small pocket in the bone. This process was repeated for each of the beads, and static x-rays were acquired to ensure successful insertion into the bone (Figure 32). If there was any doubt about whether a bead was successfully inserted, then an extra bead was injected into the bone at an alternate location as a precautionary measure.

(a)

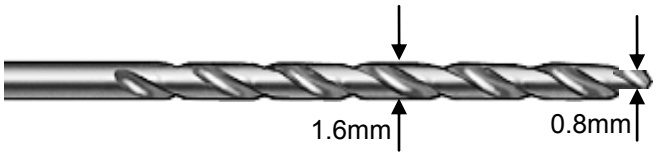

(b)

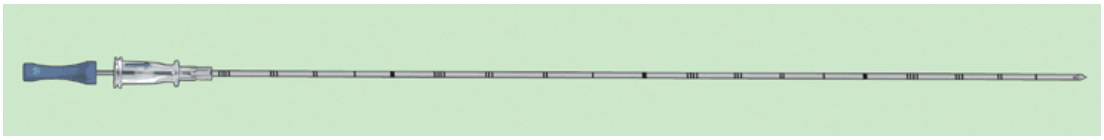

Figure 31. Beads were injected into the bone using a custom drill bit (a) and a brachytherapy needle (b). The drill bit was used to create a hole in the bone, and the needle was then inserted through the soft tissue into the hole and used to push a bead into the hole.

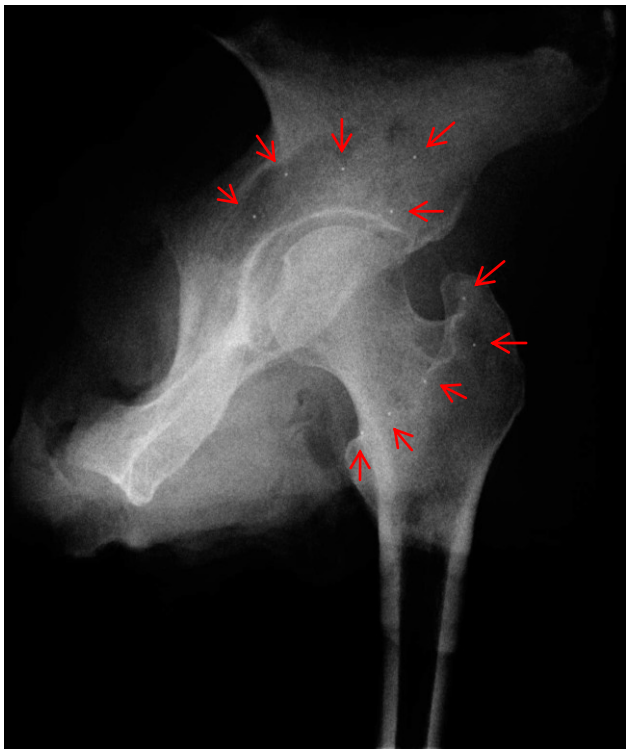

Figure 32. Static radiograph of a hip cadaver specimen with radio-opaque beads inserted in the proximal femur and acetabulum.

4.2.3 **CT imaging and joint surface segmentation**

High resolution computed tomography (CT) images (Toshiba Aquilion Helical CT, Canadian Diagnostics Center, Vancouver, Canada) were acquired of the unloaded hip specimen with the following image specifications: 0.5mm isotropic voxels, 0.5mm slice thickness, 512 x 512 field of view, 500s exposure time, 300A current. Analyze (Mayo Clinic, Rochester, MN) was used to locate the surfaces of the acetabulum and proximal femur relative to their respective beads. The

locations of the beads were determined by thresholding the CT images to isolate the voxels that made up each bead. For each set of voxels, corresponding to a single bead, their centroid was found based on a weighted grayscale. The surfaces of the hemi-pelvis and proximal femur were manually segmented in a slice-by-slice fashion, using a semi-automated region growing technique to identify the boundaries of the bone surfaces based on a user-defined pixel intensity threshold. Three-dimensional surface models of the hemi-pelvis and proximal femur were extracted using an adaptive deformation algorithm (Figure 33). Solid modeling software (Rapidform XOR, INUS Technology Inc., Seoul, South Korea) was used to manually reduce the surface models to include only the regions that acted as articular surfaces in the hip. For the hemi-pelvis this included the inner surface of the acetabular cup, and for the femur this included the surface of the femoral head, both of which were selected manually using anatomy diagrams of the articular surfaces as a reference [70].

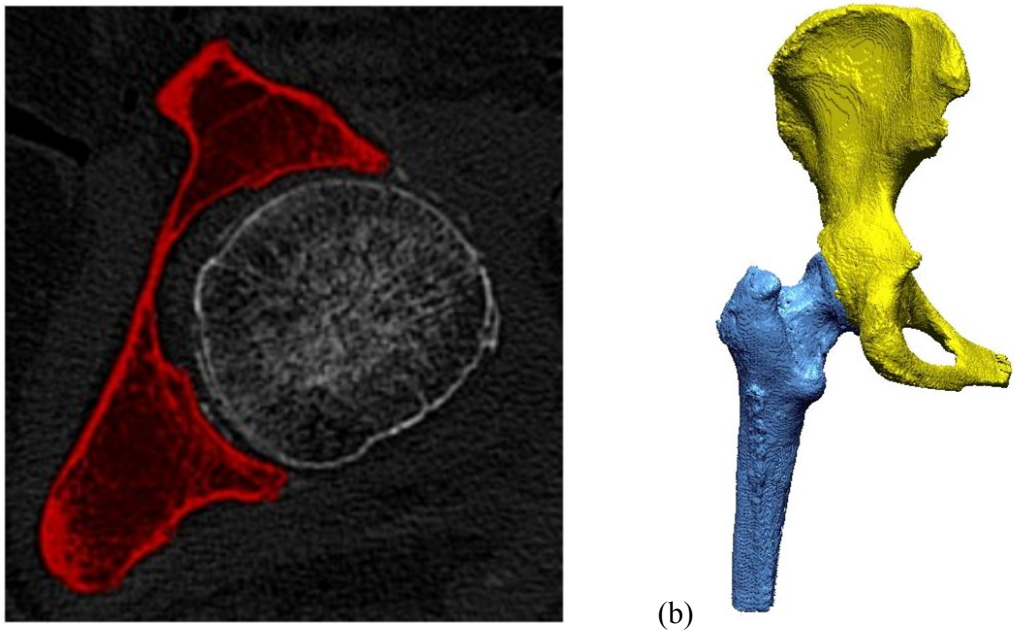

Figure 33. a) A CT slice of the hemi-pelvis bone (shown in red) and proximal femur (shown in white) in which the bone surfaces were segmented using Analyze software. b) 3D surface models of the hemi-pelvis (yellow) and proximal femur (blue) were extracted and imported into Rapidform software for analysis.

4.2.4 **Dynamic joint loading and biplanar radiography**

The femur and hemi-pelvis were potted in dental stone to allow correct alignment and attachment to the materials testing machine, using a previously designed alignment method in our laboratory [12]. The hemi-pelvis was aligned anatomically, with the anterior superior iliac

spine and pubic tubercle in the same coronal plane, so that its superior/inferior axis was aligned with the compression axis of the materials testing machine. The tilt of the hemi-pelvis was determined using a full cadaver pelvis as a visual reference. Using lasers, the femur was potted in a physiological alignment simulating two-legged stance, with the femoral shaft in 12° flexion and 5° valgus [71].

The potted specimen was positioned in a servo-hydraulic materials testing machine (Dynamite, Instron Corporation, Norwood, MA), such that the pelvic potting was attached to the actuator and the femoral potting was resting on the machine table (Figure 34). A load cell on the actuator monitored the applied force and had a maximum allowable load of 1000N. A ball bearing table was placed under the femoral potting to allow the joint to align itself during loading, so that the most congruent bone surfaces were pressed together, as occurs physiologically [72]. The ball bearing table allowed unconstrained translation in the medial/lateral and anterior/posterior directions, and unconstrained rotation around the superior/inferior axis, which prevented forces in the horizontal plane from influencing the axial joint loading direction.

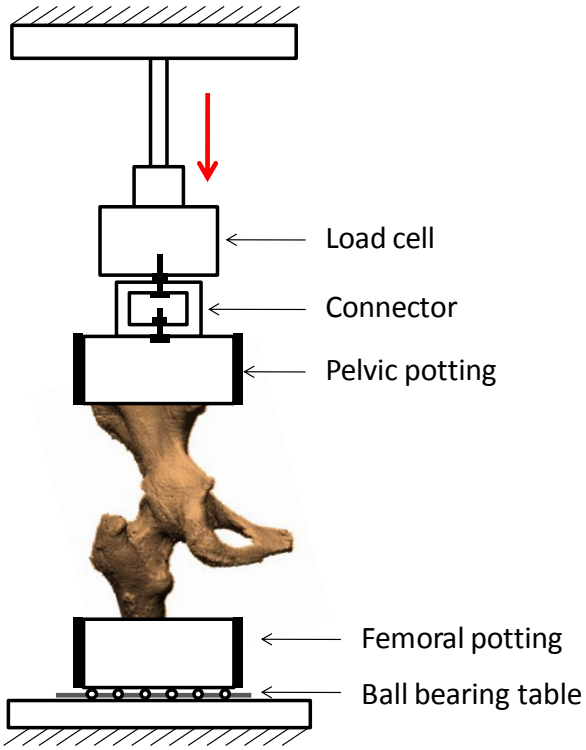

Figure 34. Hip cadaver setup in the servo-hydraulic testing machine. The pelvic potting was secured to the actuator and the femoral potting rested on a ball bearing table that allowed horizontal alignment during loading.

The biplanar radiography system was set up around the materials testing machine so that the articular surfaces and injected beads were within the capture volume. To investigate the effects of biplanar radiography equipment positioning, the x-ray tube and image intensifier pairs were positioned at a relative angle of 30º for the first specimen and 120° for the second specimen. As described in Chapter 2, the biplanar radiography system was calibrated for each test session by acquiring biplanar radiographs of a custom calibration object and computing the position and orientation of each camera in TEMA 3D (Image Systems, Wayne, NJ). A mean calibration error was found across the two test sessions. Loading of the specimens was controlled by a custom load-control program in Wavemaker (Instron Corporation, Norwood, MA). An axial load was applied to each specimen that increased from 0 N to the bodyweight (BW) of each specimen (560 N and 780 N, respectively) at a rate of 10 N/second, representing a slow weight distribution from a free leg up to two-legged stance [21]. Biplanar radiographs were acquired dynamically at 24 fps throughout the loading protocol at 160kV and 2.0mA. Higher voltage and current were required than in the accuracy studies described in Chapter 3 due to the density of soft tissue on the hip specimens. As described in Chapter 2, the biplanar radiographs were corrected for distortion, and a de-noising algorithm was applied to the radiographs to allow the beads to be identified more clearly.

4.2.5 **Measuring bone displacement**

As described in Chapter 2, the three-dimensional motion of the beads in the hemi-pelvis and proximal femur was tracked in TEMA 3D (Image Systems, Wayne, NJ). The output of the software was the three-dimensional coordinates of the beads in the biplanar radiography coordinate system for each frame during the applied loading. The centroid of the group of beads in each of the proximal femur and hemi-pelvis was calculated to analyze the displacement of the bones in each of the three orthogonal directions. The biplanar radiography coordinate frame was aligned with the anatomical coordinate system of the hip using bony landmarks in the CT image. The vertical axis of the biplanar radiography coordinate frame was already aligned with the superior axis of the joint during testing. The lateral and anterior directions were aligned by determining the location of the radio-opaque beads in the CT image when the ASIS and pubic tubercle were aligned in the coronal plane. A mean rigid body motion error (see Chapter 2) was

calculated for the beads in each bone to confirm that there was no relative motion within the bone.

4.2.6 **Measuring the relative locations of joint surfaces**

The locations of the beads measured in the CT coordinate system were registered with their corresponding locations in the biplanar radiography coordinate system using a least-squares based registration algorithm [66] in MATLAB (The MathWorks, Natick, MA, USA) that minimized the distance between each pair of registered beads (see Chapter 3 for a more detailed description). The registration process was completed separately for the beads in the hemi-pelvis and those in the proximal femur, to determine the location of each bone. The transformation matrix used to register the beads was then applied to the extracted surfaces of the acetabulum and femoral head. This allowed the location of each joint surface to be determined in the biplanar radiography coordinate system at every frame. The output of the registration algorithm was the distance between each pair of registered beads, otherwise defined as the distance between each bead in the biplanar radiography coordinate system and its corresponding registered bead from the CT coordinate system. The mean distance between each of the registered bead pairs across all image frames was calculated for comparison with the phantom accuracy study in Chapter 3. However as concluded previously, this registration error does not reflect an error in the location or orientation of the joint surfaces, or in the overall cartilage thickness measurements.

4.2.7 **Estimating cartilage thickness and strain**

To estimate the cartilage thickness across the joint surface, the distance between the joint surfaces was measured from each point on the acetabular surface to the closest point on the femoral head surface. The acetabulum was chosen as the reference from which to measure the distance because during the compressive load the femoral head became more contained within the acetabulum, and therefore the articular region of the femoral head varied during the applied load. This was completed for each frame to estimate the change in cartilage thickness for each point on the surface throughout the applied load. To highlight regional variation in the cartilage thickness, the femoral head was separated into five anatomical regions: superior, medial, posterior, lateral, and anterior [67] (Figure 23). The mean distance between the acetabulum and

femoral head was calculated for each region of interest to quantify the average cartilage thickness in each region throughout the applied load.

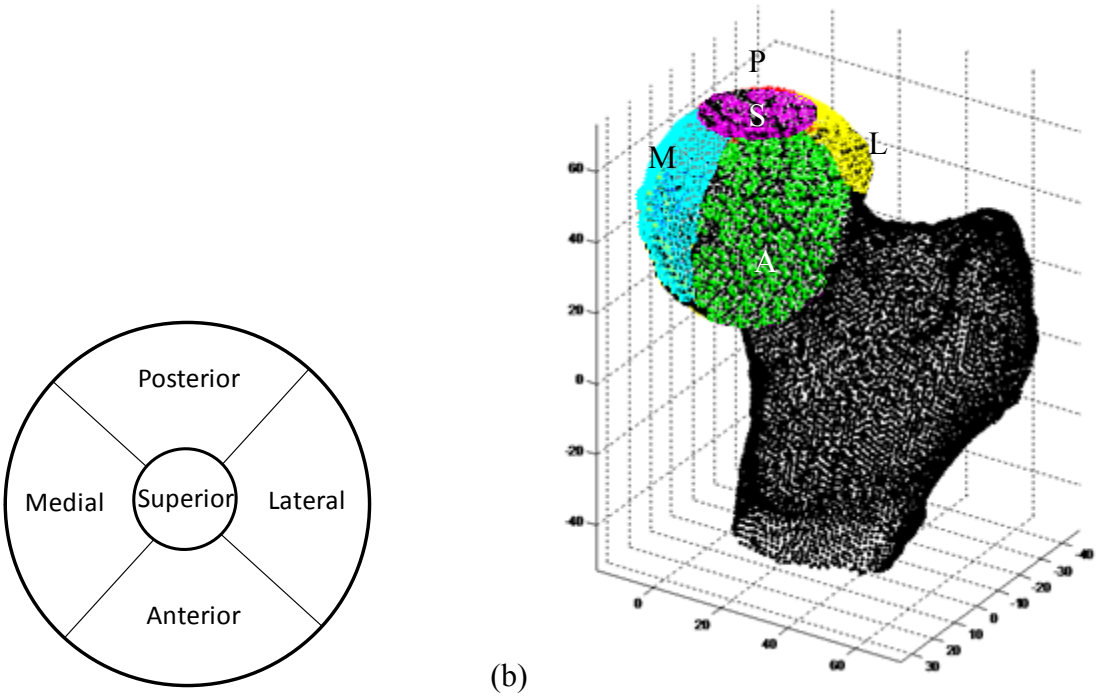

(a) (b)

Figure 35. Regions of interest (ROIs) were defined on the femoral head. (a) shows a superior view of the ROIs, (b) shows a 3D representation of the ROIs (colour-coded to show the regions only).

To analyze deformation of the cartilage throughout the applied load, engineering strain was calculated at each point on the joint surface for every frame. The original cartilage thickness was defined as the distance between the joint surfaces at their initial unloaded position, at which the hip specimens were under 0% bodyweight load. Cartilage strain was calculated at each point on the joint surface by subtracting the loaded cartilage thickness from the original cartilage thickness, and this value was then divided by the original cartilage thickness (Equation 2). A mean cartilage strain was calculated at each frame of the applied loading for the overall joint surface, as well as for each region of interest.

$$\text{Cartilage strain} = \frac{(\text{Cartilage thickness under load}) - (\text{Original cartilage thickness})}{(\text{Original cartilage thickness})} \times 100\%$$

Equation 2. Engineering strain of the cartilage was calculated at each point on the joint surface for each frame of the applied loading. The original cartilage thickness was measured with the joint under 0% bodyweight load.

4.3 Results

4.3.1 Biplanar radiography imaging

The three-dimensional calibration of the two camera views was completed as described in Chapter 2 for both cadaver specimens, and had a mean calibration error of 0.186 ±0.018 mm. Most of the radio-opaque beads were identifiable in the biplanar radiographs (Figure 36); however, in one specimen only four beads in proximal femur were included in the analysis (shown with arrows) because one bead was not visible in all image frames. The mean rigid body error was 0.050 mm in the acetabular beads and 0.077 mm in the femoral beads.

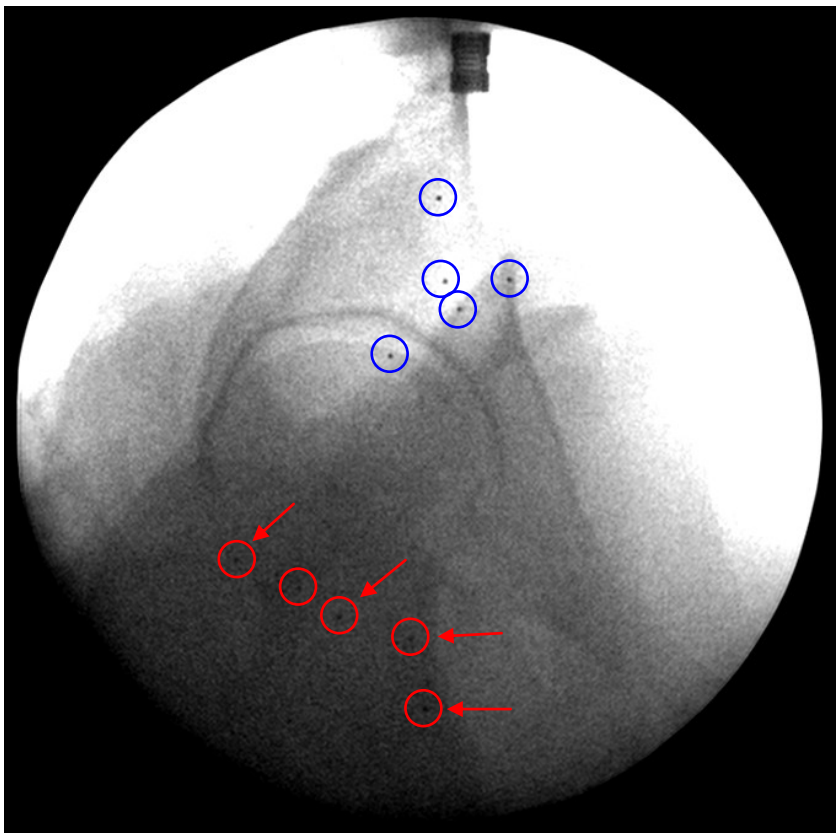

Figure 36. One of the radiographs of hip specimen 1 (56kg BW), showing the radio-opaque beads inserted into the hemi-pelvis (circled in blue) and proximal femur (circled in red). The beads indicated with arrows were used in the analysis of the proximal femur, as one bead was not visible in all image frames.

4.3.2 **Bone displacement**

The displacements of the proximal femur and hemi-pelvis were measured using the centroid of the group of beads in each bone, with translation seen predominantly in the posterior direction, followed by the inferior direction. The largest difference between the hemi-pelvis and proximal femur displacements was in the inferior direction, and was assumed to represent axial compression of the joint.

The proximal femur and hemi-pelvis followed similar paths of translation along the anterior/posterior (Figure 37a) and medial/lateral axes (Figure 37b). With the femur positioned on a ball-bearing table, the bones were unconstrained in the horizontal plane and allowed the beads to translate linearly in the posterior and medial directions during the compressive load. At 100% bodyweight load the difference between the hemi-pelvis and proximal femur displacements were 0.122mm and 0.181mm posteriorly (for specimen 1 and 2, respectively), and 0.017mm and 0.012mm laterally (for specimen 1 and 2, respectively), which likely represented horizontal compression of the cartilage.

The displacements of the proximal femur and hemi-pelvis differed most in the superior/inferior direction (Figure 37c). The femur was constrained vertically by the materials testing machine table and therefore showed less translation in the inferior direction than the hemi-pelvis, which was attached to the machine's actuator. The difference between their displacements in the inferior direction was assumed to represent axial compression of joint. At 100% bodyweight the difference between the hemi-pelvis and proximal femur displacements were 0.280mm and 0.310mm inferiorly (for specimen 1 and 2, respectively).

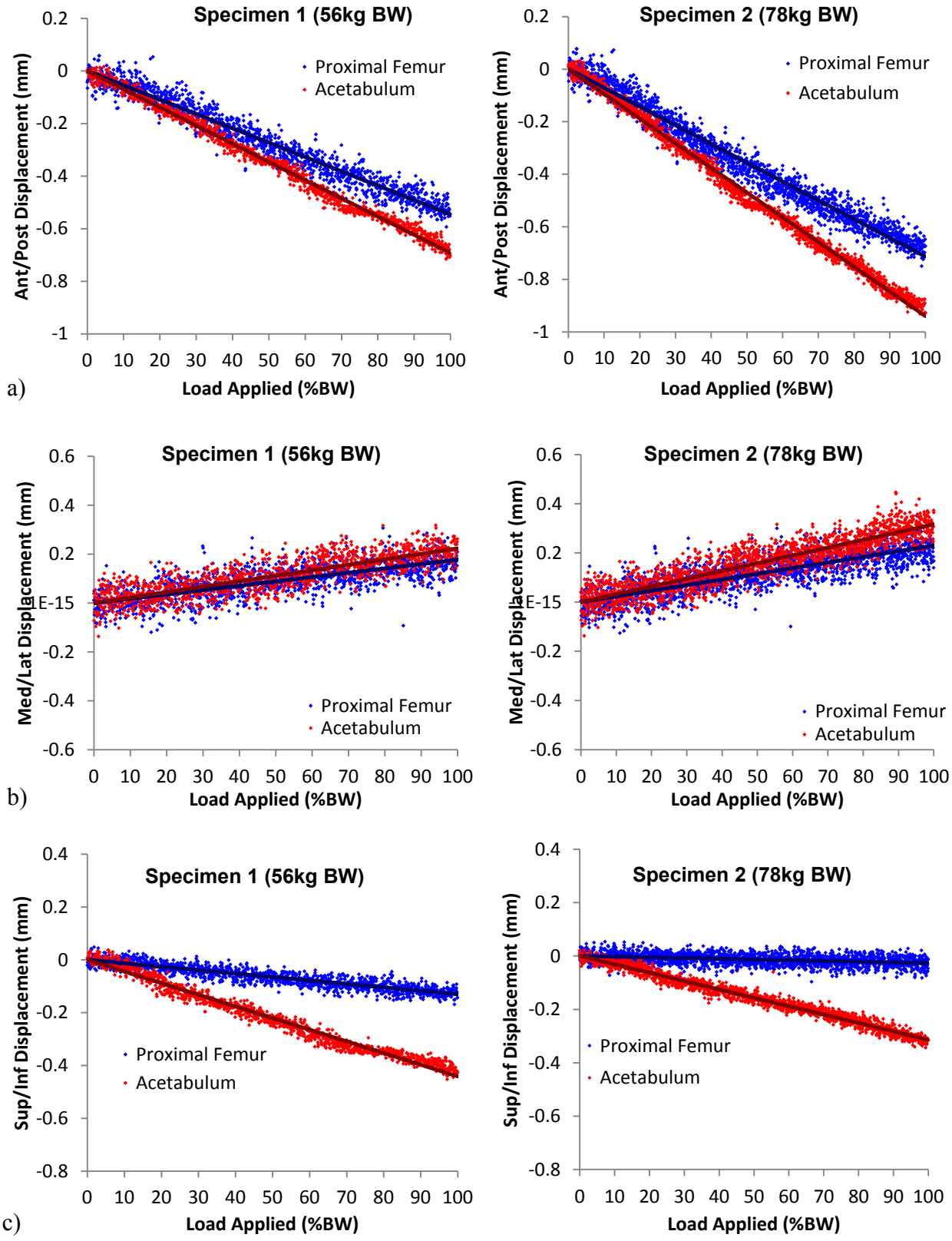

Figure 37. Applied load vs. displacement of the beads in the anterior/posterior (a), medial/lateral (b), and superior/inferior (c) directions for the two specimens. The motion of the beads inserted in each bone is shown for the proximal femur (blue) and hemi-pelvis (red), as well as a trend line for each.

4.3.3 **Locations of the joint surfaces**

The mean error in registering the bead centroids measured in the CT image to their locations measured using biplanar radiography was 0.185±0.009mm (mean ± standard deviation) for the beads in the acetabulum and 0.292±0.006mm for the beads in the proximal femur (Figure 38). These values were calculated as a mean registration error across all image frames of the dynamic loading.

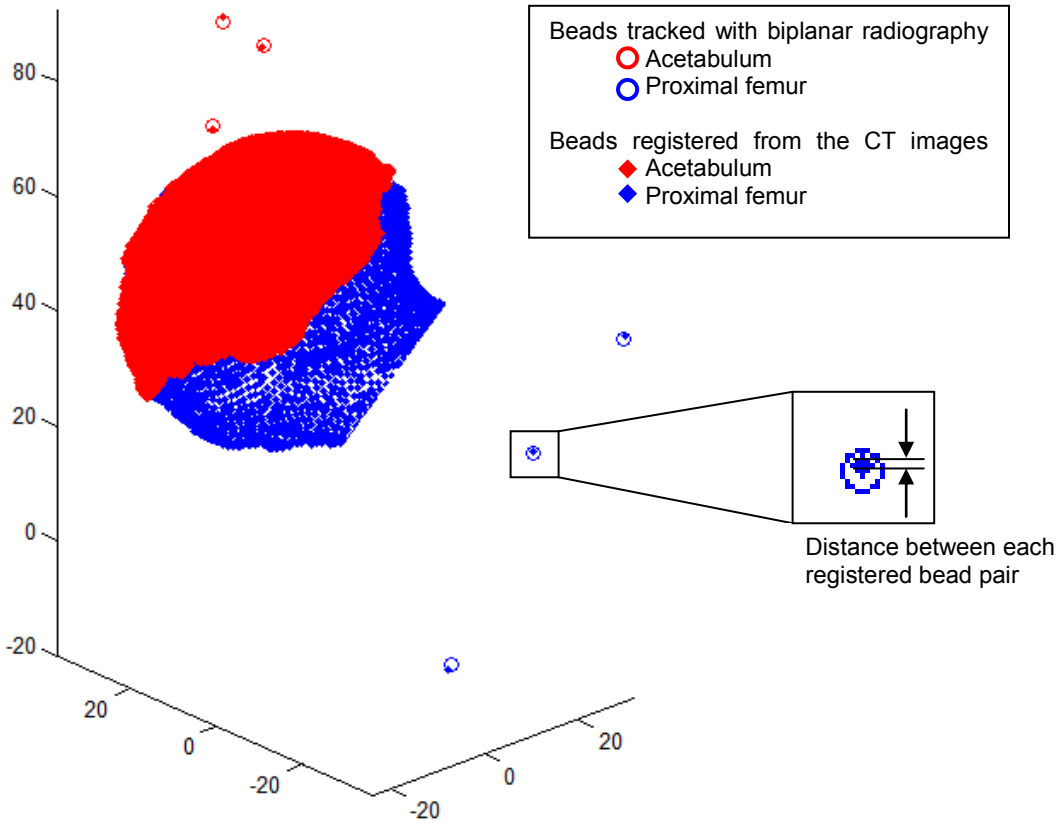

Figure 38. The biplanar radiography coordinate frame, showing the beads identified in the biplanar radiographs (circles) and the beads registered from the CT coordinate system (solid dots). The extracted surfaces of the femoral head (blue) and acetabulum (red) were also transformed into the biplanar radiography coordinate frame. The enlarged section demonstrates the three-dimensional distance between the biplanar radiography bead and its corresponding registered CT bead.

4.3.4 **Cartilage thickness and strain**

Specimen 1 had a mean unloaded cartilage thickness of 2.336±0.589mm (mean±standard deviation) and specimen 2 had a mean unloaded cartilage thickness of 2.738±1.170mm. The mean cartilage thickness decreased slightly for both specimens as the applied load was increased from 0% to 100% bodyweight, representing compression of the cartilage (Figure 39). A small

amount of cartilage deformation was detected in each specimen with a maximum mean deformation of 0.061mm and 0.170mm (for specimen 1 and 2, respectively), both of which occurred at 100% bodyweight load.

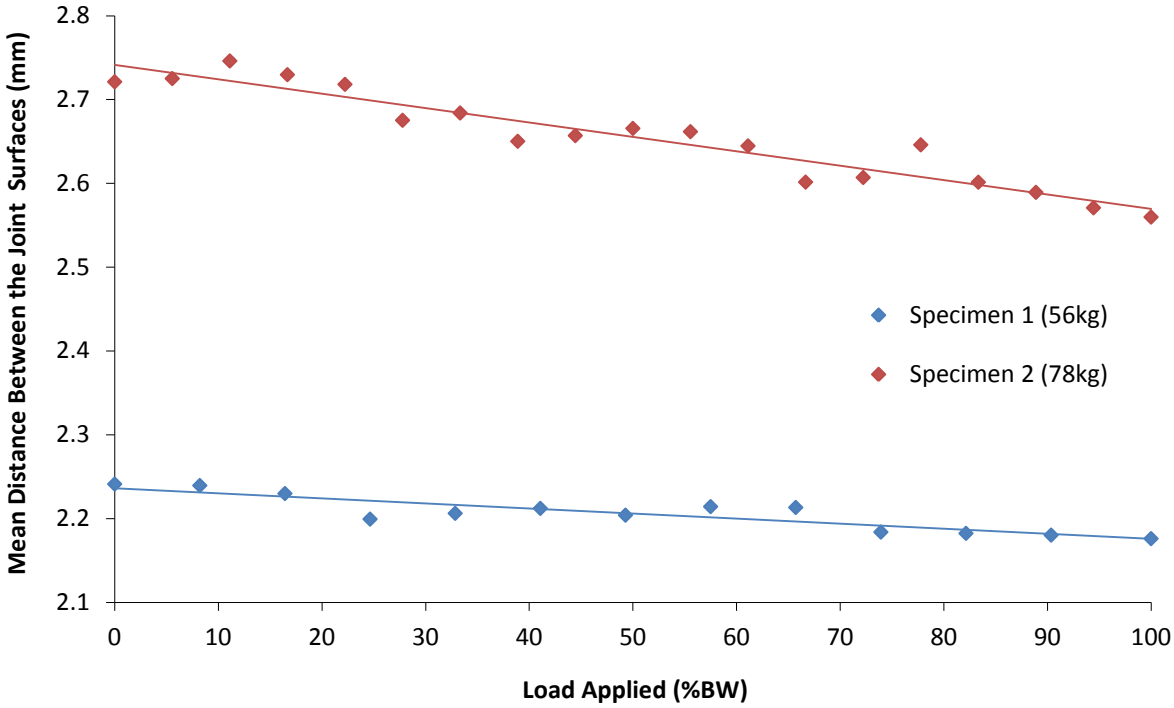

Figure 39. The mean distance between the femoral head and acetabular surfaces as the applied load was increased at 10N/s from 0 to 100% bodyweight of each specimen. For specimen 1 the duration of the loading period was 56s, and for specimen 2 the loading duration was 78s.

The unloaded cartilage thickness varied across the regions of the joint, with the highest cartilage thickness found in the posterior region and lowest found in the anterior region (Figure 40a-b). The largest mean cartilage deformation was found in the anterior region for specimen 1 and in the medial region for specimen 2. The mean cartilage deformation after the load was increased from 0%-100% bodyweight is summarized for each region of interest in Table 4 below, with the highest deformation found in the anterior region for specimen 1 and in the medial region for specimen 2.

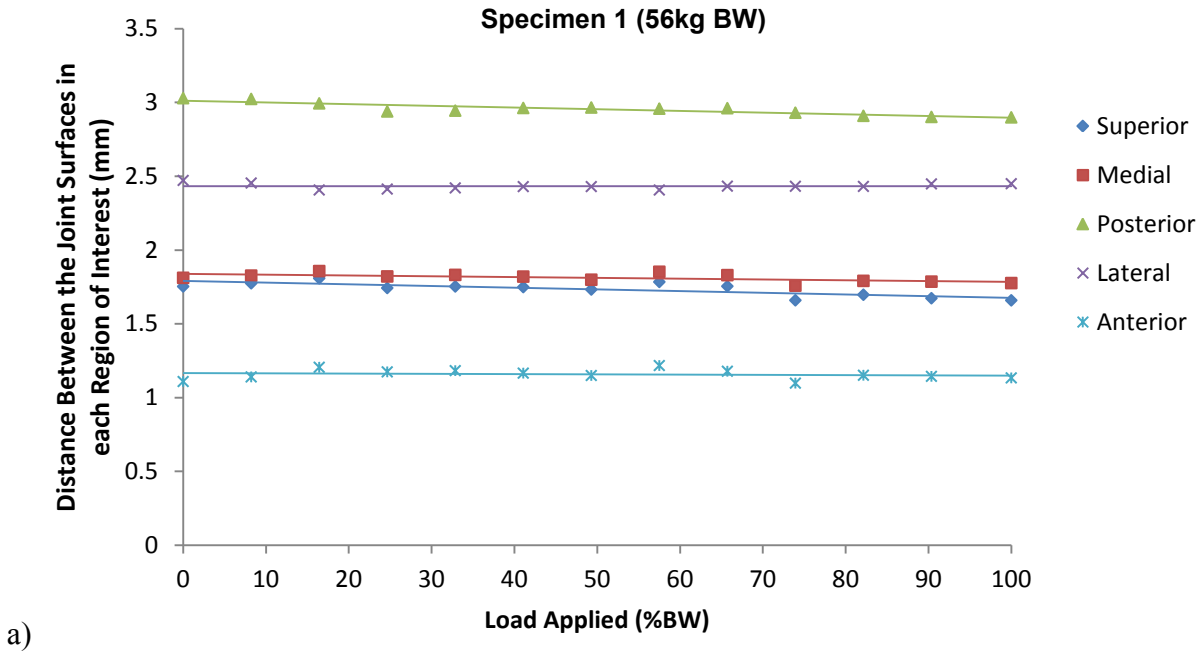

a)

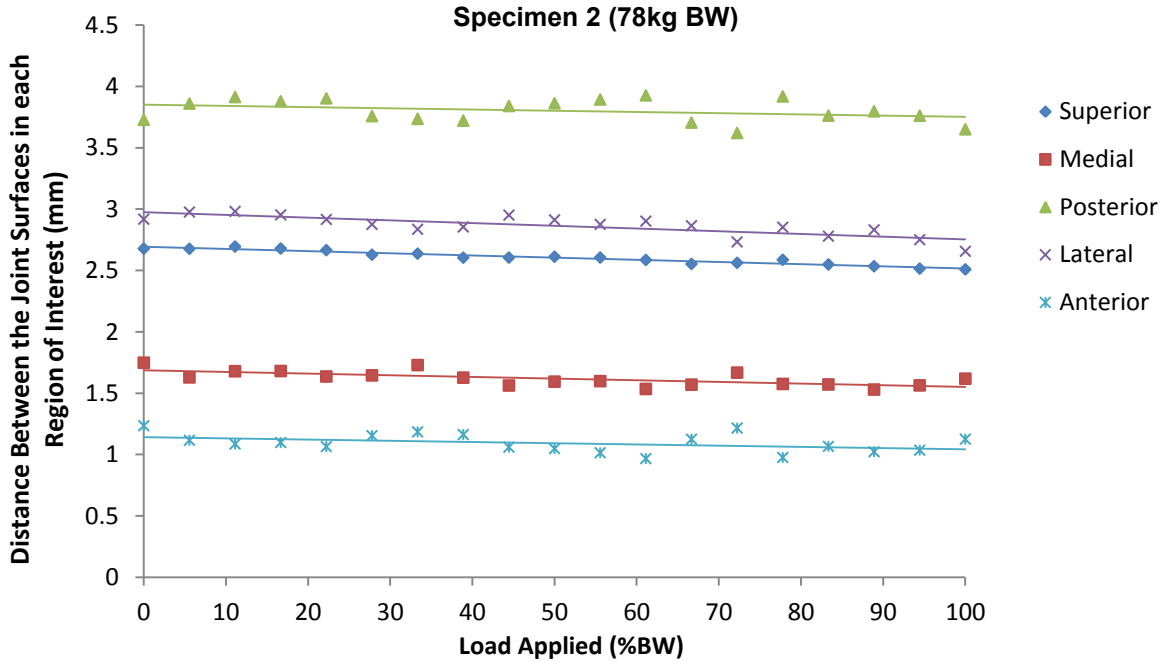

b)

Figure 40. The mean distance between the femoral head and acetabular surfaces in each region of interest (superior, medial, posterior, lateral, anterior) as the applied load was increased at 10N/s from 0 to 100% bodyweight for specimen 1 (a) and specimen 2 (b).

Table 4. Mean cartilage compression at 100% bodyweight load of the specimen. Compression was defined as a decrease in the distance between the femoral head and acetabular surfaces.

	Mean Cartilage Compression at 100% BW (mm)	
Region of Interest	**Specimen 1**	**Specimen 2**
Superior	0.110	0.100
Medial	0.060	0.220
Posterior	0.060	0.180
Lateral	0.120	0.130
Anterior	0.200	0.100

The mean cartilage strain across the joint surface increased for both specimens as the load was applied (Figure 41). A mean strain of -4.5% and -8.3% (for specimens 1 and 2 respectively) was found at 100% bodyweight load, representing a compressive strain of the cartilage under load. The highest mean cartilage strain was found in the superior region for specimen 1 and anterior region for specimen 2 (Table 5). The overall increase in compressive strain with applied load can be seen visually in Figure 42, which shows a colourmap on the femoral head surface of specimen 2 as the applied load was increased to 100% bodyweight. The translations of the bones in the horizontal plane, as found in the bead-tracking results in Chapter 3, were evident in the colourmap as the regions of high strain (shown in red) translated posteriorly across the femoral head surface.

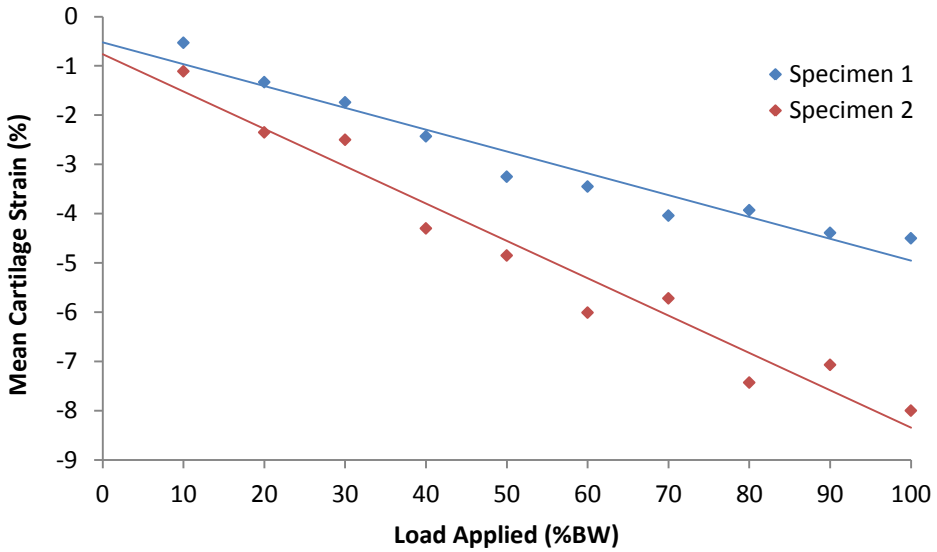

Figure 41. The mean cartilage strain increased for both specimens as the load was applied from 0 to 100% bodyweight, representing compression of the cartilage under load.

Table 5. Maximum cartilage strain as loading was increased from 0% to 100% bodyweight of each specimen (occurred at 100% bodyweight).

	Mean Cartilage Strain at 100% BW (%)	
Region of Interest	**Specimen 1**	**Specimen 2**
Superior	-7.0	-7.0
Medial	-4.0	-6.0
Posterior	-3.0	-4.0
Lateral	-0.3	-5.0
Anterior	-4.0	-9.0

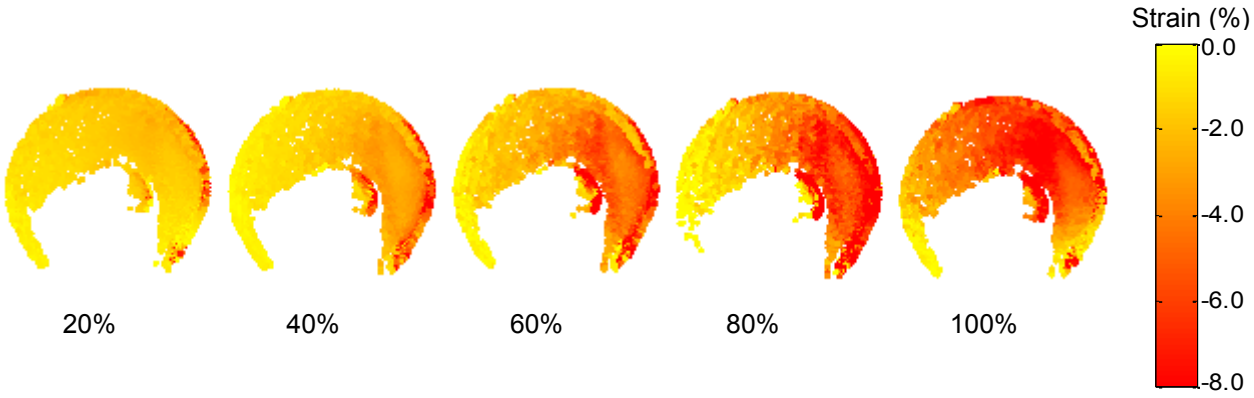

Figure 42. Cartilage strain colourmap on the femoral head surface of specimen 2 (78kg BW) at increased percentages of bodyweight load. The femoral head is displayed at a medial view, with the posterior region on the left and anterior region on the right.

4.4 Discussion

Due to the soft tissue surrounding the *ex vivo* hip joint there was poor image contrast in the biplanar radiographs, which influenced both the voltage setting used and the ability to identify radio-opaque beads in the images. To penetrate the soft tissue around the hip and optimize the image contrast, higher radiation settings (160kV, 2.0mA) were required compared to the phantom accuracy study described in Chapter 3 (100kv, 1.0mA). However, the settings used for the *ex vivo* study were comparable to standard clinical CT scans of the hip [73] and therefore did not pose a concern for increased radiation in future *in vivo* studies. The effect of increased soft tissue around the joint can be especially seen relative to a pilot *ex vivo* hip specimen used in this study, in which all the soft tissue was removed (Figure 43). Without soft tissue to interfere with the penetration of x-rays through the joint, the beads and bone surfaces were much more clearly identified in the radiographs.

(a)  (b) 

Figure 43. Image quality was much higher in (a) a pilot hip specimen with all soft tissue removed, relative to (b) a hip specimen with all soft tissue left intact.

The relative angle between the x-ray source and image intensifier pairs influenced the image contrast in the biplanar radiographs acquired, with a wide-angle orientation creating for better image contrast. Two configurations of the biplanar radiography equipment were used in this study, with the x-ray source and image intensifier pairs positioned at a relative angle of 30° for the first specimen and 120° for the second specimen. Due to the size of the base surrounding each piece of radiography equipment, there were physical restrictions to how the equipment could be positioned around the materials testing machine. The original angle of 30° was chosen because it allowed the specimen to be placed closer to the image intensifiers and therefore created a larger capture volume. However, the scatter of radiation from each x-ray source caused a highly contrasted area on the neighboring radiograph (Figure 44a). This issue was greatly improved by positioning the x-ray sources at a relative angle of 120° for the second specimen (Figure 44b). A wide-angle orientation of the biplanar radiography system is suggested for future studies to optimize image contrast around the joint.

(a)  (b) 

Figure 44. Radiographs acquired with the biplanar radiography system oriented in a (a) 30° configuration and (b) 120° configuration. Particularly in the 30° configuration, scatter from the neighboring x-ray source created areas of white space in the image, which reduced the image contrast around the joint. The image contrast was improved using a 120° configuration.

Segmentation of the *ex vivo* hip joint surfaces could have created a higher error than segmenting the smooth spherical shapes used in the phantom accuracy study in Chapter 3; however, with the high-resolution CT images acquired of the *ex vivo* hip specimens, the boundaries of the joint surfaces were clearly identified. The segmentation technique used in this study, in which an intensity threshold was used to identify bone surfaces in a CT image, has been validated in the literature. Segmented surface models of five ovine femur bones, with soft tissues left intact, were compared to their corresponding digitized surfaces, which were measured using a CMM, and the error of the segmentation technique was found to be 0.180±0.020mm [68]. This value is on the same order of magnitude as the segmentation errors calculated in the phantom study in Chapter 3 (0.166±0.073mm and 0.138±0.063mm, for the phantom proximal femur and acetabulum respectively), and suggests that the segmentation error would not have increased considerably in this *ex vivo* study.

The error in registering the joint surfaces with the measured bead locations (0.185±0.009mm and 0.292±0.006mm, for the proximal femur and acetabulum respectively) was comparable to the registration error found in the phantom accuracy study in Chapter 3 (0.185±0.004mm and 0.157±0.003mm, for the phantom proximal femur and acetabulum respectively). The slight increase in error is likely due to poor image contrast in the radiographs, caused by the density of

soft tissue around the joint. Use of the de-noising algorithm could also have created an error in measuring the location of the bead centroids in the biplanar radiographs. In this study a higher registration error was found for the femoral beads compared to the acetabular beads, which was likely due to the poor image contrast in the lower portion of the radiographs where the soft tissue was more densely situated.

The unloaded cartilage thickness measurements (2.336±0.589mm and 2.738±1.170mm, for specimens 1 and 2 respectively) were comparable to the literature [8-10]. However, the mean cartilage deformation as the load was increased from 0% to 100% bodyweight (0.061mm and 0.170mm, for specimens 1 and 2 respectively) was lower than expected. In particular the mean deformation was less than the relative displacements of the bones (based on their corresponding beads). This was likely due to rotation of the acetabulum around the femoral head, rather than direct compression of the surfaces towards each other, which can be seen visually in Figure 42 as the higher region of strain translated posteriorly across the femoral head surface. While the amount of deformation was not comparable to studies in the literature, the highest cartilage strain was identified in the anterior and superior regions (for specimens 1 and 2, respectively), which is consistent with findings that the anterosuperior region of the hip joint is the highest load-bearing region [10, 14, 20-22].

A challenge of dynamic biplanar radiography is accurately measuring the locations of the radio-opaque beads through the image noise. This was evident in the mean cartilage deformation plot (Figure 39), in which the values deviated from the trend line by up to 0.022mm and 0.037mm (for specimens 1 and 2 respectively). These values are consistent with the image noise measured in Chapter 3 (0.034±0.023mm), in which the mean position of a stationary bead was determined over 50 biplanar radiographs. However, in this *ex vivo* study the uncertainty was relatively high compared to the overall cartilage deformation. Applying a higher load to the hip joint would have allowed the amount of noise to be seen over a greater amount of cartilage deformation and helped for interpreting the capabilities of our system. The applied load was limited in this study by the materials testing machine, which was a lightweight model and had a maximum load limit of 1000N. Bodyweight was chosen as a comparable value between the two specimens that was within this limit. The materials testing machine was chosen over other heavyweight models because it was portable, which allowed the biplanar radiography system to be positioned correctly around the testing object. A future study of measuring hip cartilage deformation under

a higher load, such as simulating one-legged stance or walking, is suggested for further understanding of the limitations due to image noise.

A limitation of this study was that only five beads were inserted in each bone, compared to the 8-9 beads that were attached to each phantom in the accuracy study (see Chapter 3), and only four of the proximal femur beads were identifiable in all biplanar radiograph frames, which may have increased the registration error. While three beads is the minimum required to track the three-dimensional motion of a rigid body, the segmented joint surfaces are more likely to be oriented correctly if more beads are involved in the registration process. Therefore in future studies it would be optimal to insert 6-8 beads in each bone.

A limitation of this imaging technique, which used biplanar radiography to track bone motion and computed tomography to identify the joint surfaces, is that the joint surfaces could not be segmented from the biplanar radiographs themselves and required the use of radio-opaque beads to register the CT joint surfaces to the tracked bone motion. While radio-opaque beads are most commonly used in biplanar radiography studies, some groups are exploring the use of marker-less systems, in which 3D models of the bones are positioned to create digital reconstructed radiographs that match the original images. While this type of marker-less system is appealing for *in vivo* studies, it relies heavily on the use of accurate registration algorithms to match the original and digitally reconstructed radiographs.

4.5 Conclusions

This was the first study to estimate cartilage deformation in the *ex vivo* hip joint continuously throughout a compressive load and using a minimally invasive technique. It was found that using a high voltage setting, a wide-angled orientation of the x-ray sources around the joint, and a de-noising algorithm on the radiographs allowed the locations of the radio-opaque beads to be identified more clearly. Cartilage deformation was detected in all regions of the hip joint, with the largest cartilage strain identified in the anterior and superior regions, which is consistent with the literature. However, due to image noise and the low load applied, the amount of cartilage deformation was not comparable to findings in the literature and future studies using higher loads are needed to further assess the capabilities of our system.

Chapter 5. Integrated Discussion

5.1 Motivation and findings

While the reasons behind the initiation and progression of hip osteoarthritis are unclear, the most widely accepted theory is that excessive or abnormal joint loading increases stress concentrations in the cartilage, leading to cartilage wear and degeneration [4-6]. The connection between load-bearing and cartilage degeneration needs to be validated experimentally; ideally using a non-invasive method that can analyze the load distribution across the joint during a physiological loading application. As a first step towards understanding the connection between load-bearing and cartilage degeneration, biplanar radiography combined with CT imaging has been identified as a method of measuring cartilage strain to indicate the load distribution, and has potential for *ex vivo* and *in vivo* studies. This study analyzed the errors that accumulate during the multiple steps of measuring hip cartilage thickness using biplanar radiography and CT imaging. More specifically, the error was determined for segmenting joint surfaces from a CT image, measuring the three-dimensional location of bones using inserted radio-opaque baeds, and for measuring the locations of segmented joint surfaces in the biplanar radiography coordinate system throughout the applied loading. The major contributions of this study included the following:

- The capabilities of our biplanar radiography system were compared to other systems in the literature by determining the bead measurement accuracy (0.012±0.008mm), or the ability to measure the three-dimensional locations of radio-opaque beads during motion, which was found to be low relative to other systems in the literature (0.018-0.075mm) [54-57].
- The effect of using different orientations (30°, 90°, and 120°) of the biplanar radiography equipment around the hip joint was analyzed for its effect on image contrast in the radiographs. A wider-angled orientation was found to create the highest image contrast in the radiographs for identifying radio-opaque beads.
- The errors associated with measuring cartilage thickness using biplanar radiography and CT imaging were determined using a phantom hip joint, including the error for segmenting joint surfaces (0.166±0.073mm), and the overall error in measuring the locations of segmented joint surfaces in the biplanar radiography coordinate system (0.010±0.005mm). The combination of these errors represented the accuracy to which hip

cartilage thickness can be measured using our biplanar radiography system combined with CT imaging. This was the first study to report an error analysis of this multi-step multi-device method of measuring cartilage thickness.

- Cartilage strain was measured in the *ex vivo* hip during a continuous compressive load, which was a novel application in the hip joint. The highest cartilage strain was identified across the anterior and superior regions of the hip joint.

5.2 Utility for estimating hip cartilage strain *ex vivo* and *in vivo*

Biplanar radiography combined with CT imaging has been identified as a minimally invasive method of estimating hip cartilage strain, and can be extended to *ex vivo* and *in vivo* studies. It allows cartilage strain to be continuously measured across the joint during an applied load, from which the loading distribution can be inferred. The method is minimally invasive because the radio-opaque beads can be inserted in the bone outside the joint capsule, allowing the biological environment around the joint to remain intact. In *ex vivo* studies the beads can be inserted in the laboratory, while for *in vivo* studies the beads can be inserted during previously scheduled surgeries of volunteer subjects.

This imaging technique could be used to quantify hip cartilage strain during a variety of loading applications or simulated activities. For instance, as a pilot study, a static 140% bodyweight load was applied to one of the hip specimens (specimen 1) for ten minutes. Cartilage thickness decreased in all regions of the hip joint during the static load (Figure 45), up to a maximum of 0.067mm in the superior region. These results demonstrated the potential for using this technique to quantify creep in the cartilage, and could be used in the future to estimate changes in cartilage strain during higher loads and longer loading periods.

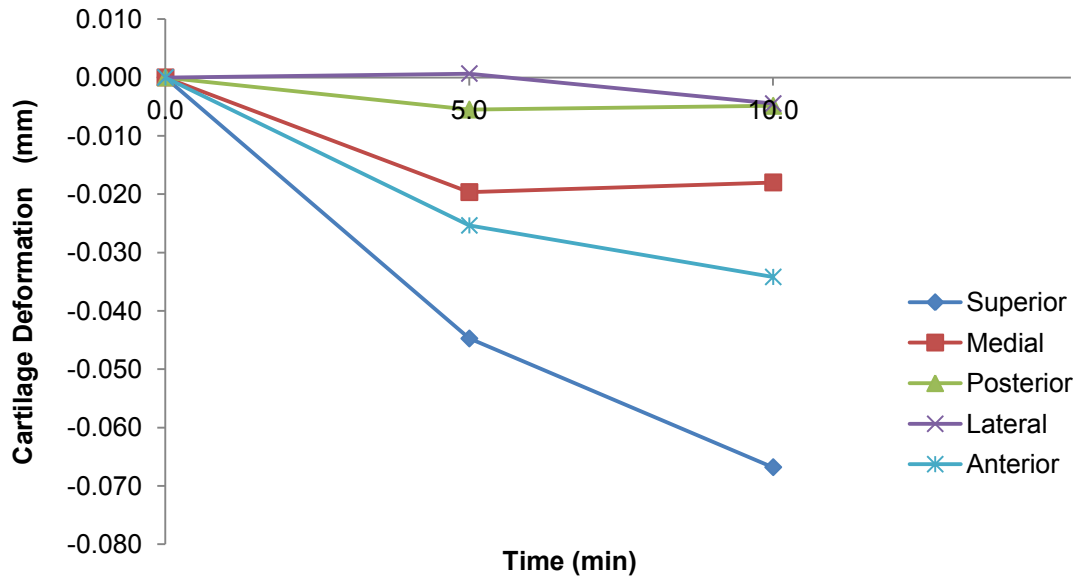

Figure 45. Cartilage deformation in each region of interest during a static 140% bodyweight load applied for ten minutes to *ex vivo* hip specimen 1.

As a second pilot study, a cyclic load was applied to a hip specimen (specimen 1) at an amplitude of 10-140% bodyweight load, for 12 cycles at 0.5Hz. The cyclic loading rate represented a slow bodyweight shift. The cartilage deformation results for the cyclic load were not clear. Figure 46 shows the mean displacement of the femoral head and acetabular surfaces over time. The difference between the peak displacements of the surfaces during each cycle likely represented cartilage compression; however, the high image noise made the results unreliable. The femoral head data was especially noisy as a result of poor contrast in the region around the femoral head in the radiographic images, which was due to more densely situated soft tissue. The mean difference between the peak displacements of the femoral head and acetabular surfaces was 0.035mm across all cycles. These were preliminary results of cyclic loading in the hip, and using higher loads over longer periods of time would more clearly identify trends in cartilage deformation during cyclic loading. Overall it is promising that these applications can be quantified using a biplanar radiography and CT imaging technique.

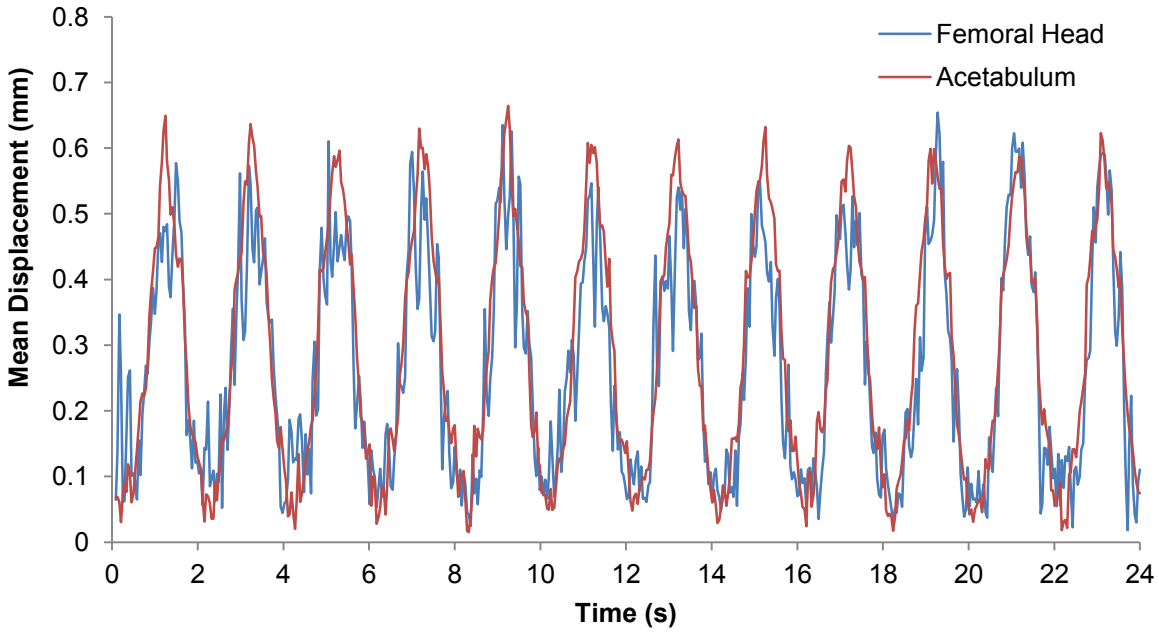

Figure 46. Mean displacement of the centroid of the femoral head and acetabular surfaces during a cyclic load applied to *ex vivo* hip specimen 1 at 10-140% BW amplitude, 12 cycles, 0.5Hz.

Further applications of this imaging technique include estimating cartilage strain in osteoarthritic and normal hip joints to indicate differences in the loading distribution between diseased and non-diseased joints. Measurements of this type would be useful for experimentally validating a connection between hip loading and cartilage degeneration during hip osteoarthritis. Finally, this method could also be used to study changes in hip biomechanics *in vivo* during a variety of joint diseases, including femoroacetabular impingement (FAI), Legg-Calve-Perthes disease, or hip dysplasia.

5.2.1 **Strengths**

A phantom accuracy study demonstrated that biplanar radiography combined with CT imaging is accurate enough to detect clinically relevant changes in cartilage thickness during loading. Cartilage deformation has been measured *ex vivo* using qMRI, a non-invasive method of measuring cartilage thickness during static loading, and deformation was found up to 0.960 mm under a 230% bodyweight load [12]. The errors in using biplanar radiography combined with CT imaging to measure cartilage deformation were found to be 0.166±0.073mm for segmentation of the joint surfaces and 0.010±0.005mm for measuring the locations of joint surfaces, which were

much lower than the deformation measured *ex vivo*. In the present study, a small amount of cartilage deformation was detected in the *ex vivo* hip, with areas of high cartilage strain identified in the anterior and superior regions, which was consistent with the literature. However, due to image noise and the low load applied, the actual amount of cartilage deformation was not comparable to findings in the literature. Future studies using higher loads to create larger cartilage deformation are needed to further assess the capabilities of the system for detecting physiological cartilage deformation.

As a minimally invasive technique, biplanar radiography combined with CT imaging allowed the joint capsule to remain intact and maintained the loading environment in the joint during testing. Invasive methods of measuring hip loading that involve destruction of the joint capsule, particularly pressure sensitive film, are susceptible to biological changes within the joint that could influence the load distribution measured.

As a continuous measure of cartilage strain across the joint surface, biplanar radiography combined with CT imaging allows changes in the load distribution to be detected throughout a loading application. This has considerable advantages over static measures of cartilage strain (qMRI, static radiography, pressure sensitive film), which can only measure cartilage strain during static loading or measure the peak loads experienced during a loading protocol.

5.2.2 **Limitations**

Using biplanar radiography combined with CT imaging does not allow a direct measurement of cartilage thickness or cartilage strain. Rather, thickness is estimated from images of the joint surfaces and strain is estimated from a change in the cartilage thickness during loading. Cartilage strain is also simplified by assuming that the cartilage is in pure compression during the applied load, which does not take into account friction between the femoral and acetabular cartilage layers that could lead to tensile or shear strain of the cartilage, particularly around the periphery of the femoral head. Despite these estimated values of cartilage thickness and strain, with the high resolution of CT images and measurement accuracy of biplanar radiography, this imaging technique has been validated for estimating physiological joint surface articulations in the knee [33-35, 42, 44-49], ankle [50, 51] and shoulder [52].

Camera placement is a limitation of this method, since it was found that positioning the biplanar radiography equipment in different orientations around the hip joint affected image contrast in the radiographs. Poorer image contrast may lower the accuracy of the system, as it could create error in measuring the location of the radio-opaque beads. Positioning the cameras at wider angles around the hip joint created radiographs with better image contrast for identifying the radio-opaque beads. Cameras should therefore be placed at wider angles; however, this may limit the joint loading apparatus that can be used because the large base supports on the x-ray sources and image intensifiers must fit around the apparatus.

Radiation exposure is a limitation of all imaging techniques that expose subjects to x-rays during *in vivo* studies, which for the method described in this study occurs during both the biplanar radiograph and CT image acquisition. However, the voltage, amperage, and exposure times used with our system were within the recommended dose limits for patients and workers stated by Health Canada [53], and has the potential to be used for *in vivo* studies in the future.

5.3 Future directions

A future step in measuring hip cartilage strain using biplanar radiography and CT imaging is the addition of unloaded cartilage models from MR images. By creating a 3D surface model of the articular cartilage in an unloaded hip joint from an MR image and registering the model to the locations of the bones, then overlap of the bone surfaces into the cartilage model during loading could be used to estimate cartilage deformation. An advantage of using MR cartilage models is that defects or thinner regions of cartilage, potentially due to osteoarthritis, could be identified. This would be particularly important if there were any regions in which the femoral and acetabular cartilage are not in contact, since it could influence the amount of cartilage deformation measured. This method has been used to measure cartilage contact mechanics in the knee [48, 49], shoulder [52], and ankle [50], but has yet to be applied to the hip joint. A limitation of this method is that high resolution MR images must be acquired to accurately segment the cartilage surfaces, and the unloaded cartilage model does not represent the cartilage thickness throughout the loading protocol.

To avoid the insertion of radio-opaque markers in the bone, marker-less biplanar radiography systems are currently being explored. These systems use CT surface models of the joint to create digitally reconstructed radiographs of the joint at each frame. The position and orientation of the surface models are adjusted until the digitally reconstructed radiographs match the original biplanar radiographs. This marker-less technique is very attractive for non-invasive *in vivo* studies, as bead insertion often discourages subjects from volunteering for studies and creates for small sample sizes. However, there is the inherent tradeoff that the technique relies heavily on high image resolution and complex image registration algorithms. The accuracy of marker-less systems is still being validated in the literature, using radio-opaque bead tracking as a reference standard, with accuracies ranging from 0.200-0.385mm [22, 36, 45] and precisions ranging from 0.200-0.700mm [22, 36, 45]. This is a considerable increase in error relative to bead-based methods, and currently has limited use for analyzing micro-motions such as cartilage deformation. A model-based method could be used with our system to perform a completely non-invasive *in vivo* study of the hip joint; however, this method needs to be developed further before it can be used to accurately quantify hip cartilage deformation.

5.4 Conclusion

Biplanar radiography combined with CT imaging has the potential to detect physiological hip cartilage deformation in *ex vivo* and *in vivo* applications. The errors associated with this method were assessed using a simple phantom, and it was found that cartilage thickness could be estimated in the phantom with high accuracy. The analysis was applied to the hip *ex vivo*; however, a low load was used and only a small amount of cartilage deformation was detected. Further studies using higher loads to compress the cartilage are needed to fully assess this method for detecting clinically relevant hip cartilage deformation. Overall biplanar radiography combined with CT imaging has the potential to estimate cartilage deformation in response to load, while using minimally invasive method that continuously provides information throughout an applied load.

References

1. Brandt, K.D., P. Dieppe, and E.L. Radin, *Etiopathogenesis of osteoarthritis.* Rheum Dis Clin North Am, 2008. **34**(3): p. 531-559.
2. Radin, E., et al., *Mechanical determinants of osteoarthritis.* Semin Arth Rheum, 1991. **21**(3 Suppl 2): p. 12-21.
3. Mankin, H., *The reaction of articular cartilage to injury and osteoarthritis (first of two parts).* N Engl J Med, 1974. **291**(24): p. 1285-1292.
4. Ateshian, G., et al., *Finite deformation biphasic material properties of bovine articular cartilage from confined compression experiments.* J Biomech, 1997. **30**(11-12): p. 1157-1164.
5. Gupta, S., et al., *The economic burden of disabling hip and knee osteoarthritis (OA) from the perspective of individuals living with this condition.* Rheumatology (Oxford), 2005. **44**(12): p. 1531-1537.
6. Kim, Y. and H. Azuma, *The nerve endings of the acetabular labrum.* Clin Orthop Relat Res, 1995. **320**: p. 176-181.
7. Drake, R., W. Vogl, and A. Mitchell, *Gray's Anatomy for Students, 2nd Edition*. 2009, Philadelphia, PA, USA: Elsevier Inc.
8. Adam, C., et al., *The distribution of cartilage thickness within the joints of the lower limb of elderly individuals.* J Anat, 1998. **193**: p. 203-214.
9. Shepherd, D. and B. Seedhom, *Thickness of human articular cartilage in joints of the lower limb.* Ann Rheum Dis, 1999. **58**(1): p. 27-34.
10. Naish, J., et al., *MR measurement of articular cartilage thickness distribution in the hip.* Osteoarthritis and Cartilage, 2006. **14**(10): p. 967-73.
11. Eckstein, F., et al., *Quantitative analysis of incongruity, contact areas and cartilage thickness in the human hip joint.* Acta Anat (Basel), 1997. **158**(3): p. 192-204.
12. Greaves, L., *M.A.Sc Thesis: Effect of Acetabular Labral Tears, Repair and Resection on Hip Cartilage Strains: A 7T MR Study*, in *Department of Mechanical Engineering*. 2009, University of British Columbia: Vancouver.
13. Armstrong, C., A. Bahrani, and D. Gardner, *In vitro measurement of articular cartilage deformations in the intact human hip joint under load.* J Bone Joint Surg Am, 1979. **61**: p. 744-755.
14. Afoke, N., P. Byers, and W. Hutton, *Contact pressures in the human hip joint.* J Bone Joint Surg, 1987. **69-B**(4): p. 536-541.
15. Macirowski, T., S. Tepic, and R. Mann, *Cartilage stresses in the human hip joint.* J Biomech Eng, 2008. **116**(1): p. 10-18.
16. Soltz, M. and G. Ateshian, *Experimental verification and theoretical prediction of cartilage interstitial fluid pressurization at an impermeable contact interface in confined compression.* J Biomech, 1998. **31**(10): p. 927-934.
17. Ferguson, S., et al., *An in vitro investigation of the acetabular labral seal in hip joint mechanics.* J Biomech, 2003. **36**: p. 171-178.
18. Tan, V., et al., *Contribution of acetabular labrum to articulating surface area and femoral head coverage in adult hip joints: an anatomic study in cadavera.* Am J Orthop, 2001. **30**(11): p. 809-812.
19. Lane, N.E., *Clinical practice. Osteoarthritis of the hip.* N Engl J Med, 2007. **357**: p. 1413-1421.

20. Sparks, D., et al., *Contact pressures in the flexed hip joint during lateral trochanteric loading.* J Ortho Res, 2005. **23**(2): p. 359-366.
21. Bergmann, G., G. Deuretzbacher, and M. Heller, *Hip contact forces and gait patterns from routine activities.* J Biomech, 2001. **34**(7): p. 859-871.
22. Martin, D., et al., *Model-based tracking of the hip: implications for novel analyses of hip pathology.* J Artho, 2010. **26**(1): p. 88-97.
23. Noguchi, Y., et al., *Cartilage and labrum degeneration in the dysplastic hip generally originates in the anterosuperior weight-bearing area: an arthroscopic observation.* Arthroscopy, 1999. **15**(5): p. 496-506.
24. Adams, D., G. Kempson, and S. Swanson, *Direct measurement of local pressures in the cadaveric human hip joint.* Med Biol Eng Comput, 1978. **16**: p. 113-115.
25. Hak, D., et al., *Consequences of transverse acetabular fracture malreduction on load transmission across the hip joint.* J Orthop Trauma, 1998. **12**: p. 90-100.
26. Bay, B.K., et al., *Statically equivalent load and support conditions produce different hip joint contact pressures and periacetabular strains.* J Biomech, 1997. **30**(2): p. 193-196.
27. Hale, J. and T. Brown, *Contact stress gradient detection limits of pressensor film.* J Biomech Eng, 1992. **114**(3): p. 352-357.
28. Athanasiou, K., et al., *Interspecies comparisons of in situ intrinsic mechanical properties of distal femoral cartilage.* J Ortho Res, 1991. **9**(3): p. 330-40.
29. Wu, J., W. Herzog, and M. Epstein, *Effects of inserting a pressensor film into articular joints on the actual contact mechanics.* J Biomech Eng, 1998. **120**: p. 655-659.
30. Brown , T. and D. Shaw, *In vitro contact stress distributions in the natural human hip.* J Biomech, 1983. **16**(6): p. 373-384.
31. Anderson, A., et al., *Effects of idealized joint geometry on finite element predictions of cartilage contact stresses in the hip.* J Biomech, 2010. **43**(7): p. 1351-1357.
32. Brinckmann, P., W. Frobin, and E. Hierholzer, *Stress on the articular surface of the hip joint in healthy adults and persons with idiopathic osteoarthritis of the hip joint.* J Biomech, 1981. **14**(3): p. 149-156.
33. Anderst, W., C. Les, and S. Tashman, *In vivo serial joint space measurements during dynamic loading in a canine model of osteoarthritis.* Osteoarthritis and Cartilage, 2005. **13**: p. 808-816.
34. Tashman, S., *In-vivo measurement of dynamic joint motion using high speed biplane radiography and CT: application to canine ACL deficiency.* J Biomech Eng, 2003. **125**: p. 238-245.
35. Anderst, W., R. Vaidya, and S. Tashman, *A technique to measure three-dimensional in vivo rotation of fused and adjacent lumbar vertebrae.* Spine Journal, 2008. **8**: p. 991-997.
36. Bey, M., et al., *Accuracy of biplane x-ray imaging combined with model-based tracking for measuring in-vivo patellofemoral joint motion.* J Ortho Surg Res, 2006. **3**(38): p. 1-8.
37. Luan, F., et al., *Qualitative analysis of neck kinematics during low-speed rear-end impact.* Clin Biomech, 2000. **15**: p. 649-657.
38. Saari, T., et al., *Knee kinematics in medial arthrosis. Dynamic radiostereometry during active extension and weight-bearing.* J Biomech, 2005. **38**: p. 285-292.
39. You, B.-M., et al., *In vivo measurement of 3-D skeletal kinematics from sequences of biplane radiographs: application to knee kinematics.* IEEE Trans Med Imag, 2001. **20**(6): p. 514-525.

40. Selvik, G., *Thesis: Roentgen stereophotogrammetry: a method for the study of the kinematics of the skeletal system*, in *Departments of Anatomy and Diagnostic Radiology*. 1974, University of Lund: Lund, Sweden. p. 56.
41. Spoor, C. and F. Veldpaus, *Rigid body motion calculated from spatial co-ordinates of markers.* J Biomech, 1980. **13**: p. 391-393.
42. Anderst, W. and S. Tashman, *A method to estimate in vivo dynamic articular surface interaction.* J Biomech, 2003. **36**: p. 1291-1299.
43. Kelkar, R., et al., *Glenohumeral mechanics: a study of articular geometry, contact, and kinematics.* J Shoulder Elbow Surg, 2001. **1**: p. 73-84.
44. Anderst, W. and S. Tashman, *The association between velocity of the center of closest proximity on subchondral bones and osteoarthritis progression.* J Ortho Res, 2009. **27**(1): p. 71-77.
45. Anderst, W.J., et al., *Validation of three-dimensional model-based tibio-femoral tracking during running.* Med Eng & Phys, 2009. **31**: p. 10-16.
46. Asano, T., et al., *In vivo three-dimensional knee kinematics using a biplanar image-matching technique.* Clin Orthop Relat Res, 2001. **388**: p. 157-166.
47. Komistek, R., D. Dennis, and M. Mahfouz, *In vivo fluoro-scopic analysis of the normal human knee.* Clin Orthop, 2003. **410**: p. 69-81.
48. Li, G., et al., *Anterior cruciate ligament deficiency alters the in vivo motion of the tibiofemoral cartilage contact points in both the anteroposterior and mediolateral directions.* J Bone Joint Surg Am, 2006. **88**(8): p. 1826-34.
49. DeFrate, L., et al., *In vivo tibiofemoral contact analysis using 3D MRI-based knee models.* J Biomech, 2004. **37**: p. 1499-1504.
50. Wan, L., et al., *Determination of in-vivo articular cartilage contact areas of human talocrural joint under weightbearing conditions.* Osteoarthritis and Cartilage, 2006. **14**: p. 1294-1301.
51. Corazza, F., et al., *Articular contact at the tibiotalar joint in passive flexion.* J Biomech, 2005. **38**: p. 1205-1212.
52. Boyer, P., et al., *In vivo articular cartilage contact at the glenohumeral joint: preliminary report.* J Orthop Sci, 2008. **13**: p. 359-365.
53. Maharaj, H., *Radiation protection and safety for industrial x-ray equipment. Safety Code 34*. 2003, Health Canada.
54. Kedgley, A., T. Birmingham, and T. Jenkyn, *Comparative accuracy of radiostereometric and optical tracking systems.* J Biomech, 2009. **42**: p. 1350-1354.
55. Madanat, R., et al., *Accuracy and precision of radiostereometric analysis in the measurement of three-dimensional micromotion in a fracture model of the distal radius.* J Ortho Res, 2005. **23**: p. 481-488.
56. Solomon, L., et al., *The accuracy and precision of radiostereometric analysis in monitoring tibial plateau fractures.* Acta Orthopaedica, 2010. **81**(4): p. 487-494.
57. Laende, E., et al., *Implementation and validation of an implant-based coordinate system for RSA migration calculation.* J Biomech, 2009. **42**: p. 2387-2393.
58. Brainerd, E., et al., *X-ray reconstruction of moving morphology (XROMM): precision, accuracy and applications in comparative biomechanics research.* J Exp Zool A Ecol Genet Physiol, 2010. **313**(5): p. 262-79.
59. Hardy, W.N., et al., *Investigation of head injury mechanisms using neutral density technology and high-speed biplanar x-ray.* Stapp Car Crash J, 2001. **45**: p. 337-368.

60. Lucas, E., *M.A.Sc Thesis: Measuring In Vivo Internal Spinal Cord Deformations During Experimental Spinal Cord Injury Using a Rat Model, Radiography, and Fiducial Markers*, in *Department of Mechanical Engineering*. 2010, University of British Columbia: Vancouver, BC.
61. Hardy, W.N., et al., *A study of the response of the human cadaver head to impact.* Stapp Car Crash J, 2007. **51**: p. 17-80.
62. Candes, E., et al., *Fast discrete curvelet transforms.* Multiscale Modeling & Simulation, 2006. **5**(3): p. 861-899.
63. Valstar, E., et al., *Guidelines for standardization of radiostereometry (RSA) of implants.* Acta Orthopaedica, 2005. **76**(4): p. 563-572.
64. Bottner, F., et al., *Radiostereometric analysis: the hip.* Hospital for Special Surgery, 2005. **1**(1): p. 94-99.
65. Lawrie, D.F., et al., *Insertion of tantalum beads in RSA of the hip.* Acta Orthopaedica, 2003. **74**(4): p. 404-407.
66. Hill, N., *Closest points function*, in *MATLAB*, closest_points.m, Editor. 2001, University of British Columbia.
67. Neumann G, M.A., Zou KH, Minas T, Coblyn J, Winalski CS, Lang P, *Prevalence of labral tears and cartilage loss in patients with mechanical symptoms of the hip: evaluation using MR arthrography.* Osteoarthritis and Cartilage, 2007. **15**(8): p. 909-917.
68. Rathnayaka, K., et al., *Effects of CT image segmentation methods on the accuracy of long bone 3D reconstructions.* Med Eng & Phys, 2011. **33**: p. 226-233.
69. Gelaude, F., J. Vander Sloten, and B. Lauwers, *Accuracy assessment of CT-based outer surface femur meshes.* Comp Aided Surg, 2008. **13**(4): p. 188-199.
70. Gray, H., *Anatomy of the Human Body*. 1918, Philadelphia, PA, USA: Lea & Febiger.
71. Bergmann G, D.G., Heller M, *Hip contact forces and gait patterns from routine activities.* J Biomech, 2001. **34**(7): p. 859-871.
72. Bay BK, H.A., Olson SA, Sharkey NA, *Statically equivalent load and support conditions produce different hip joint contact pressures and periacetabular strains.* J Biomech, 1997. **30**(2): p. 193-196.
73. Lattanzi, R., et al., *Specialised CT scan protocols for 3D pre-operative planning of total hip replacement.* Med Eng & Phys, 2004. **26**(3): p. 237-245.

Appendix A: Phantom acetabulum

The phantom acetabulum, or cup surface, was manufactured from a cube of Delrin® thermoplastic (50.8mm x 50.8mm x 38.1mm, McMaster-Carr, Princeton, NJ) with a hemisphere milled into the bottom surface (38.1mm-diameter ±0.025mm, UBC Machine Shop, Vancouver, BC).